

# **Systematic studies of the beam dynamics with a superconducting damping wiggler at KARA**

Zur Erlangung des akademischen Grades eines  
DOKTORS DER NATURWISSENSCHAFTEN (DR. RER. NAT.)  
von der KIT-Fakultät für Physik des  
Karlsruher Instituts für Technologie (KIT)

genehmigte  
**Dissertation**  
von

Dipl. Phys. Julian Gethmann

Tag der mündlichen Prüfung: 25.06.2021  
Referentin: Prof. Dr. A.-S. Müller  
Korreferent: Prof. Dr. G. Drexlin



This document is licensed under a Creative Commons Attribution 4.0 International License (CC BY 4.0): <https://creativecommons.org/licenses/by/4.0/deed.en>

# Contents

<b>1. Introduction</b>	<b>1</b>
<b>2. Theoretical Foundations</b>	<b>5</b>
2.1. Theory of particles moving in an accelerator . . . . .	5
2.1.1. Coordinates in a particle accelerator . . . . .	5
2.1.2. Beam dynamics . . . . .	5
2.1.3. Motion in an accelerator and Twiss parameter . . . . .	7
2.1.4. Tune and chromaticity . . . . .	8
2.1.5. Longitudinal dynamics . . . . .	11
2.1.6. Synchrotron radiation and insertion devices . . . . .	15
<b>3. Experimental setup and methods</b>	<b>23</b>
3.1. KARlsruhe Research Accelerator . . . . .	23
3.2. Wigglers in KARA . . . . .	25
3.3. Measurement methods . . . . .	27
3.3.1. Tune measurement . . . . .	27
3.3.2. Chromaticity measurement . . . . .	27
3.3.3. Orbit bump measurements . . . . .	29
3.3.4. Amplitude-dependent tune shift measurement . . . . .	31
3.3.5. Linear Optics from Closed Orbit . . . . .	32
<b>4. Including wiggler models into the storage ring KARA</b>	<b>35</b>
4.1. Choosing a field representation . . . . .	36
4.2. Comparison of three wiggler implementations available in the <i>elegant</i> tracking code . . . . .	40
4.2.1. Description of the implementations . . . . .	41
4.2.2. Methods to evaluate the simulation results of the different implementations . . . . .	42
4.2.3. Results of the simulations with the different implementations . . . . .	42
<b>5. Developing and refining models of the storage ring KARA</b>	<b>51</b>
5.1. Normal operation mode . . . . .	51
5.2. Short-bunch mode . . . . .	56
<b>6. Experimental characterisation of the wiggler in the storage ring</b>	<b>59</b>
6.1. Heat load measurements . . . . .	60

6.2. Tune measurements . . . . .	60
6.3. Search for sextupole and other not expected multipole components . . . . .	64
6.4. Measurement of octupole components . . . . .	66
6.4.1. Orbit bumps . . . . .	67
6.4.2. Amplitude Dependent Tune Shift (ADTS) . . . . .	71
6.4.3. Evaluation of the ADTS measurements . . . . .	72
6.4.4. Conclusion of the evaluation of octupole components utilising tune measurements . . . . .	80
<b>7. Effects in the short-bunch operation mode</b>	<b>81</b>
7.1. Beta-beating mitigation, radiation damping, and further transversal beam dynamics considerations . . . . .	81
7.2. Considerations of bucket deformation in short bunch mode . . . . .	83
<b>8. Summary and outlook</b>	<b>93</b>
<b>Appendix</b>	<b>97</b>
A. Parameter tables . . . . .	97
A.1. Measurements . . . . .	97
B. Derivations . . . . .	101
B.1. Rigidity . . . . .	101
B.2. Further comments on phase space and trace space . . . . .	101
B.3. Orbit bump correctors . . . . .	101
B.4. Dispersion variation . . . . .	102
B.5. Field integral measurements . . . . .	102
B.6. Further field components . . . . .	102
B.7. Field representations . . . . .	103
List of Symbols . . . . .	107
List of Acronyms . . . . .	108
<b>Bibliography</b>	<b>111</b>

# 1. Introduction

Particle accelerators exist in different variants serving different purposes in scientific, industrial and medical applications. In the field of high energy physics, hadron colliders are often seen as “exploration machines” and lepton colliders as facilities for precise measurements of the particles. The Large-Hadron-Collider (LHC) is such a hadron collider at which the Higgs boson was found, that couldn’t be characterized completely [et.20], yet. It is a storage ring collider where the colliding particles are accelerated in forward direction by the radio frequency cavities and perpendicularly, to form a closed ring, by bending magnets. This results in strong radiation, called *synchrotron radiation* named after the synchrotron circular accelerator in which it was discovered [et.20]. For colliders of light particles this is a big disadvantage and was one of the limiting factors of LHC’s predecessor, the Large Electron-Positron collider (LEP), because the radiation power losses scale with  $1/m^4$  [Hue, Wie07]. Hence, there are concepts for linear colliders as the next large high energy physics experiment machine, namely the International Linear Collider (ILC) and the Compact Linear Collider (CLIC) [Eur20, The18].

Nonetheless, the synchrotron radiation can also be used for scientific purposes. Nowadays, dedicated synchrotrons exist that utilise this broadband and intense light. The Karlsruhe Institute of Technology (KIT) has got a storage ring called KARlsruhe Research Accelerator (**KARA**) providing its radiation for a variety of use cases ranging from imaging with hard x-rays to lithography, and THz and infrared spectroscopy [ANK14].

Modern synchrotron light sources make use of insertion devices (ID) that provide much higher intensities than bending magnets do. One kind of such an ID is a so-called *wiggler*. Its spectrum is similar broadband as that of a bending magnet, but much stronger enabling hard x-ray imaging at **KARA**’s IMAGE beamline.

Though in general synchrotron radiation is not wanted at high energy physics accelerators, the next generation of colliders will make use of it, too. They produce it on purpose before accelerating the beam to its final energy to actively reduce the transverse momentum. Thereby the luminosity and thus the statistics of the collision processes can be increased. For this purpose very strong wigglers, then called *damping wiggler*, are used.

For the CLIC project it is planned to have two damping rings each with two straight sections with 26 2-m-long superconducting wiggler with a magnetic field of 3 T and a period length of 0.05 m [The18] each. The layout of the CLIC facility and one damping ring is

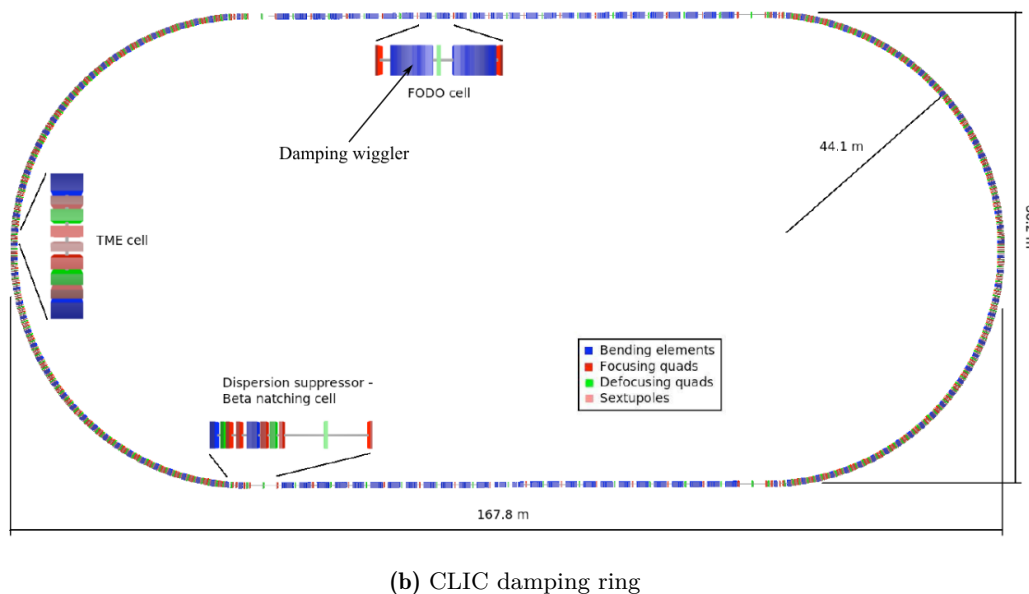
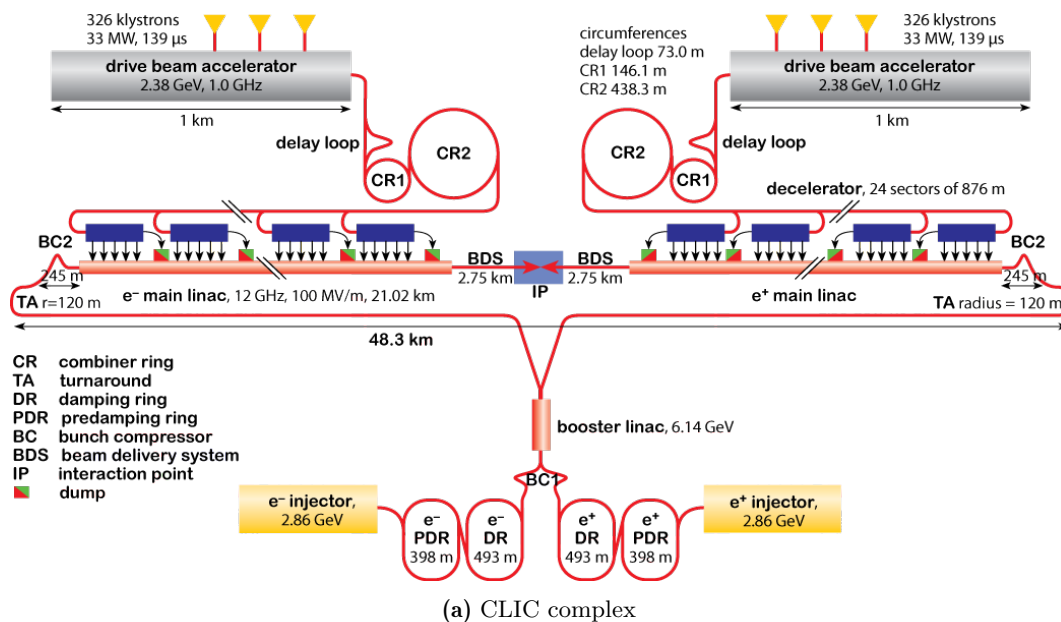


**Figure 1.1.: Sketch of the CLIC complex and damping rings.** The originally planned layout of the Compact Linear Collider (CLIC) (1.1a) and one damping ring (DR) (1.1b) in particular are depicted. The damping rings are located before the main linac, at the bottom of Fig. 1.1a.

Each of the two damping rings would have two times 26 of 2-m-long damping wigglers, depicted as blue blocks inside the FODO cells that form the straight sections—labeled as “Bending elements”—in Fig. 1.1b. One prototype of such a wiggler is installed at the storage ring KARA. Based on: clic-study.web.cern.ch/[The18], annotation by me.

sketched in Fig. 1.1.

After the injection and pre-acceleration the electron beams’ oscillations are damped in the pre damping rings (labelled PDR in the figure) and damping rings (DR) with the damping wigglers, before the beams are longitudinally compressed (in BC1, BC2), guided (in TA,

BDS), and accelerated (in booster linac, main linac) until they collide in the interaction point (IP).

A novel cooling technique for superconducting wigglers was developed by the Budker Institute of Nuclear Physics (BINP) to make individual wigglers more accessible to maintenance by using conduction cooling instead of bath cooling. This and the expected high heat load from the upstream wigglers are challenging for devices with these high fields and relatively short period length. Also, damping rings with superconducting wigglers have not been built yet, so the demand to test a prototype of such a wiggler emerged.

The Conseil Européen pour la Recherche Nucléaire (CERN), the KIT and the BINP have established a collaboration to investigate the maturity of the technology and to investigate beam dynamic effects caused by a prototype of such a wiggler build by BINP and installed in **KARA**. The wiggler serves as a prototype for **CERN** and as a light source for KIT's IMAGE beamline at **KARA**.

In this thesis, the question if damping wigglers can be used in such large scale, as planned for damping rings, will be tackled. Can the beam dynamics of the wigglers be simulated properly and can the effects be experimentally confirmed? Or does it turn out that beam dynamics of damping wigglers are not understood sufficiently well to rely the next generation collider physics accelerators thereon when ca. 50% of the damping rings' circumference are damping wigglers? Can one find effects appearing in real devices that are not covered by simulations so far? These are questions, this thesis tries to answer by simulating the damping wiggler prototype and doing measurements with it in **KARA**. For the **CLIC** project emerging from a conceptual design study to a technical design study it is of interest if this prototype can fulfill the expectations and work reliably in a real accelerator. This is the topic of this thesis. As collective effects showed to be of importance for the **CLIC** damping rings [The18] in the past, it is also of interest to do first experiments with this wiggler with regard to collective effects. At **KARA** there is also a strong research on one collective effect, the so-called “micro-bunching instability” which is under investigation in theory, simulation and experiments. Therefore it makes sense to experimentally investigate the wiggler's influence on this particular collective effect within this work.

After the necessary theoretical background on accelerator physics, beam dynamics, synchrotron radiation and insertion devices—in Chapter 2—, the experimental setup of the accelerator and its insertion devices and then the simulation and measurement techniques are presented in Chapter 3. Because often IDs are simulated as many alternating dipoles or quadrupoles only acting in the vertical plane no common approach exists that satisfies our needs for the simulation, in particular higher order multipoles represented in actual field data. So different approaches for including the wiggler into the storage ring models are evaluated and compared against each other. This encompasses, firstly, the transformation of magnetic field data to Fourier components as input for different wiggler implementation of the particle tracking code *elegant*. And, secondly, the selection of the actual implementation of the wiggler model. The available options and choices made will be discussed in Chapter

4. The basic functionality, features and influence of the wiggler on beam dynamics are tested experimentally in the 2.50 GeV operation mode. In this mode also heat load studies were conducted. Some further beam dynamics investigations and experiments were carried out in the short-bunch, low- $\alpha$  mode at 1.30 GeV beam-energy to better understand the mechanisms of coherent synchrotron radiation and the so-called micro-bunching instability. Accordingly, the development of two different models of the storage ring is presented in Chapter 5. Chapter 6 describes the experimental characterisation of the wiggler. This includes the findings of the heat load studies as well as the beam dynamics investigations that yielded additional octupole components of the integrated magnetic field. The wiggler was not only used to investigate its transverse beam dynamics, but it was also used to investigate the influence of the damping time on the THz radiation emitted by the electron beam. This happened in the special short-bunch, low- $\alpha$  mode. The optics manipulation needed to operate the wiggler in this special operation mode along with the experimental results of these efforts are presented in Chapter 7.

## 2. Theoretical Foundations

### 2.1. Theory of particles moving in an accelerator

This theory part is based on the textbook of [Wie07], and the accelerator physics lectures by Anke-Susanne Müller and Axel Bernhard if not stated differently.

#### 2.1.1. Coordinates in a particle accelerator

In this work a right-handed coordinate system will be used with the longitudinal direction  $z$ , the horizontal direction  $x$ , and the vertical direction  $y$ , if not stated otherwise. If it is relevant to distinguish between the coordinates moving with the reference electron and the global, fixed coordinates of the ring, then the coordinate  $s$  is used for the coordinate system moving along with the reference particle instead of  $z$  which then refers to a global, fixed coordinate system.

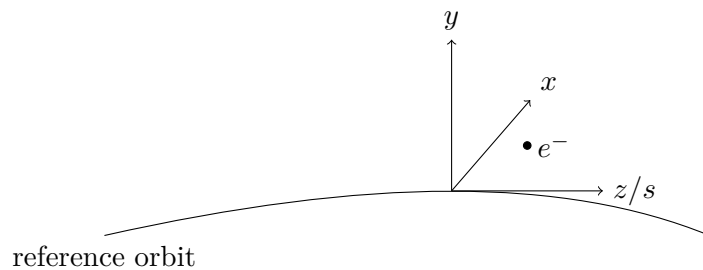


**Figure 2.1.: Coordinate system.** The coordinate system used in this work. The electron  $e^-$  is positioned relative to a right handed coordinate system that follows the reference orbit around the ring. If the movement of the coordinate system is relevant  $s$  is used for the longitudinal axis, otherwise  $z$  is used.

#### 2.1.2. Beam dynamics

Most of the work was done for electron storage rings, namely **KARA** and the **CLIC** damping rings, so that we will concentrate on beam dynamics of highly relativistic electrons in circular accelerators. In such accelerators the Lorentz force  $\vec{F} = q(\vec{E} + \vec{v} \times \vec{B})$  that acts on electrons is split into its electric and magnetic parts and aligned so that these components are orthogonal to each other. The electric field  $\vec{E}$  acts in radio frequency cavities onto the

electrons in the longitudinal direction and hence is responsible for their acceleration. The magnetic field  $\vec{B}$  acts in the transverse directions and guides the electrons along the ring. This separation of the acting forces reflects in the separated description of the motions in the transverse—horizontal and vertical—plane and the longitudinal plane in many aspects. Such a ring does include other magnets besides dipole magnets, accelerating structures and further elements. Nevertheless, since we are looking at a ring, the magnetic structure is seen by the particles periodically each turn, so that one can speak of a magnetic lattice to describe this arrangement of the magnets.

Beside the Lorentz force also the centripetal force acts against the electrons, so that we get

$$\frac{1}{\rho(x, y, s)} = \left| \frac{e}{p} B_y(x, y, s) \right| = \left| \frac{ec}{\beta E} B_y(x, y, s) \right|$$

for the horizontal plane. A similar expression is true for the vertical plane ( $1/\rho_y \propto B_x$ ), but for practical reasons accelerators are built in the horizontal plane most often, so we ignore the vertical plane here. We can expand it with a Taylor series around  $x = 0$ , to get

$$\begin{aligned} \frac{e}{p} B_y(x) &= \frac{e}{p} B_{y0} + \frac{e}{p} \frac{dB_y}{dx} x + \frac{1}{2!} \frac{e}{p} \frac{d^2 B_y}{dx^2} x^2 + \frac{1}{3!} \frac{e}{p} \frac{d^3 B_y}{dx^3} x^3 + \dots \quad (2.1) \\ &= \frac{1}{\rho} + kx + \frac{1}{2!} mx^2 + \frac{1}{3!} ox^3 + \dots \\ &\Rightarrow \text{Dipole} + \text{Quadrupole} + \text{Sextupole} + \text{Oktupole} + \dots \end{aligned}$$

In a so-called split function lattice the individual terms of that series can be identified with magnets of their particular kind. The momentum normalised coefficients are called “quadrupole strength”, “sextupole strength” and so on. These different mathematical multipoles are realised as individual physical magnets, as shown in Fig. 2.2 on the next page and serve different purposes. Dipoles bend the beam. Here it also makes sense to define the bending angle  $\theta$  as the integral over a finite length:  $\theta = \int_{s_1}^{s_2} \frac{1}{\rho}$ . Quadrupoles focus the beam in one plane towards the central axis of the magnet as shown in Fig. 2.2b on the facing page and defocus it in the other plane. In Fig. 2.2b on the next page we see a horizontally focusing magnet that defocuses in the vertical plane. This focusing counteracts the inherent divergence of the electron beam that consists of  $10^9$  to  $10^{11}$  electrons that are bunched longitudinally and repel each other with Coulomb’s force. Sextupoles are used for correction of chromatic effects, see Section 2.1.4 on page 8, and higher-order multipoles for corrections of errors introduced by lower-order multipoles. For given energy the bending magnets need to have a specific magnetic field, so that particles in the ring are bent into a “closed orbit”. Besides the reference orbit there are other closed orbits for particles for which the energy deviates from the reference energy, the so-called dispersion orbit. The description of the motion of the particles, namely the oscillation around such orbits, is called beam dynamics.

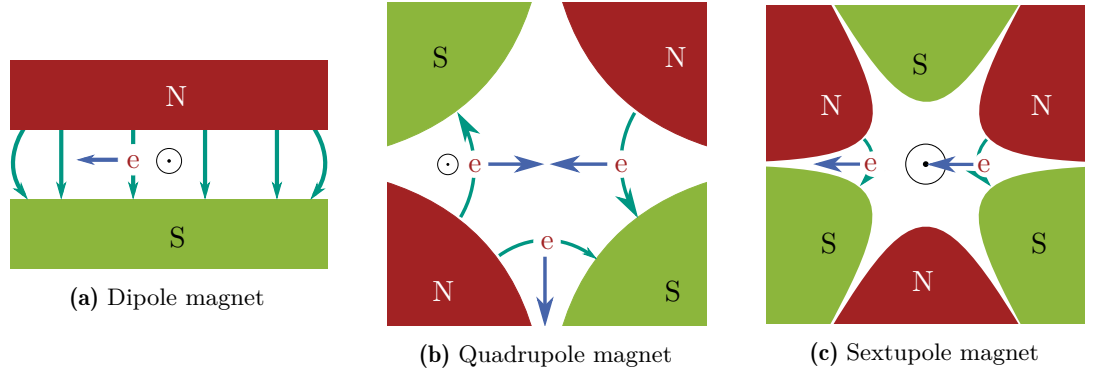


**Figure 2.2.: Different magnets used in an accelerator.** The magnetic field lines between the north pole (red) and south pole (green) are shown in green, the electron is coming from the paper plane as indicated by the circle with a dot at its centre. The Lorentz force caused is indicated by blue arrows. Dipole magnets (a) are used to bend the beam. Quadrupole magnet (b) are used for focusing and sextupole magnet (c) for chromatic corrections.

### 2.1.3. Motion in an accelerator and Twiss parameter

The trajectory of a particle oscillating around the reference orbit of a linear lattice, i. e. a lattice composed of dipoles and quadrupoles, can be described by the following equation of motion [Wie07] which is often called **Hill's equation**

$$u'' + k(z)u = 0 \quad (2.2)$$

with the transversal coordinates  $u$  ( $x$  or  $y$ ), and a longitudinal dependent function  $k$ . Here we do not account for any de- or acceleration or momentum deviations from the reference particle, and the right-hand side is 0 for the moment. This **Hill's equation** is the equation of a  $z$ -dependent harmonic oscillator which can be solved by

$$u(z) = \sqrt{\varepsilon_u} \sqrt{\beta_u(z)} \cos(\psi(z) - \psi_0) . \quad (2.3)$$

The emittance  $\varepsilon_u$ , more precisely named **Courant-Snyder invariant** in this case of single-particle dynamics, and the phase  $\psi$  are constants of the integration whereas  $\beta_x$  and  $\beta_y$  depend on the position in the ring and are called *beta functions*. Because these oscillations around the reference orbit described by Eq. (2.3) were discovered at the betatron they are often referred to as betatron oscillation. By solving the differential equation Eq. (2.2) with Eq. (2.3) the **Courant-Snyder invariant** [Wie07] is derived as

$$\gamma_u u^2 + 2\alpha_u u u' + \beta_u u'^2 = \varepsilon_u . \quad (2.4)$$

The functions  $\alpha_u = -\frac{1}{2}\beta_u'$ ,  $\gamma_u = (1 + \alpha_u^2)/\beta_u$ , and  $\beta_u$  are called **Twiss parameters** or sometimes **Optical functions**. Together with the **Courant-Snyder invariant** they describe the complete state of a particle in an accelerator that is considered as a conservative system. If we consider many particles instead of one, we speak of the emittance instead of

the **Courant-Snyder invariant** and the functions describe the state of the whole particle distribution. Equation (2.4) represents an ellipse in the phase space  $u, u'$  with the area  $\pi\epsilon_x$  as depicted in Fig. 2.3. As it is the common practice according to [Flo03], here

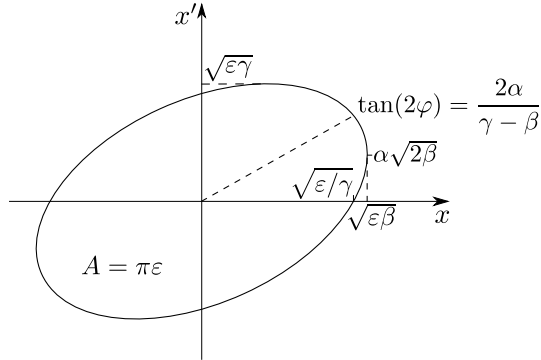


**Figure 2.3.: Horizontal phase space ellipse.** The phase space ellipse, here for the horizontal case, describes the location (axis of abscissae) and momentum (axis of ordinates) of a particle. Its area is a constant  $A = \pi\epsilon_x$  for conservative forces.  $\alpha, \beta, \gamma$  are the so-called Twiss parameter,  $\epsilon$  is a constant factor around the ring and  $\phi$  is the phase of the particle along the ring. This phase space ellipse exists also for the vertical plane and slightly different for the longitudinal plane, too. Based on [Wie07].

and in the following the trace space is referred to as phase space. The trace space is  $(x, x') = (x, \frac{p_u}{p_z})$  whereas the real phase space would be  $(x, p_u)$ . Here  $p_u$  are the normalized canonical momenta and  $u'$  the slopes. The velocities thus are denoted as  $\dot{u}$ .

In the case of field-free regions with only a longitudinal vector potential ( $\vec{A} = (0, 0, A_z)$ ) optics codes can set  $p_u = u'$  in the Hamiltonians describing the system, see e. g. [Wie07], and the trace space then indeed is the phase space. Also only the projections in one plane are used throughout this work. So instead of the full six-dimensional trace space three (horizontal, vertical, and longitudinal) two-dimensional projections are considered.

#### 2.1.4. Tune and chromaticity

As focusing of the quadrupole magnets causes an additional phase advance  $\psi$  of the particle described by Eq. (2.3), the **tune** is the phase advance integrated over the complete ring divided by  $2\pi$  [Wie88, Hin08]:

$$\nu_u = \frac{1}{2\pi} \oint \frac{d\bar{s}}{\beta(\bar{s})} = \frac{\psi(C)}{2\pi}$$

In this work  $\nu_u$  is used for the full tune with its integer part as well as for the **fractional tune** which is dealt with and referred to as tune more often, because upon beam optics variation the tune typically is changed only by less than 0.5. A common other notation for the tune in literature is  $Q$  and sometimes  $q$  for the fractional tune. The tune can be changed mainly by changing the focusing in the quadrupoles which increase or decrease the focusing in one plane and do the opposite on the other plane. We recall the focusing

strength

$$k = \frac{e}{p}g = \frac{ec}{\beta E}g, \quad (2.5)$$

with the field gradient  $g = \frac{\partial B_y}{\partial x}$ , the momentum  $p$ , the electron charge  $e$ , velocity  $\beta = \frac{v}{c}$  normalized to the speed of light  $c$ , and the energy  $E$ . By convention one speaks of focusing magnets when  $k$  is positive in the horizontal plane, such that the horizontal tune increases. This implies a negative  $k$  in the vertical plane. In contrast, defocusing magnets are those with a negative  $k$ , defocusing in the horizontal plane.

As the tune is the measure of the oscillations per turn, it is the dominant oscillation frequency of the beam. Therefore it can be measured by frequency analysis of the oscillation spectrum. Typically the beam is slightly excited and the oscillations of the beam are measured using **Beam Position Monitors (BPMs)**. Then the **fractional tune** is taken from the **FFT** of the spectrum normalised by the spectrogram's size. The equation  $\nu_u = 1 \pm \frac{hf}{\omega_{\text{RF}}} \pmod{1}$  holds true, with the harmonic number  $h$  and the circular radio frequency  $\omega_{\text{RF}}$  and the measured tune frequency  $f$ . To measure the integer part of the tune and to determine the sign in the aforementioned equation, the orbit oscillations seen by all **BPMs** in a snapshot measurement (see e. g. [Bra09]) are counted. Of course at least twice the number of **BPMs** as the integer part of the tune are needed because of the sampling theorem [But09].

The tune should not be an integer value, so that particles do not see the same betatron oscillation after  $n$  turns which would drive resonances. As there is coupling between the planes, this condition has to be considered in all three planes, as well as their coupling terms. This yields the condition:  $n\nu_x + m\nu_y + l\nu_z = p, \forall n, m, l, p \in \mathbb{N}_0$ , which has to be fulfilled. Here  $p$  is the order of the resonance. Though in principle this leads to very many resonance conditions in practice only resonances for  $p < 4$  are relevant for electron storage rings, because for electron storage rings resonances of higher-order are damped as described in Section 2.1.6 on page 17. At proton accelerators much higher resonance orders have to be avoided, too, because of the by far smaller damping of the betatron oscillations. In Fig. 2.4 on the next page the lines of the resonances in the space spanned by vertical and horizontal fractional tune are depicted up to the fourth-order.

When getting close to resonance lines with both transversal tunes, particles with a slightly different tune are already resonating, e. g. because of chromaticity, see the following paragraph. So the beam as a whole gets more and more unstable the closer one gets to the resonance line. A so-called **stopband** can be found in which particles do not survive for longer than a few turns. In fact, when trying to cross vertical and horizontal tunes they do not cross. Instead the tunes of the particles that would hit a resonance, change their tune in one plane to the tune of the respective other plane. Due to this mechanism the tunes do not hit the resonance, but create a gap between the lines of the moving tunes—the **stopband**. The width of this **stopband** varies with different parameters, like higher-order multipole components in the magnetic lattice which will play an important role in this

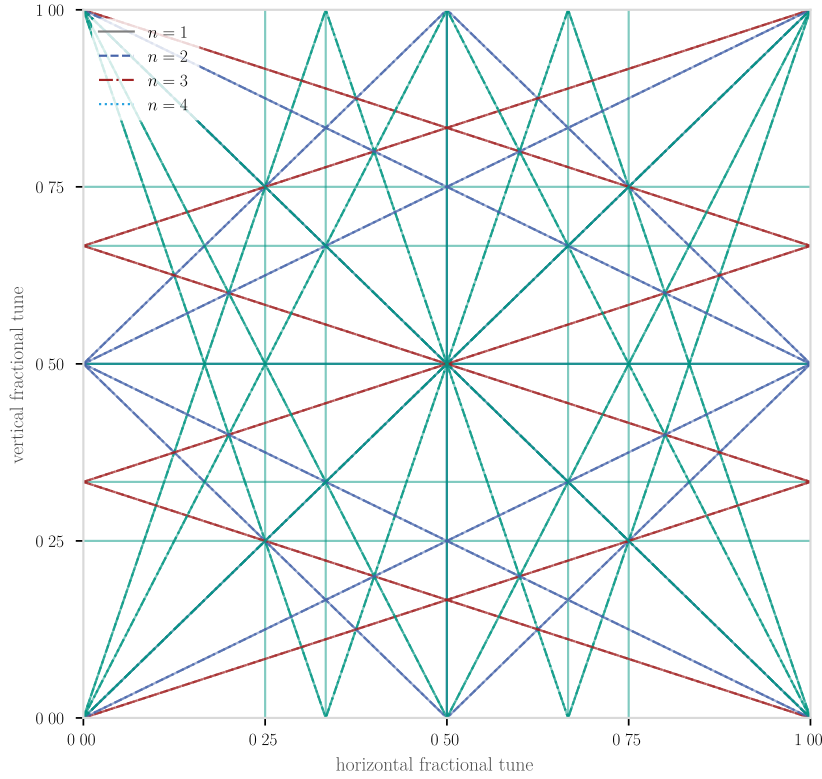


**Figure 2.4.: Tune diagram.** Fractional tune resonance lines up to the fourth order. Electron beams oscillating with frequencies corresponding to the tune resonance lines eventually get lost. Higher order oscillations are damped fast enough, so that electron storage rings like **KARA** do not have to take care of them.

work.

The **chromaticity** represents the differences in the magnetic lattice focusing for particles with different energies and occurs when particles with different energies pass a focusing magnet, just like chromatic aberration occurs for different wavelength passing through an optical lens. As such it occurs when off-momentum particles get focused, e.g. in a quadrupole magnet. Then these particles with different energies experience different focssing. Therefore the chromaticity is defined as the derivative of the tune with respect to the momentum and sometimes noted as  $\nu'$  where the “'” is the derivative with respect to momentum. Usually, in accelerator physics “'” is the derivative with respect to the longitudinal position  $s$ . This parameter is also a typical parameter characterising the beam dynamics. The first-order chromaticity is relatively easy to measure and gives insight to the sextupole components inside the ring. These are the highest order multipole components at **KARA** that can be directly influenced by magnets.

The *natural chromaticity* is the uncorrected chromaticity of a ring. In focusing rings it is negative by definition [Bra09, Hin08]:

$$\xi_{\text{nat}} = \nu' = -\frac{1}{4\pi} \oint k(s)\beta(s)ds. \quad (2.6)$$

Here  $k$  is the quadrupole strength and  $\beta \geq 0$ .

As one can see, the natural chromaticity is induced by focusing elements ( $k$ ). It can be counteracted by sextupoles in dispersive sections. Indeed it needs to be compensated to be slightly above 0 to mitigate so-called “head-tail-instabilities” [Bra09].

### 2.1.5. Longitudinal dynamics

So far we primarily looked at the two transversal planes of the 6d phase space of beam dynamics. However, we need to have a look at the longitudinal dynamics, too. There we often take the energy  $E$  or the relative momentum deviation  $\delta = \frac{\Delta p}{p_0} = \frac{p-p_0}{p_0}$  instead of the longitudinal momentum as the conjugate generalized momenta of the phase space and the time  $t$  or phase  $\psi$  of the particle as the generalized coordinates instead of the location.

As in the transversal planes, particles oscillate in the longitudinal plane, too. These oscillations are called **synchrotron oscillations**. The corresponding tune is the synchrotron tune.

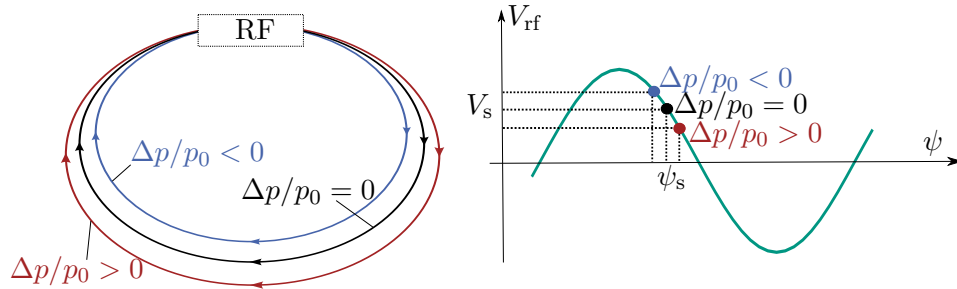


**Figure 2.5.: Phase focusing.** On the left side a idealised ring with one RF cavity is sketched and on the right side the voltage of the cavity depending on the phase of the electron. Particles with less momentum (blue,  $\Delta p/p_0 < 0$ ) than the reference particle (black,  $\Delta p/p_0 = 0$ ) arrive earlier in rings that are operated above transition energy  $\gamma_{tr}$ , i. e. with a smaller phase than the reference particle—oscillating in the synchronous phase— $\psi < \psi_s$  and thus see a higher accelerating voltage. The contrary holds for particles with too large momentum (red,  $\Delta p/p_0 > 0$ ). Particles oscillate around the synchronous phase  $\psi_s$ .

Fig. 2.5 shows the process of phase focusing causing the synchrotron oscillations. On the right side the oscillating voltage of the standing wave in the radio frequency (rf) cavity is plotted against the phase of the arrival of the particle in the cavity. The synchronous phase  $\psi_s$  is the phase of the reference particle where the particle gains as much energy as it lost since the last pass through a cavity. The corresponding voltage  $V_s$  can be called synchronous voltage.

Particles with less (more) momentum ( $\Delta p/p_0 \leq 0$ ) are bent stronger (weaker) in the dipoles and follow a shorter (longer) orbit, as depicted on the left side in blue (red). This means they arrive earlier (later) in the cavity, so at a smaller (larger) phase—right side of the graphic. Therefore they see a higher (lower) voltage and are accelerated more (less) than the reference particle at the synchronous phase. This leads to a relative energy gain (loss) and momentum increase (decrease) and eventually these particles become the particles with too much (little) momentum. An oscillation around the synchronous phase  $\psi_s$  arises

that is called **synchrotron oscillation**. This oscillation is not just in the energy axis of the phase space, but also translates into the time or location axis, so that particles at the head of the bunch eventually end up at the tail of the bunch and vice versa. There is a second flank where the acceleration condition  $V_{\text{rf}} > 0$  is fulfilled,  $\pi/2$  before the case described. However, this phase focussing mechanism does not work there, because particles with less energy would lose energy in relation to the reference particle in the long run, they finally cross  $V_{\text{rf}} = 0$  and are decelerated. If the energy is too low particles eventually get lost by hitting the beam pipe. This implies firstly that particles can only survive in a region around the synchronous phase and secondly that the beam is bunched by the described effect of phase focusing.

With the chromaticity we already saw one effect of energy deviations within the particle distribution. Another effect is the **dispersion**  $\eta$ . Particles with different momenta are bent differently and thus go on different orbits described in linear approximation by the dispersion function  $\eta(s)$  with  $u_\delta = \delta\eta(s)$ . This effect is called dispersion also in analogy to optics. In the first approximation only dipoles change the dispersion orbits [Wie07]. The dispersion function is derived from the inhomogeneous differential equation for the particle's radial plane taking the momentum deviation into account [Hin08]:

$$\eta(s) = \frac{\sqrt{\beta(s)}}{2 \sin \pi \nu_u} \int_s^{s+C} h(\bar{s}) \sqrt{\beta(\bar{s})} \cos(\psi(\bar{s}) - \psi(s) - \pi \nu_u) d\bar{s}, \quad (2.7)$$

with the reference orbit  $h(s) = \frac{1}{\rho_0(s)}$  and the closed orbit circumference  $C$ .

One consequence of the dispersion is the momentum dependence of the closed orbit circumference. The **momentum compaction factor**  $\alpha_c$  describes this momentum dependent path lengthening and links the dispersive orbit  $\Delta C/C_0$  with the relative momentum deviation  $\delta = \frac{p-p_0}{p_0}$ . It holds true that  $\alpha_c = \left\langle \frac{\eta}{\rho} \right\rangle = \frac{\Delta C/C_0}{\delta}$ , with the closed orbit circumference  $C$  of the considered particle and the length of the reference trajectory  $C_0$  and the relative momentum deviation of the particle  $\delta$ . There are also higher-order momentum compaction factors that are noted with numerical indices starting with 1 in this work.

The simulation code *elegant*, more on it in Chapter 4 on page 35, calculates the momentum compaction factor up to the next to leading order, so that the path length is  $s = s_0 + \alpha_0 C \delta + \alpha_1 C \delta^2$ . In contrast to this definition, at **KARA** the matching of the momentum compaction factor to the current optics was done for one effective momentum compaction factor that does not take energy deviations into account.

Moreover, in this thesis the *momentum compaction*  $\eta_c$  is defined as it is done in e. g. [Wie07, Hin08] as  $\eta_c = \left( \frac{1}{\gamma^2} - \alpha_c \right)$ . The transition energy  $\gamma_{\text{tr}} = \frac{1}{\sqrt{\alpha_c}}$  is the energy at which the particle's energy gained from the acceleration **RF** does not result in a significant velocity change, but mainly results in an orbit change. At that energy the momentum compaction vanishes and stable operation is not possible. In general, electron synchrotrons operate above transition. In this case, the momentum compaction is negative. In the longitudinal

phase space particles with positive  $\eta_c$  move anti-clockwise and with negative  $\eta_c$  move clockwise, see [Wie07].

### Separatrix

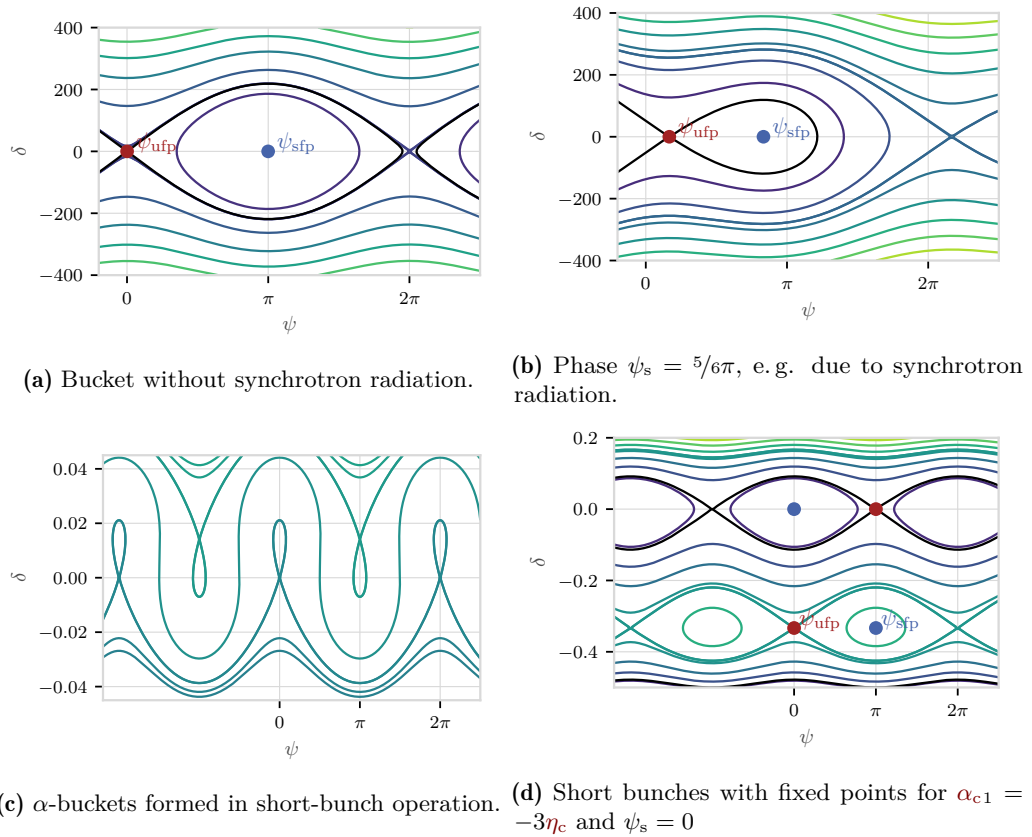


**Figure 2.6.: Separatrix for different phases.** The separatrix, black line, is the line that separates the area of stable particle motions (the inside, also-called bucket) from the unstable parts. The points  $\psi_{\text{sfp}}$  and  $\psi_{\text{ufp}}$  are the stable (blue) and unstable (red) fix points of this bucket. The colour code of the equipotential lines represents the energy ranging from dark, representing low energy, to yellow, representing high energy. Fig. 2.6a shows a closed bucket for the conservative case, where there is no synchrotron radiation. In Fig. 2.6b the particle is accelerated and there exists energy loss, e.g. by synchrotron radiation, because the energy is above transition energy ( $\gamma > \gamma_{\text{tr}}$  and the particle arrives with a phase between  $\frac{\pi}{2} \leq \varphi < \pi$ ). In 2.6c so-called “ $\alpha$ -buckets” are shown. They look like tilted  $\alpha$ s. Their length is very small. In 2.6d another case of these  $\alpha$ -buckets is shown, where the two times two stable and unstable fixed points are depicted. For a more detailed explanation of this plot see the text. The parameter for the plots were chosen to show the different features.

In the longitudinal phase space the separatrix separates the particles with stable motions that are inside the so-called bucket—the largest closed trajectory in the phase space diagram—from those that are unstable. The latter ones get either too much or too little energy when passing the cavities and eventually hit the wall. This process can be described

by the following Hamiltonian which is derived in [Wie07] as

$$\mathcal{H}(\psi, \delta) = \frac{1}{2}(-\delta h \omega_{\text{rev}} \eta_c)^2 - \frac{\Omega^2}{\cos \psi_s} [\cos \psi - \cos \psi_s + \psi \sin \psi_s - \psi_s \sin \psi_s] . \quad (2.8)$$

In this we have got the synchronous phase  $\psi_s$ , the actual phase of the particle  $\psi$ , and via the momentum deviation  $\delta = -\frac{\dot{\varphi}}{h \omega_{\text{rev}} \eta_c}$  the canonical phase variable  $\varphi = \psi - \psi_s$ , its time derivative  $\dot{\varphi}$ , and the synchrotron frequency

$$\Omega^2 = \omega_{\text{rev}}^2 \frac{h \eta_c e \hat{V}_0 \cos \psi_s}{2\pi \beta c p_0} . \quad (2.9)$$

This frequency depends on the revolution frequency  $\omega_{\text{rev}} = 2\pi f_{\text{rev}} = 2\pi \frac{C}{c\beta} = \omega_{\text{RF}}/h$ , the peak accelerating voltage of the cavity  $\hat{V}_0$ , speed of light  $c$ , the momentum of the reference particle  $p_0$ , its velocity  $\beta c$ , the harmonic number  $h$ —the maximum number of available buckets in a storage ring and factor between the revolution frequency  $\omega_{\text{rev}}$  and the circular radio frequency  $\omega_{\text{RF}}$ —, the momentum compaction  $\eta_c$ , and the elementary charge  $e$ .

An alternative formulation, depending on the energy deviation  $\delta$  and the phase  $\psi$ , can be found in [Rie14]

$$\mathcal{H}(\phi, \delta) = -\beta^2 E_0 \delta^2 \left( \frac{\alpha_0}{2} + \frac{\alpha_1}{3} \delta + \frac{\alpha_2}{4} \delta^2 \right) - \frac{eU_0 \cos \phi}{2\pi h} \quad (2.10)$$

for  $\alpha_c(\delta) = \alpha_0 + \alpha_1 \delta + \alpha_2 \delta^2$ . Here  $eU_0$  is the total energy loss per turn. It is especially handy when dealing with low momentum compaction factors  $\alpha_c$ , due to its explicit dependence on them.

Fig. 2.6 on the preceding page shows contours of this momentum deviation  $\delta$  against phase  $\psi$ . Figs. 2.6a and 2.6c on the previous page show situations for a synchrotron without synchrotron radiation and for one with short bunches in a so-called “low- $\alpha$ ”-operation. Fig. 2.6b and 2.6d show some features of these longitudinal phase spaces more distinctively. In Fig. 2.6b the synchronous phase is shifted by  $\pi/6$  which corresponds to a strong energy loss of the particles. This causes a typical “fish-like” shape of the bucket. In a conservative system, with no synchrotron radiation or particle losses, one could see an “eye-like” shape of the bucket like for a harmonic oscillator. Due to the radiated energy the phase is shifted and a gap of instability occurs around phases of  $2\pi$ . Also the phase of the stable fix point (blue point labelled  $\psi_{\text{sfp}}$ ) shifts away from  $(\psi = \pi, \delta = 0)$  to smaller phases whereas the unstable fix point (red point labelled  $\psi_{\text{ufp}}$ ) shifts from  $(\psi = 0, \delta = 0)$  to larger phases resulting in smaller regions of stability.

In Fig. 2.6d on the preceding page on the other hand one can see secondary buckets appearing that are shifted by  $\pi$  in phase and are also shifted in momentum. The centre of these buckets is no longer at  $\delta = 0$ , like for the original ones. This means one also gets two more fix-points, the local minima of the Hamiltonian. They are also plotted in Fig. 2.6d as blue points, but without labels. This effect which appears at very small  $\alpha_c$ s results in very

short bunches. These very short bunches show interesting behaviour like bursts of coherent synchrotron radiation that are current research topics.

### 2.1.6. Synchrotron radiation and insertion devices

When highly relativistic particles, say electrons, are accelerated they emit synchrotron radiation. Such an acceleration occurs when they are deflected transversely. In our reference system, we see the radiation in forward direction, because of the highly relativistic movement.

#### Coherent Synchrotron Radiation and Bursting

If the bunch length is in the order of the wavelength of the radiated light, this radiation will be temporal coherent. Let  $\mathcal{E}_j = e^{i(\omega t + \phi_j)}$  be the phase of the radiation field of one electron  $j$  radiating a photon of circular frequency  $\omega$ . Here  $\phi_j$  is the phase with respect to the centre of the bunch. Then the total radiated power is [Wie15]

$$P(\omega) \propto \sum_{j,l}^N \mathcal{E}_j \mathcal{E}_l^* = \underbrace{N}_{\text{incoherent}} + \underbrace{\sum_{j \neq l} e^{i(\phi_j - \phi_l)}}_{\text{coherent}}.$$

For the case of a storage ring with a Gaussian bunch profile and going from summation over all phases to integration, one gets

$$P(\omega) \propto p(\omega)N \left[ 1 + (N-1)\mathcal{F}^2(l, \lambda) \right] \quad (2.11)$$

with the radiation power of one electron  $p(\omega)$  and a form factor  $\mathcal{F}^2(l, \lambda) = \exp\left(-2\pi\frac{l^2}{\lambda^2}\right)$  that depends on the radiated wavelength  $\lambda$  and an effective bunch length  $l = \sqrt{2\pi}\sigma_z$ . For short bunches and long radiation wavelength  $\mathcal{F}^2$  approaches 1 (and not  $\mathcal{F}^2 \sim 0$ ). For bunch populations of  $10^8$  to  $10^{11}$  electrons this effect is very interesting, because the radiated power scales with the number of electrons squared instead of linearly as the incoherent part.

However, for vacuum wavelengths  $\lambda$  that are longer than the vacuum pipe aperture  $h$  the radiation is exponentially suppressed. Following [VW02] the suppression holds for wavelengths  $\lambda \geq \lambda_0 = 2h\sqrt{\frac{h}{\rho}}$  that define the so-called ‘‘shielding cut-off’’ wavelength  $\lambda_0$  with the bending radius  $\rho$ . In normal synchrotrons this effect of coherent synchrotron radiation is not significant. Nevertheless in synchrotrons with e.g. high currents and with short bunches it is.

In case of high enough bunch current  $I_b$ , collective effects cause substructures inside the bunch to appear, which means a distortion of the longitudinal phase space. Current theories describe this phenomenon by the following mechanism: short bunches see a stronger wake potential by the image charge in the beam pipe which cause substructures to appear. These



coil based wigglers change the magnetic field strength by varying the electric current in the coils.

Besides the radiation for experiments, another interesting aspect of wigglers for a different use case is their capability of damping betatron oscillations. There are special “damping wigglers” with a very high magnetic field that exploit this property. The electron radiates while moving along a curve, and hence loses momentum in the respective direction at that very moment, resulting also in transverse momentum loss. However, it is accelerated only longitudinally, so that it gets a net loss in transverse momentum and the transverse oscillation is damped. This *damping* is partially acted against by the so-called *quantum excitation*. Since the radiation is a stochastic process the electrons lose their momentum in steps and hence also change their dispersion orbit in discrete steps. This causes new betatron oscillations, so the beam is excited—hence quantum excitation. This quantum excitation and the damping result in an equilibrium of the betatron oscillations. A damping wiggler has got a very high field to cause much radiation accompanied with a large momentum change and thus a strong damping as long as a low dispersion causes little excitation.

### Damping

The wiggler causes strong radiation which implies that it causes also a big power loss for the electron beam [Hof04]:

$$P_{wI} = \frac{N_u \lambda_w I 2 r_0 c^2 e \langle B^2 \rangle E^2}{3(m_0 c^2)^3}$$

with  $N_u$  periods of length  $\lambda_w$ , the beam current  $I$ , the mean wiggler’s magnetic field strength  $\langle B \rangle$ , the beam energy  $E$ , and the classical electron radius  $r_0 = \frac{e^2}{4\pi\epsilon_0 m_0 c^2}$ , with vacuum permittivity  $\epsilon_0$ .

In this context *damping time* refers to the exponent of the exponentially damped betatron oscillation of the electrons. There are three damping times for the three planes. Typically the longitudinal one is bigger in the order of a magnitude, and the oscillation itself is slower. The damping times are defined as  $\tau_u = \frac{2E}{j_u U_0} T_0$  with the damping partition numbers  $j_u$ , beam energy  $E$  and the revolution period  $T_0$  and the energy loss per turn  $U_0$ . The damping partition numbers

$$\begin{aligned} j_x &= 1 - \mathcal{I}_4/\mathcal{I}_2, \\ j_y &= 1, \text{ and} \\ j_z &= 2 + \mathcal{I}_4/\mathcal{I}_2 \end{aligned} \tag{2.12}$$

connect the radiation integrals, see paragraph “**Radiation integrals**”, and the damping times of the three different planes. Following Robinson’s damping criterion they must add up to  $j_x + j_y + j_z = 4$  [Wie07].

## Radiation integrals

By convention, some integrals often appearing in calculations of properties and effects of synchrotron radiation in a storage ring are abbreviated as synchrotron radiation integrals. Since they are used for many simplifications the most relevant ones for this work are defined as follows [CMTZ13]:

$$\mathcal{I}_1 = \oint_C \left( \frac{\eta_x}{\rho_x} + \frac{\eta_y}{\rho_y} \right) ds, \quad (2.13)$$

$$\mathcal{I}_2 = \oint_C \left( \frac{1}{\rho_x^2} + \frac{1}{\rho_y^2} \right) ds, \quad (2.14)$$

$$\mathcal{I}_{4u} = \oint_C \frac{\eta_u}{\rho_u^3} \left( 1 \pm 2\rho_u^2 k \right) ds, \quad (2.15)$$

with the focusing strength  $k$  and the usual dispersion  $\eta$ , bending radius  $\rho$  integrated along the circumference  $C$ . In the fourth radiation integral  $\mathcal{I}_4$  the sign “+” is for the horizontal case ( $u \hat{=} x$ ) and “−” for the vertical case ( $u \hat{=} y$ ).

The first integral influences mostly  $\alpha_c$ . This is caused by the coupling to the dispersion  $\eta$ . The second one changes the emittance, radiation power and energy spread and by this the damping time and damping partition numbers, see paragraph “Damping”. That is caused by the quadratic dependence on the inverse bending radius and thus the radiation.  $\mathcal{I}_3$  is not relevant for this work and therefore not listed here. The fourth integral, with a cubic dependence on the inverse bending radius, is related to the damping partition numbers and emittance.

### 2.1.6.1. Influence of IDs on the beam dynamics

To be transparent to the orbit the start and end of the ID have to produce a smooth transition for the particles so that the particles neither have an offset nor an additional angle after passing the ID (see e. g. [Cla04, FEW<sup>+</sup>03]). To achieve this, the two so-called “field integrals” have to be zero:

$$II_y = \int_{-\infty}^{\infty} \int_{-\infty}^s B_y(s') ds' ds = 0 \quad (2.16)$$

$$x = \frac{e}{\gamma m_0 c} II_y. \quad (2.17)$$

$x$  is the offset which is caused by a non-vanishing *second field integral*  $II_y$ .

To also be “transparent” concerning the angle with which a particle exits the wiggler a similar relation holds true for the *first field integral* and the angle  $\alpha$ :

$$I_y = \int_{-\infty}^{\infty} B_y(s) ds = 0 \quad (2.18)$$

$$\alpha = \frac{e}{\gamma m_0 c} I_y. \quad (2.19)$$

To eliminate these integrals, the beginning and end of a wiggler need to have a special magnet configuration with decreasing strength towards the ends. Typical configurations are  $1/3, -2/3, 1, -1$  or  $1/4, -3/4, 1, -1$  (see e. g. [FEW<sup>+</sup>03]), with 1 as the full magnetic field, fractions of their strength and opposite signs for opposite field direction. The period length is the same as for the main magnets.

A planar wiggler has got the following magnetic field in linear approximation [Sch85]:

$$\vec{B} = \frac{m_0 c^2}{e} B_0 [\hat{y} \cosh(k_z y) \cos(k_z z) - \hat{z} \sinh(k_z y) \sin(k_z z)] , \quad (2.20)$$

with the on-axis field  $B_0$ , the wave number  $k_z = \frac{2\pi}{\lambda_w}$  of the wiggler with period length  $\lambda_w$ , the electron charge  $e$  and rest mass  $m_0$ , the speed of light  $c$  and the unit vectors in their respective directions  $\hat{y}, \hat{z}$ .

One interesting effect of a strong wiggler is its focusing effect in the vertical plane, which yields to a tune change [Wal83, Wal93, FEW<sup>+</sup>03]

$$\Delta\nu_y = \frac{\beta_y}{4\pi} K L \quad (2.21)$$

$$= \frac{\beta_y}{4\pi} L \left( \frac{e}{\gamma m_0 c} \right)^2 \langle B_y^2 \rangle \quad (2.22)$$

$$= \frac{k_u^2 B^2}{8\pi k_z^2 \left( \frac{p}{e} \right)} \quad (2.23)$$

$$\propto B^2 , \quad (2.24)$$

with the length of the wiggler  $L$ .  $K$  is the so-called undulator parameter or deflection-parameter, which is also-called wiggler (focusing) strength [Wal93] (not to be confused with the general focusing strength  $K = \kappa^2 + k$ ) and is defined as follows [Wie07]:

$$\langle K \rangle = \left( \frac{e}{\gamma m_0 c} \right)^2 \langle B_y^2 \rangle$$

$$K = \beta \gamma \theta = \frac{e B_0 \lambda_w}{2\pi m_0 c} ,$$

with the elementary charge  $e$ , the electron mass  $m_0$ , and speed of light  $c$ , and the maximum on-axis magnetic field of the ID  $B_0$ .  $\lambda_w$  is the period length of the ID and  $\theta = -\frac{e}{p} B_0 \frac{\lambda_w}{2\pi}$  the deflection angle, and  $\langle B_y \rangle$  denote the average of the vertical magnetic field component along the wiggler.

In the vertical direction the wiggler focuses like a quadrupole, but not in the horizontal direction. However, this focusing is a relatively weak focusing in comparison to that of focusing magnets (quadrupoles) which then is called strong focusing. The focusing mechanism is described now. In Fig. 2.8 on the following page the magnetic field inside of a wiggler is depicted in the graphic at the top. Particles that enter with a positive vertical

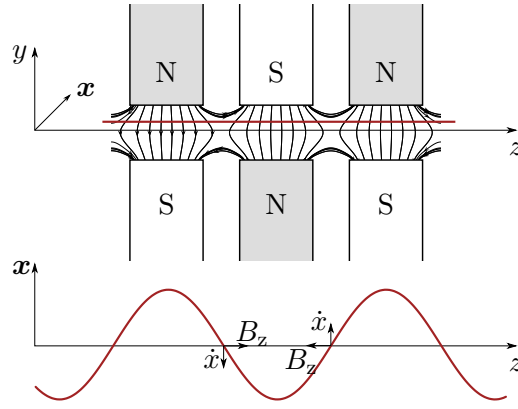


**Figure 2.8.: Edge focusing in the wiggler.** In the upper part three pole pairs of a wiggler are depicted as a side view with their magnetic field lines in between. In red a particle entering off-axis in the  $y$ -plane is shown. In the bottom plot the trajectory of this particle is shown in a on-top view. Also the velocity of the particle and the longitudinal magnetic field component  $B_z$  is shown. The additional  $B_z$  components cause an additional focussing force along the wiggler occurring only in the vertical plane.

offset see a finite longitudinal component of the magnetic field  $B_z$ , which is shown for two cases in the bottom plot. Particles moving with a negative offset see a field component with opposite sign. In the bottom plot the horizontal trajectory of a particle with a positive vertical offset is shown in red. Also the directions of the velocity at two distinct points are shown. One can see that the Lorentz force caused by the longitudinal component of the magnetic field  $B_z$  for this particle moving along the red line with the horizontal velocity component  $\dot{x}$  points into the paper plane, so towards the  $x$ - $z$ -plane. For a particle with a negative vertical offset the trajectory is the same, but the field components have a different sign and thus the Lorentz force points out of the paper plane, so also towards the  $x$ - $z$ -plane. In the central  $x$ - $z$ -plane there is no  $B_z$  component and therefore no additional Lorentz force. Because the  $B_z$  field is relevant at the edges of the pole pairs and between two pairs of them, this effect is called edge focusing.

Because the focusing is only in the vertical plane, a particle that enters with an angle or an offset should not be affected in the horizontal plane. However, if the horizontal width of the magnets is too small to provide a homogeneous field in  $x$  in the range where the electron beam is, a focusing or defocusing can occur. If so, a focusing effect occurs if the  $B_y$  increases with  $|x|$  and a defocusing one if it decreases [Smi86, Sch85], because the bending is stronger (weaker) at  $|x|$  with increasing (decreasing)  $B$ .

### Multipole components

Focusing changes the phase advance locally, so the phase advance between the chromaticity correcting sextupoles around the wiggler is different from the phase advance e. g. in the opposite straight section. Therefore third-order resonances (sextupole component) are introduced by the linear effect of focusing. This effect scales with  $1/\rho^2$ , see [Wal93, p. 825]. This scaling proportionality will be of interest when trying to distinguish different effects.

Higher-order multipole components show up in the Taylor expansion of the sine and cosine terms. These scale with  $k^2/\rho^2$ . Sextupole components for example can then cause a horizontal focusing and a vertical defocusing [Sch85].

It turns out that these effects scale proportional to  $1/E^2$  whereas the effect of field errors caused by fabrication inaccuracies scale with  $1/E$  [Wal93, p. 826]. Thus this fact can also be used to distinguish these intrinsic higher-order multipole components from field errors. The field quality of the wiggler typically is measured beforehand e. g. by measuring the *first* and *second field integrals*.

### Further higher-order effects

Additionally one can see higher-order effects like an increase of the **stopband** width, see Section 2.1.4 on page 8, also notable as a decrease of the dynamic aperture and therefore the lifetime of the beam. Furthermore, more important for this work is the higher-order effect “**amplitude-dependent tune shift, also-called detuning with amplitude (ADTS)**” [Smi86]

$$\Delta\nu_{\mathbf{u}} = \frac{1}{16\pi} \frac{k_{\mathbf{u}}^4}{k_z^2 \rho^2} L_w \beta^2 \left[ 1 + \frac{2}{3} \left( \frac{L_w}{2\beta} \right)^2 + \frac{1}{5} \left( \frac{L_w}{2\beta} \right)^4 \right] \varepsilon_x . \quad (2.25)$$

This can be written differently for the linear case and with the simplifications  $k_{\mathbf{u}} \approx k_z$  as well as the definition of the emittance  $\varepsilon_x$  (for the derivation see Appendix B.7 on page 105) [Saf89]

$$\frac{\Delta\nu_{\mathbf{u}}}{u^2} = \frac{\pi}{4} \frac{L_w}{\lambda_w^2} \frac{\beta e^2}{p^2} B \cdot B , \quad (2.26)$$

with the wiggler length  $L_w$ , and period length  $\lambda_w$ , the  $\beta$  function at the place of the wiggler, the wiggler’s magnetic field amplitude  $B$ , the beam momentum  $p$ , and the elementary charge  $e$ .  $u$  is the amplitude of the excitation and  $\nu_{\mathbf{u}}$  the corresponding tune.

This **ADTS** can also be used to examine multipole effects of the wiggler as described in Section 3.3.4 on page 31.



## 3. Experimental setup and methods

This chapter introduces the accelerator **KARA** at which the experiments were carried out, as well as the superconducting **CLIC** and **CATACT** wigglers which were used for the experiments. Then an overview of the methods used throughout this work is given and the links between these methods are presented.

### 3.1. **KARlsruhe Research Accelerator**

The **KARlsruhe Research Accelerator** (**KARA**) is a 110.40 m long electron storage ring with four times two symmetrical parts, called periods. In Fig. 3.1 on the following page the accelerator is sketched to scale. These periods are separated by so-called straight sections where no main magnets are located, but in which **Insertion Devices** (**IDs**) or infrastructure like the accelerating cavities or the injection line are installed. Each period consists of two bending magnets, five quadrupole magnets, and three sextupole magnets of which two are of the same kind—the vertically focusing ones. Two mirrored periods form a sector, sometimes called super-period. The straight sections between the sectors are longer than the straight sections between the mirrored periods and can thus provide more space for **IDs**. Two of the short straight sections are filled with the acceleration cavities and the straight section at the bottom left in Fig. 3.1 on the next page is used for the injection from the booster.

The electrons are injected into the main storage ring from the booster ring with a beam energy of 0.5 GeV. Then the beam energy is increased to the final operation energy, which typically is either 1.3 GeV or 2.5 GeV.

The typical operation mode of **KARA** for synchrotron light users is at 2.5 GeV. In this “user operation” all **IDs** are in their state of a high magnetic field to provide synchrotron radiation to the beamlines. In this work, the term “normal operation mode” refers to the 2.5 GeV case with all **IDs** in their zero-field mode.

One quarter of this optics is shown in Fig. 3.2 on page 25, simulated with *elegant*. The magnetic lattice is typical for double bend achromats that have zero dispersion in the straight sections. In favour of a smaller emittance the dispersion is not kept zero in the straight sections [HKB<sup>+</sup>05], so that **KARA**’s typical operation mode uses distributed

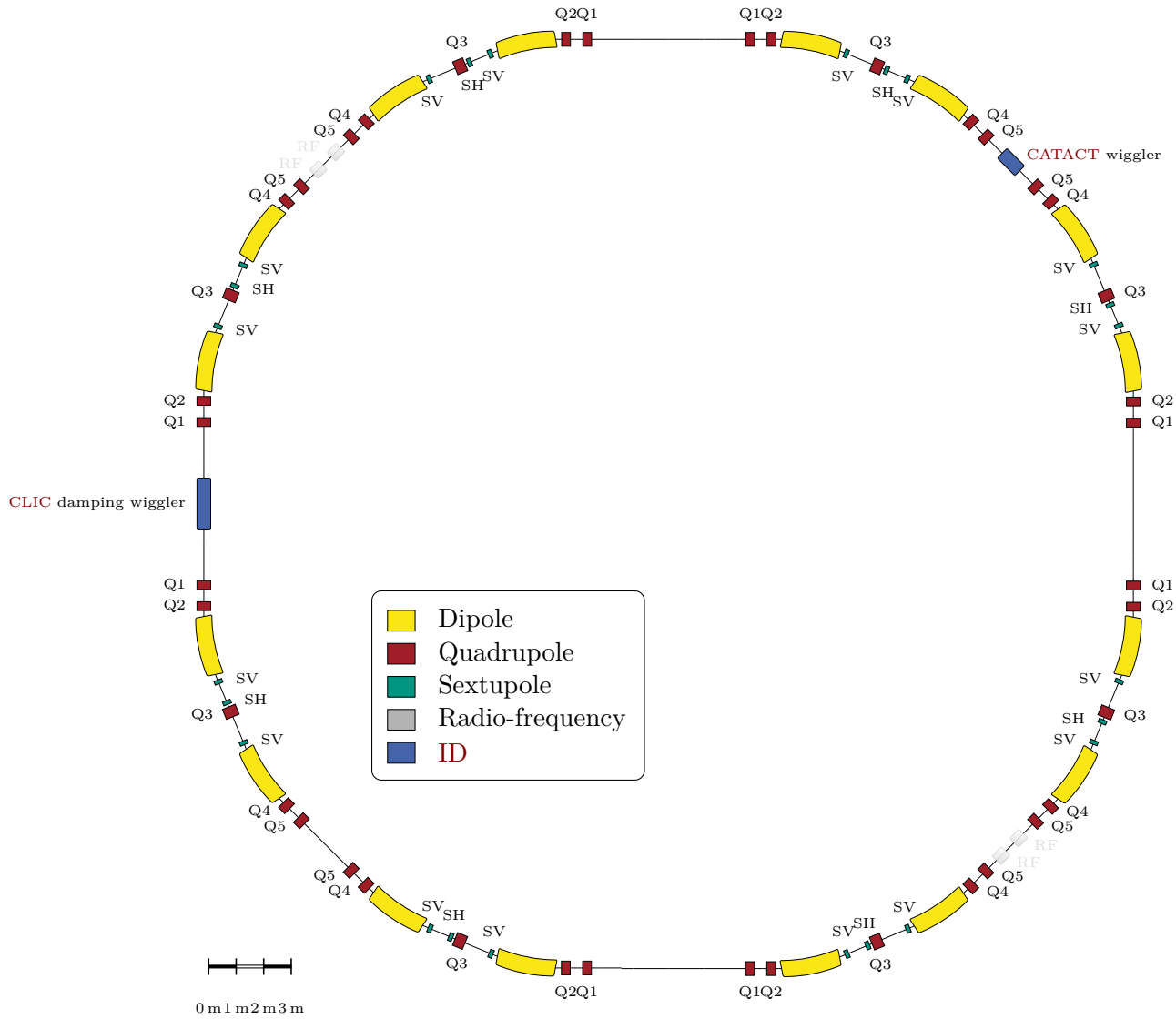


**Figure 3.1.: Magnetic lattice of Karlsruhe Research Accelerator (KARA).** The magnetic lattice of KIT’s electron storage ring KARA is depicted. Electrons circulate clockwise after being injected into the ring in the short straight section in the bottom left corner. As in the real machine the ring’s bending magnets are shown in yellow, its five quadrupole families  $Q\#$  in red, and its horizontal and vertical sextupoles  $SH/SV$  in green in this sketch. The CLIC damping wiggler and the CATACT wiggler with which experiments were done are depicted in blue. Also the four accelerating radio frequency cavities are included in this sketch.

dispersion optics. This can be seen in Fig. 3.2 on the next page where the dispersion  $\eta_x$  (red/dash-dotted line) nearly reaches 0.40 m in the long straight section at  $s = 25$  m.

Another typical electron beam energy at which KARA is operated is 1.3 GeV. At this energy there exists a special operation mode with short bunches, that is often referred to as *low- $\alpha$*  mode. It will be discussed in more detail in Chapter 7 on page 81 where the effects of the wiggler on the beam in this mode are discussed, too.

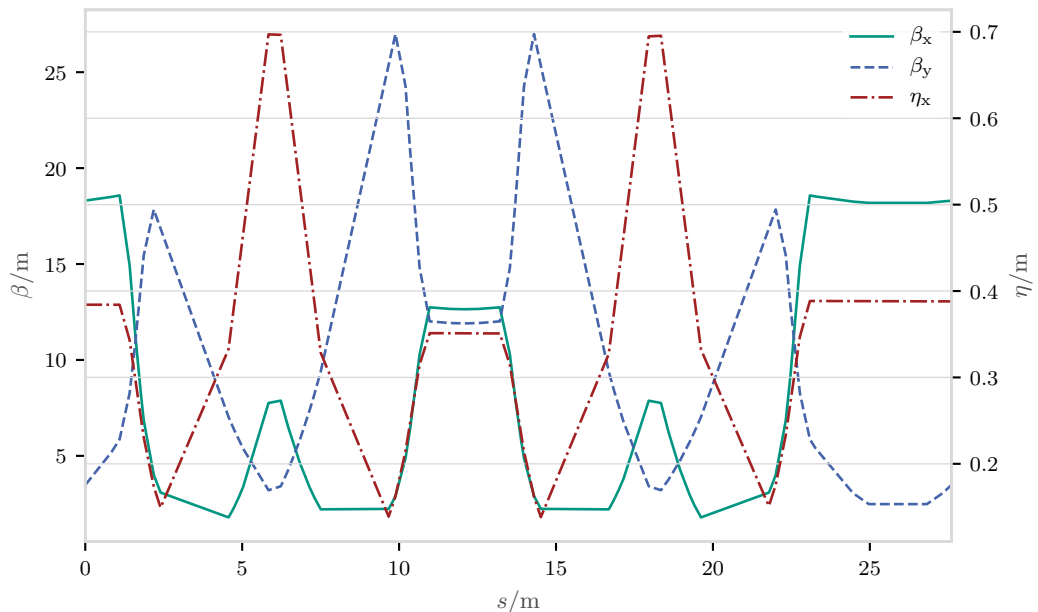


**Figure 3.2.: KARA's normal operation lattice.** *elegant* simulations of one quarter of KARA's lattice for the 2.5 GeV mode. The horizontal (solid, green) and vertical (dashed, blue) beta-functions stay below 30 m. The dispersion (dash-dotted, red; right axis) is also positive in this case, but is small 0.70 m compared to beta functions. The plot shows the long straight section, where e.g. the wiggler is positioned, as one section at the right of the plot and not as it is often the case symmetric to the center of the straight section.

**Table 3.1.: KARA parameter for the three common operation beam energies.** Parameters taken from [Keh19].

Energies $E$	GeV	0.5, 1.3, 2.5
Circumference $C$	m	110.40
Bending radius $\rho$	m	5.56
Vacuum chamber height $h$	mm	32

The aforementioned important parameters of KARA are summarised in Table 3.1.

### 3.2. Wigglers in KARA

In this work two superconducting wigglers produced by Budker Institute of Nuclear Physics (BINP) are used for experiments. Both of them are constructed with horizontally wound racetrack coil pairs. Nb-Ti multifilament wires with a copper matrix are used for these windings. The coils are directly wound on iron poles, each 15 cm wide. The end field configuration to compensate the field-integrals is of the kind  $1/4$  strength,  $-3/4$  strength. The vertical aperture of the beampipe inside the wigglers (13 mm and 15 mm, respectively) are much smaller than the vacuum chamber height in the rest of the storage ring (32 mm), see Tables 3.1 and 3.2 on the current page and on the following page.

The CATACT wiggler provides a maximum magnetic field of 2.6 T and a period length of  $\lambda_w = 48$  mm, resulting in a maximum undulator parameter  $K = 11.65$ . It has 34 full field

**Table 3.2.: Wiggler parameters.** Parameters taken from the technical reports [MVS<sup>+</sup>16, MVS<sup>+</sup>12].

Parameter	Unit	CLIC	CATACT
Period length $\lambda_w$	mm	51.4	48
Max. magnetic field $B$	T	2.9	2.6
Vacuum gap $g$	mm	13	15
Magnetic gap $g$	mm	17	19.4
Vacuum chamber width	mm	75	60
Magnetic length $L_w$	mm	1836	900
Pole width	mm	150	150
Number of full field poles		68	72
Super conductor		Nb-Ti	
End field configuration		1/4, -3/4	

periods resulting in a magnetic length of 0.90 m. The wiggler was installed in 2014 in the remaining short straight section and serves as a light source for the catalysis and actinides beamline.

The **CLIC** damping wiggler is 1.84 m long, so more than twice as long as the **CATACT** wiggler. It is located in the long straight section in the west, depicted on the left side of Fig. 3.1 on page 24. As it is not only designed to serve as a light source for the IMAGE beamline, but also as a prototype of a damping wiggler for the **CLIC** damping rings, it has a higher magnetic field of 2.9 T. Its period length is  $\lambda_w = 51.4$  mm. That means that it has got an undulator parameter of  $K = 13.92$ .

It is the first conduction cooled superconducting wiggler. That means, one can exchange or repair it relatively easy, which is crucial for the large scale of damping rings and convenient for testing different prototypes. Hence, this cooling concept was also part of investigations. Though the wiggler could reach the design magnetic field of 3 T with a period length of 51 mm in a LHe-bath, the magnetic field could not be reached in the wiggler's own cryostat. Therefore the maximum field was decreased and the period length increased, to avoid quenching during operation. It was the first result for **CERN** of the test of maturity of the technology, that conduction cooling works for wigglers, but not for the design parameters. This was even before installation. Besides testing the maturity of the technology, **CERN**'s second major interest in this prototype was the tolerance against heat-load produced by the upstream wigglers' synchrotron radiation, and the influence of the wiggler on the beam dynamics. In the damping rings proposed for the **CLIC** project there are 26 damping wigglers in a row. Wigglers downstream of the other wigglers see the light of the upstream ones which results in additional heat-load. In addition to this expected large heat-load the wiggler has got a cooling concept which is novel for wigglers.

In Table 3.2 the important parameters of these two wigglers are summarised.

### 3.3. Measurement methods

In the following some measurement techniques that were used during this work are presented in more detail. We start with the measurement of the optics parameter tune and chromaticity at **KARA**. Then higher-order multipole measurement techniques, local orbit bump and amplitude-dependent tune shift (**ADTS**) measurements, follow. Finally, the optics reconstruction technique Linear Optics from Closed Orbits (**LOCO**) is presented.

#### 3.3.1. Tune measurement

At **KARA**, the tune can be measured with a bunch-by-bunch feedback system [HHH<sup>+</sup>14, Dim20].

A bunch-by-bunch feedback system acts against beam oscillations on a turn-by-turn basis. Such systems measure the oscillation of the beam position with one **BPM** at a certain position in the ring. Then they process the signal and calculate the feed back with which they act onto the beam with the dominant frequencies using a strip line. This strip line is located at a different position than the **BPM** in the ring. This feedback is measured to get the frequencies the beam would oscillate with if it was not stabilized by the feedback system. As discussed in Section 2.1.4 on page 8 for the text-book tune measurement where the excitation of the beam results in a peak at the betatron oscillation frequency in the oscillation spectrum, a notch in the spectrum measured by the feedback system is visible, because of the internals of the feedback systems' feedback-loop. In Fig. 3.3 on the next page the full oscillation spectrum is shown. The notch, indicated by the point, is located at the betatron oscillation's frequency. Here the frequency of 509.53 kHz corresponds to a fractional tune of  $\nu_y = 0.8124$ , calculated as discussed in Section 2.1.4 on page 8. The systematic uncertainties of the readout system are of very different nature and strongly dependent on the accelerator settings and thus hard to quantify in general. On the one hand, they consist of ones that are specific to this system, like the resolution of the spectrum, the asymmetry and shape of the notch and the signal to noise ratio that can be influenced by the feedback strength. On the other hand, uncertainties like averaging the tune over all bunches exist. These kind of uncertainties also occur at other tune measurements. Since these uncertainties are very dependent on the settings of the system these settings have to be checked and optimized before each measurement. Therefore these systematic uncertainties will be discussed for each measurement separately, and only statistical fluctuations are provided in plots and tables in the following.

#### 3.3.2. Chromaticity measurement

Unlike the tune, the chromaticity cannot be measured directly because the momentum of the particle is not known from direct measurements. Thus the chromaticity must be derived by measuring the tune  $\nu_u$  as a function of the radio frequency  $f_{RF}$  at a known momentum compaction factor  $\alpha_c$ . The chromaticity is yielded by a polynomial fit, typically

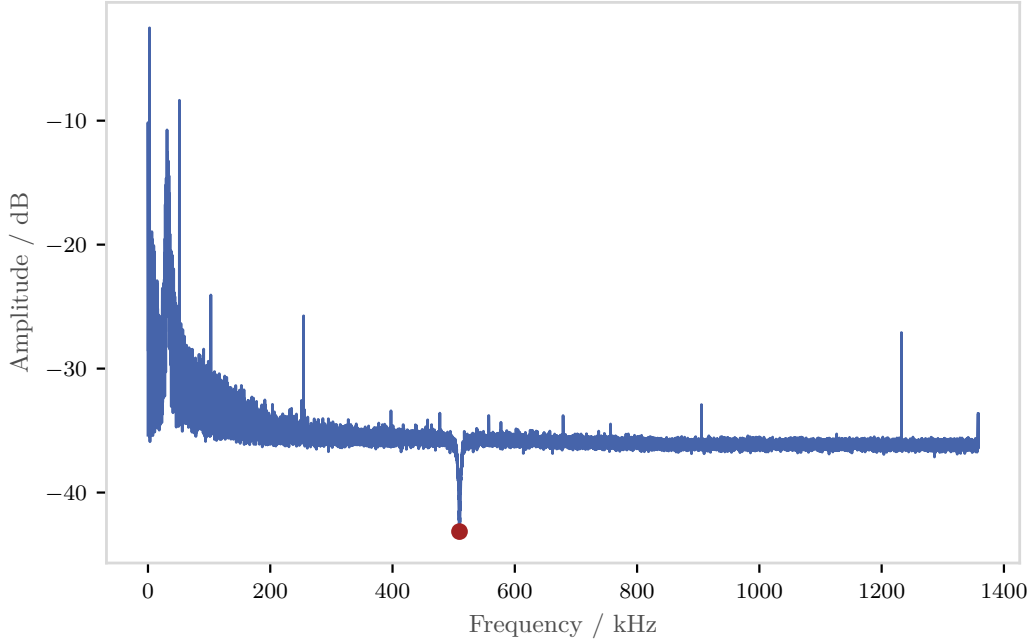


**Figure 3.3.: Notch of the vertical tune in the feedback system data.** The spectrum of the vertical betatron oscillation is displayed. A notch with its minimum marked as a red point indicates the betatron frequency from which the fractional tune is derived. It results from the internal processing of the feedback loop of the bunch-by-bunch feedback system.

of second-order, to the data, together with the relation for the first order (cf. [Bra09]):

$$\xi_{\mathbf{u}} = \frac{\partial \nu_{\mathbf{u}}}{\partial \frac{\Delta p}{p_0}} = \frac{\partial \nu_{\mathbf{u}}}{-\partial \left( \frac{1}{\alpha_c} \frac{f_{\text{RF}} - f_{\text{RF}}^c}{f_{\text{RF}}^c} \right)}. \quad (3.1)$$

Here  $f_{\text{RF}}^c$  denotes the central frequency—the radio frequency corresponding to the reference tune  $\nu$ —and  $f_{\text{RF}}$  a slight variation thereof, so the radio frequency causing the particle to change its momentum. The momentum compaction factor has been measured at **KARA** for different energies [Cha16]. Though these values were measured at optics different from these of this work, Miriam Brosi found a factor that connects the measured momentum compaction factor, the set value of the radio frequency and the measured radio frequency [Bro20]. With this factor these measured momentum compaction factors can be used and were used in the short-bunch mode measurements. Nevertheless, for the simulations and chromaticity measurements done not in the short-bunch mode, the momentum compaction factor provided by optics simulations is used.

For practical chromaticity measurements at **KARA** when the feedback signal or the excitation cannot be strong, or other resonances dominate the frequency spectrum, notch or peak finding might fail. This causes single tune values to jump. SciKit-Learn’s [PVG<sup>+</sup>11] implementation of the RANSAC algorithm [FB81] was used to automatically detect the outliers. The Random sample consensus (RANSAC) is an algorithm that randomly samples minimal data points of the measurement to fit a model and votes for or against it. It

iteratively takes a minimal sample, fits this to a model and adds all points within a certain threshold that can be described by this model to a set named consensus and compares the consensus set with the largest consensus so far. After a certain number of iterations a fit with all data from the largest consensus is done and data points not fitting this best model are rejected as outliers. It relies on not too many data points to be missing to describe the model, but is robust against many outliers. In the case of the chromaticity measurement the outliers are spoiled tune readouts at single disturbed frequencies ranges. Since at first all data points are recorded in the chromaticity measurement, RANSAC is applied in the post-processing to reject the outliers from the point set used for fitting to the second-order polynomial. The uncertainties of the fit are calculated using the bootstrapping method [Efr79].

### 3.3.3. Orbit bump measurements

One method for investigating higher-order magnetic momenta of the wiggler field, which were discussed in Section 2.1.6.1 on page 20, is the orbit bump measurement.

For the orbit bump measurements the beam was transversely shifted inside the wiggler. For this purpose four corrector magnets per transverse plane were used, to get a displacement that is parallel to the reference orbit. Though this method is called *local orbit bump*, the bump is located not only around the wiggler itself, but also affects the orbit position in the neighbouring magnets. There are only 16 vertical corrector magnets and 28 horizontal ones around the ring. This implies that in the case of vertical bumps the beam passes a quadrupole with an offset, and even worse nearly an eighth of the ring with an angle and an offset. The positions of the corrector magnets that are used for shifting the orbit are depicted with italic cyan labels in Fig. 3.4. In the same figure the CLIC damping wiggler's position is located at the top left. The horizontal corrector magnet closest to the wiggler has no magnetic elements in-between, but the farthest horizontal corrector is located two quadrupoles of different families, one sextupole and one dipole away, which means at least one of each magnet type. That means a beam passes all magnetic fields with an additional angle and many with an additional offset, before passing the wiggler.

As can be seen in Fig. 3.5 not only the orbit between the corrector magnets used for displacing the orbit locally is affected, but the orbit around the whole ring.

The orbit bump itself is realised utilising the respective mechanism of the control system [ZKPS02].

Though the set values of the bumps are supposed to correspond to shifts of the orbit at the wiggler's location in steps of 0.50 mm or 1 mm, the BPM read-back deviates from these set values, as can be seen in Fig. 3.6 on page 32. Thus the "actual bump height" needs to be calculated as the difference of the absolute maximum displacement of the orbit measured within the bumping area (red line in Fig. 3.5) and the mean unperturbed orbit in order to see the effects of local orbit change and not the global. As an example the supposed orbit



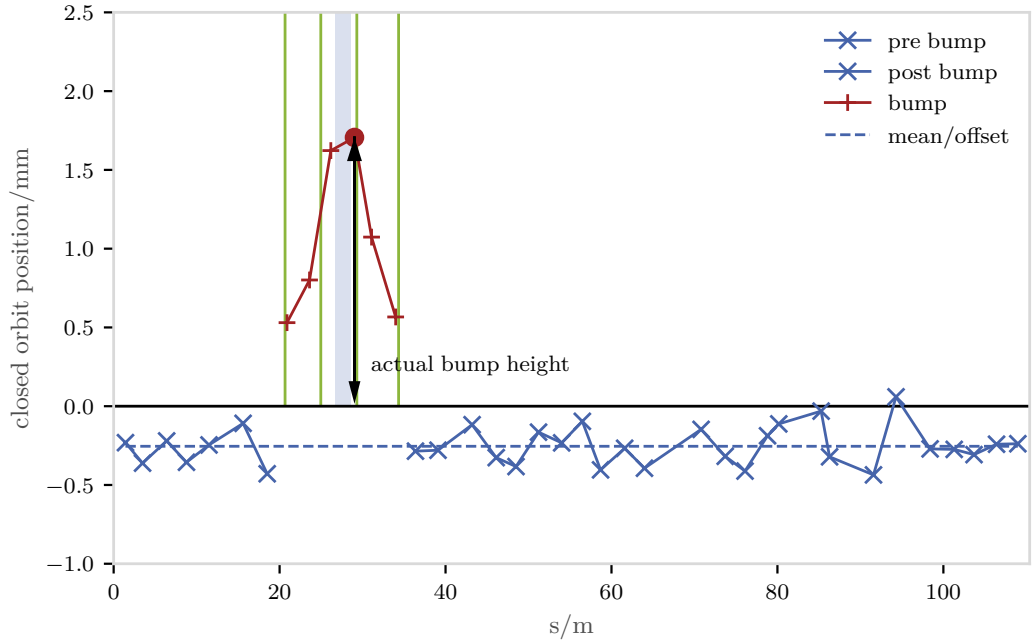


**Figure 3.5.:** Example of the orbit bump procedure. Each cross indicates a **BPM** measurement of the orbit. The beam is displaced around the wiggler whose position is indicated by the light blue area. For the bump four corrector magnets, indicated by the light green lines, are used. The mean of the orbit outside of the displacement area, blue dashed line, is also shifted with respect to the original mean (black line). The connecting lines between the crosses are for visualisation purposes only. Also published in [GBB<sup>+</sup>17].

- wiggler without field;
- wiggler at high field.

Because ramping the wiggler's field up and down takes much more time than bumping the beam, all measurements at one wiggler field were done before increasing the field to minimise time-dependent effects within a data set for one wiggler field.

### 3.3.4. Amplitude-dependent tune shift measurement

A different method used for investigating higher magnetic momenta of the wiggler field is the amplitude-dependent tune shift method. This method is based on tune measurements depending on the betatron oscillation amplitude. The amplitude of the oscillation can be modified by kicking the beam with different strengths. For kicking the beam at **KARA** the first of three injection kickers was used to have one dedicated kick. However, the duration of one kick is 7 turns. This causes already kicked particles to be kicked again, so that the momentum and position of the particle are changed depending on the lattice. Furthermore, the kick strength must be measured with **BPMs**, because it is not known from the kicking magnets themselves. The **BPMs** measure the kick for about 1750 turns. Such a measurement is repeated for 20 times to get statistics and compensate fluctuations of individual kicks. To get a kick dependence one must either measure at different kick strength, or one can measure at a certain kick strength and shift a small window along the

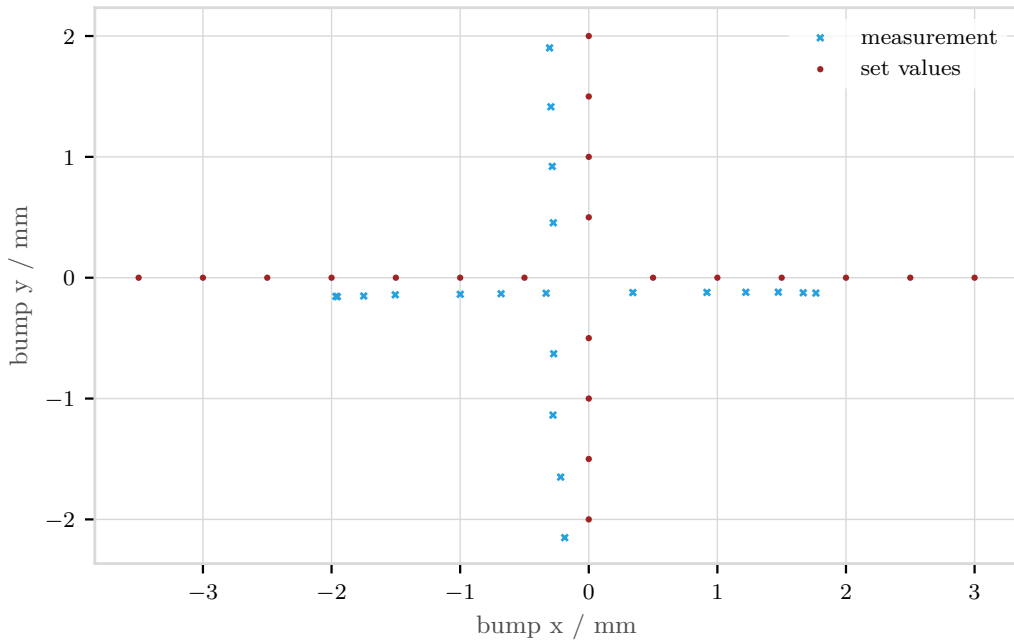


**Figure 3.6.: Difference between the set values and the real bump.** The red points show the set values of the bump amplitude and the light blue crosses the corresponding post processed bump amplitudes. In the horizontal plane the steps between the measurement points get closer for larger bumps/offsets. Measurement points are slightly shifted in both planes.

damped oscillation signal so that different windows represent different amplitudes. Both techniques were used for comparison. The kick must not be too strong in order not to get into a regime of non-linear excitation or even worse to lose parts of the beam, but of course it must be strong enough to see an effect.

With this measurement technique it is possible to see octupole components of the wiggler field as a quadratic dependence of the tune shift on the kicking amplitude, as elaborated in [SLT<sup>+</sup>02].

### 3.3.5. Linear Optics from Closed Orbit

Often it is useful to get a model of the real storage ring at a specific state, e. g. like in this work when one wants to compare a model with measurements and the accelerator settings might vary from one measurement campaign to another. One method has been developed by James Safranek [Saf97] that is called Linear Optics from Closed Orbit (**LOCO**) and provides the quadrupole strength, so the linear optics, of a lattice from a measurement. The transfer matrices of each magnet or magnet family of a storage ring are fitted to a measured transport matrix. By varying correction magnets strength and measuring the response on the **BPMs** a so-called **Orbit Response Matrix (ORM)** can be created. The transfer matrix representation of the storage ring needs to be fitted to the inverted **ORM**. The fits are done for a set of different quadrupole configurations and then the overall best fit is taken.

Because there is no linear connection between the quadrupole strength and the **ORM**, the optimization cannot be of a simple gradient descent type, so this sampling approach is used. This method's performance might be affected by **ORM** matrices with low dimensions, or suboptimal input values of the **ORM**. As **KARA** is a small ring it has few **BPMs** and corrector magnets and therefore a small **ORM**. Furthermore, at low energies the corrector magnets cannot be operated at high fields, because the beam is less stiff. Then the corrector magnets might show hysteresis effects at the lower fields. Also non-linear regimes occur earlier in fragile accelerator setups where the energies are lower, resonances are closer or the closed orbit is not in the centre of the beam pipe.

This method was used as a starting point, but did not result in tunes that match the measured tunes to the measurement uncertainty for the 1.3 GeV lattice. Anyhow it turned out that even a relatively bad **LOCO** fit can provide a good starting point for optics fits with elegant with respect to the tunes and chromaticities.



## 4. Including wiggler models into the storage ring **KARA**

### General remarks and conventions

For beam dynamics simulations three different simulation codes that are designed for electron accelerators, especially synchrotrons, have been used for three different purposes. **Matlab Accelerator Toolbox** [Ter01] (**AT**) was used for **LOCO**-fits and as a reference, because it is used as the internal model for running **KARA**. **AT** is a software often used by and developed by accelerator physicists at light sources around the world. At **KARA** an **AT** based model is used as an internal model, e.g. for beam-based alignments of the orbit and for measurements of the **ORM**. Therefore it makes sense to use **AT** to get simulation-based accelerator parameters for individual measurement campaigns. However, this code does not include insertion devices.

Another tracking code, Methodical Accelerator Design 8 (**MAD-8**) [Sch97], was used in-between as a benchmark for some tracking studies in the short-bunch mode. It was developed at **CERN** for **LEP** and was succeeded by **MAD-X** for **LHC** which focussed on proton accelerators. Since measurements in the small bunch operation mode, see Chapter 7 on page 81, have already been simulated with a **MAD-8** model in the past, these models could be used to benchmark against *elegant*.

*elegant* [Bor00] was used for most of the simulations, because it offers wiggler implementations. In fact it provides three different implementations to simulate wigglers. It is a 6d tracking and optics simulations code developed at the Argonne National Laboratory for their accelerators ranging from linear accelerators to a synchrotron light source.

### Naming conventions

In the following, three different Fourier representations of the wigglers' magnetic field data are compared. As they differ in the point of termination of the expansion the names used in the following reflect this. To make the text easier to follow the representation with only the fundamental harmonic is abbreviated as **F-0**, the one with very many Fourier components generated by an iterative approach using **FFTs** as **F-N**, and the one with a decent amount of Fourier components generated by fitting as **F-4**. They will be described thoroughly in this chapter.

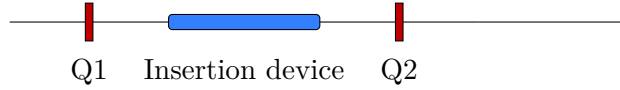


**Figure 4.1.: Sketch of the test case.** Sketch of the test case used for wiggler comparisons. 1 cm equals 1 m in the simulation. The start and end are connected, such that a periodic structure is defined and properties of a ring—tune, chromaticity—can be calculated.

**Table 4.1.: Test case configuration.** Configuration of the test case for the wiggler implementations and field representations.

Wiggler field $B$ / T	1
Field configuration	Opera 3d field
Period Length $\lambda_w$ / m	variable
Periods	200
Length $L$ / m	2
$k_Q/\frac{1}{m}$	$\pm 0.50$
$L_Q/m$	0.10
$L_{d1}/m$	1
$L_{d2}/m$	2

## Test case optics

To test *elegant*'s different wiggler implementations a simple optics model is used that can introduce some non-linearities, but is simple enough to see mainly the effects caused by the wiggler. This optics model is structured as shown in Fig. 4.1 and Table 4.1 is a ring consisting of two quadrupoles and two straight sections of which one is filled with the wiggler. It is used for tune calculations for intermediate results of the fit of Fourier components. It is modelled as a closed ring to provide symmetric boundary conditions to be able to have tunes and chromaticities.

### 4.1. Choosing a field representation

In this chapter different ways of describing a wiggler in the computer code *elegant*, and different mathematical representations of the wiggler field are compared to each other and summarised in Table 4.2 on page 48. Based on this comparison the decision to choose *elegant*'s wiggler implementation CWIGGLER is made and to use two different Fourier representations for the CLIC damping wiggler and the CATACT wiggler.

At first, different representations of the wiggler field used in the simulations are presented. Afterwards, the different wiggler implementations that can handle these representations are compared.

For the CLIC damping wiggler there is one field data set available which is exported from a magnetic field map simulation of a short model of the wiggler. For the second wiggler dealt with in this thesis, the CATACT wiggler, there are two sets of field data available. The first field data set is a measured field of a short model of the CATACT wiggler. The second field data set used for the comparison is the simulated field data set of the short

model of the **CATACT** wiggler. With these two different field data sets of the same device and measurements it is possible to compare the implementations and to see how the input field quality affects the simulation results.

*elegant* does not expect the field data sets to be given as raw magnetic field components  $B_i$ , but as a list of Fourier components  $C_{mn}$  and corresponding wave numbers  $k_u$  of the Fourier series [Bor]

$$B_y = |B_0| \sum_{m \leq n}^N C_{mn} \cos(k_{x,1}x) \cos(k_{z,n}z) \cosh(k_{y,m}y) \quad (4.1)$$

representing the field. This implies that the field data sets have to be transformed into this format first.

In the following different transformations to this representation are discussed starting with only one harmonic Fourier component (F-0), then multiple Fourier components (F-N).

### **Fundamental harmonic / F-0**

The simplest solution to represent the field is to use only one Fourier component which then can be directly calculated for given  $B_0$ ,  $C_{mn} = 1$  and the idealized  $k_z = \frac{2\pi}{\lambda_w}$ . This solution does not provide more information to *elegant* than a purely analytical solution does. Especially no information about individual field characteristics of this specific device is provided. The exact input can be found in Appendix B.7 on page 103.

### **Many Fourier components / F-N**

In contrast to using only one component, so to take the purely analytical theoretical approach, there is an advantage in using multiple Fourier components. Therefore the aforementioned existing field data have been transformed in [Get14] following the procedure described in [Wol01]. A Fourier transformation of the field data set of the  $x$ - $y$ -plane is done and afterwards the Fourier components are approximated iteratively to match the field data set in all three dimensions. The approximation is necessary, because for the vertical axis  $y$  there are only very few data points (8), though these components are highly sensitive to variations, because of its dependence on the cosh, see Eq. (4.1). One iteratively minimises the difference of the calculated  $B_y$  for the Fourier coefficients and the values of the data set to less than  $10^{-16}$ . The minimisation is done in four steps. Firstly Eq. (4.1) is represented as a matrix  $F_{ij} = \cosh(k_{y,j}y_i)$  for  $x = z = 0$ . The dimensions are the number of data points in  $y$  rows and the number of wave vectors  $k_y$  columns. The inverse hereof  $F_{ij}^{-1}$  is multiplied with the difference vector of the measured and calculated  $B_y$ . That provides us with the variation of the Fourier components  $\vec{\Delta c} = -F^{-1}\vec{\Delta B_y}$ . Now new Fourier components  $C_{m,n}$  are calculated and inserted into Eq. (4.1) to get the  $\vec{B}_y$  for the next iteration.

This method is less sensitive to variations in  $y$  than e.g. a simple **FFT**, because of the iterative approach. However, it is still error-prone for very few data points in  $y$ .

The resulting field representation has got 550 Fourier components which is the highest approachable result with this technique that is not limited by *elegant*'s input limit of 1000.

### Fit / F-4

The last approach to represent the field data is the “F-4” approach which will be described in more details in the following section.

### Few Fourier components of the wiggler's field / F-4

Now the F-4 method of generating the right representation will be described in more detail, starting with a small motivation for the necessity of it.

The originally designed wiggler and the finally installed wiggler differ in some aspects. The installed wiggler has got a period length of 51.4 mm instead of 51 mm and can only reach a stable field of 2.9 T instead of 3 T in its own cryostat. This means that the existing model of [Get14] based on the procedure described e. g. in [Wol01] does not exactly fit the real situation, because for the CLIC damping wiggler no data with this changed period length are available. Furthermore, the F-N modelling procedure also turned out to be numerically unstable and not appropriate for the field data set of the CLIC damping wiggler that is smaller than that of the CATACT wiggler which was used in [Get14].

Hence a different method was used to get a representation of the magnetic field for the *elegant* code. The Fourier series Eq. (4.1) on the previous page were directly fitted to the data obeying Maxwell's conformity condition  $m^2 k_y^2 = n^2 k_z^2 + l^2 k_x^2$  with the transversal wave numbers  $k_x$  and  $k_y$  and integers  $n, m$ . With this additional restriction the number of fitting parameters could be reduced significantly and thus the fitting stability could be increased. Because in the input file for the tracking code the parameter  $k_z$  was given as a fixed parameter and not calculated for each component, this parameter was also taken as a fixed parameter in the fitting procedure. With these restrictions the number of free parameters is reasonable compared to the number of data points.

As a fitting initialization the F-0 case was used. For fits with more Fourier components higher-order components were added iteratively, and the best fit from the run with one order below was used as the starting point. A fit was considered good if the deviation of the fit from the data is minimal firstly and if the optics simulations were successful, too. That means the tune and chromaticity must change similarly to optics changes without the wiggler when changing the optics slightly, so the results must be robust against minimal changes in the optics simulations. This tends to be the case for few Fourier components. Therefore a second condition was, that the Fourier series still has to have more than just the first Fourier components to be able to represent also higher-order effects.

Fig. 4.2 on the facing page shows the Fourier coefficients  $C_{mn}$  depending on the number of fitted Fourier components. The higher components that are added are very small for  $N \geq 6$ , but make the fit unstable—especially  $C_{1,3}$  jumps for higher  $N$ . Therefore it does

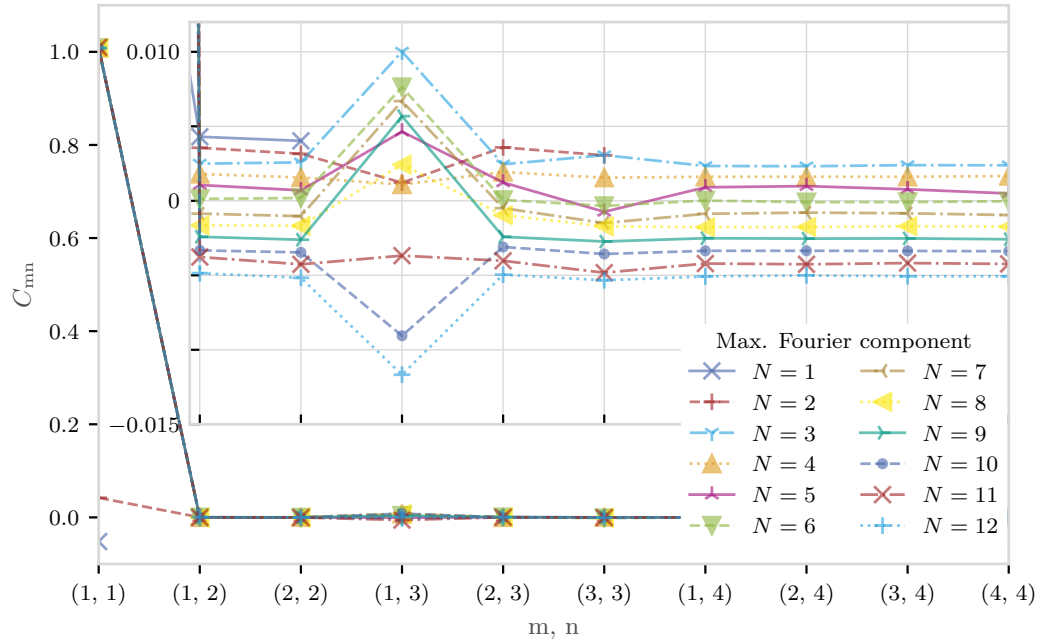


**Figure 4.2.: Dependence of  $C_{mn}$  on  $N$ .** Fits of the Fourier series with a fixed number of Fourier components to the field data of the CLIC damping wiggler short model result in different Fourier components  $C_{mn}$ .

The individual graphs are shifted by  $0.005 - 0.01/12 \cdot (N - 1)$  for better visibility. The component  $m = 1$ ,  $n = 3$  shows changes for all simulations. After  $m = 1$ ,  $n = 4$  no larger differences are observable anymore. The lines for  $N = 1$  and  $N = 2$  do not have the first component at  $C_{mn} \approx 1$ .

not make sense to add more components than  $N = 6$ . However,  $N \geq 3$  is necessary to have also  $C_{1,3}$  represented which is large compared to the other higher-order components. The final choice of  $N$  was done after beam dynamics simulations.

Beam dynamics simulations were performed and analysed using these fits, because a fit of the field does not give direct insight into the behaviour of the beam dynamics simulations that use these fits. Tunes were calculated with *elephant* for the test model, described in Chapter 4 on page 36, using the data sets representing the wiggler's field that were generated by the fits with different numbers of Fourier components. These tunes are shown in Fig. 4.3 on the following page.

For the fit for  $N$  the result of the fit of  $N - 1$  was used as input parameters up to a run with  $N = 12$ . For even higher  $N$  fits were done with the same start parameters as for  $N = 1$ . This is, because these fits were done in parallel to search for different local minima that might have resulted in convergent tunes. This was not the case nor is there a trend (increasing or decreasing) for the tunes for  $N \geq 12$  recognisable which might have been an indication for a local minimum. Therefore better results for even more Fourier components are not expected.

A closer look at the interesting region of  $N = 3$  to 6 shows that the tunes converge from  $N = 4$  on. As one does not gain more accurate results for higher-order Fourier components

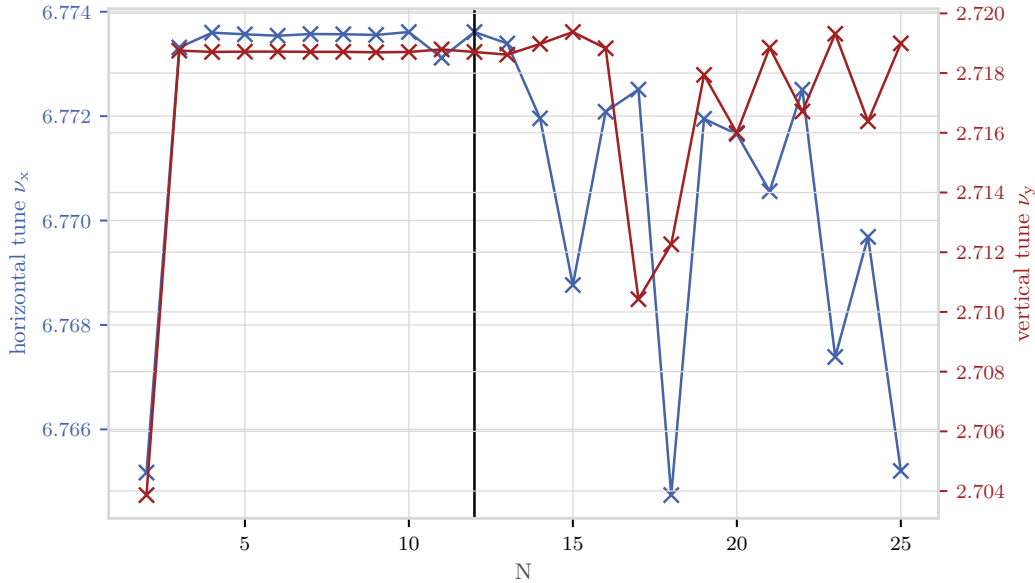


**Figure 4.3.: Tune depending on the field components generated with different  $N$ .** Simulated tunes for different input field components generated with different Fourier series upper limits  $N$ . For  $N \geq 12$  the initial parameters of  $N = 1$  were used for the fitting routine. For  $N < 12$  the results of the fit of  $N - 1$  was used to initialise the fitting routine. Though the values vary a lot for  $N \geq 12$  no trend indicating changes from the converged tunes  $N \leq 10$  are visible.

than of the order  $N = 4$  as is depicted also in Fig. 4.3 the solution with  $N = 4$  is the best fit and therefore used. In the end, a field-representation for further simulations could be found that is based on the simulation data of the short model of the wiggler. This representation is a compromise between the robustness of the simulation results and the accounting for higher-order field components.

## 4.2. Comparison of three wiggler implementations available in the *elegant* tracking code

The tracking and optics simulation software *elegant* offers different implementations of wiggler representations. In the following section three different implementations of modelling wigglers (WIGGLER, GFWIGGLER, and CWIGGLER) are described. Then their simulation results are discussed and the decision to choose the CWIGGLER implementation is justified.

Particle tracking in accelerator codes typically works by numerically integrating the path through all passed elements. For this the magnetic fields are evaluated at a certain number of points and the movement of the particle is extrapolated. Wigglers with their inhomogeneous fields therefore typically need a lot of evaluations to achieve accurate results in comparison to the main magnets of an accelerator. In rings this problem becomes more severe, because these evaluations have to be done for each turn.

### 4.2.1. Description of the implementations

#### Sinusoidal CWiggler and Wiggler

One implementation is available as the pure “sinusoidal CWIGGLER” and as WIGGLER. This implementation cannot make use of field data and it does not include any higher-order field components. It simply uses the pure analytical first order formulas to calculate the effects of the wiggler on the beam. It will only serve as a reference of an ideal wiggler for comparisons with the other implementations, because of the lack to describe higher-order effects.

#### GFWiggler

The GFWIGGLER implementation uses an analytical approach based on Taylor expanded generating functions of type  $F_3(p, Q, t)$ . In general, it applies a known solution of a generating function for arbitrary magnetic fields, see [BW11], for the specific case of a Fourier representation of the magnetic field. Such a specific case of a Fourier representation of a wiggler field is the implementation of that algorithm in *elegant*. By this solution for  $(z, -p_z)$  the field and cartesian momentum dependent Hamiltonian  $\tilde{\mathcal{H}}(\vec{p}, \vec{A})$  transforms into one that depends on the transverse location and momentum of the particle  $\mathcal{H}(x, p_x/p_0, y, p_y/p_0)$ . Using the latter Hamiltonian the trajectory of a particle can be tracked through the wiggler. Though one integration step is computationally more expensive than for simple numerical integration of the equation of motions for that particular magnetic field values, this method is faster. This is because one integration step can be chosen to be longer for the same resulting accuracy. In fact, the effect of the magnetic field on the charged particle can be described for a distance that may be longer than one period with the generating function approach. That is in contrast to typical tracking routines where many kicks per period are integrated over, which is very expensive in terms of computing time for strongly varying fields—like in wigglers. So the resulting speed-up of the GFWIGGLER method is beneficial for many turn tracking studies.

Note that the solution of the transformation makes use of a small-angle approximation and expects an even number of poles which is both compatible with our case.

#### CWiggler

Another implementation that can handle field data represented as Fourier components and wave numbers is the CWIGGLER [WFR03, Wu04]—not to confuse with the “sinusoidal CWIGGLER”. It explicitly integrates numerically over a quadratic Hamilton function representing the field data. Because it is explicitly integrating similarly to Ruth’s drift-kick-integrator [Rut83], the equations of motion for a given magnetic field needs to be evaluated many times for each period. This makes it more computationally expensive than the GFWIGGLER implementation.

## 4.2.2. Methods to evaluate the simulation results of the different implementations

### Phase space observations

As one indicator of the quality of the implementation, the behaviour of particle distributions in the phase spaces were after tracking through the wiggler in comparison with tracking through a drift space was chosen. The distribution in the phase space directly shows the behaviour of the particles tracked through the optics. One can see if it behaves like a drift space, which is what one expects for the horizontal plane, but not for the vertical, or if the implementation somehow totally misbehaves, like shifting or blowing up the beam, or if it behaves like other implementations.

For investigating the different wiggler implementations particles were tracked through the test optics described in Fig. 4.1 on page 36 and the particle distribution in phase space immediately after the wiggler was observed. The wiggler was exchanged by the different implementations as well as by a drift space of the length of the wiggler. In the vertical plane we expect a slightly different behaviour for either wiggler or a drift space, because of the vertical focussing effect. In the horizontal plane we do not expect such a difference in the first place, but if there were some these might come from higher-order multipole components of the wiggler field. In the discussion, histograms of the difference in the particles' vertical position between the wiggler and the drift space case are compared for different wiggler implementations. The corresponding momentum behaves anti-correlated to this, because in the simulations the phase space is preserved. Therefore only the coordinates, but not the momenta, are shown.

### Field dependent tunes

The particle distributions evaluations were for one field strength only. In contrast to that tunes were taken as a function of the wiggler field as a measure. For this test also the different field data of the **CATACT** wiggler, see 4.1, were used, to compare these data sets, too.

### Comparison with the experiment

Another very strong basis for a decision were first experiments. The decision taken here were based on the **CATACT** wiggler firstly, because the **CLIC** wiggler was not installed at first. Later a benchmark with the **CLIC** wiggler was added, so that the results for the **CLIC** wiggler will be discussed, too.

## 4.2.3. Results of the simulations with the different implementations

### GFWiggler

The first implementation I will discuss is the **GFWIGGLER** using generating functions [BW11]. Though it can use a representation of a real wiggler field by its Fourier components and its wave numbers, see Section 4.1 on page 36, it turns out that this implementation

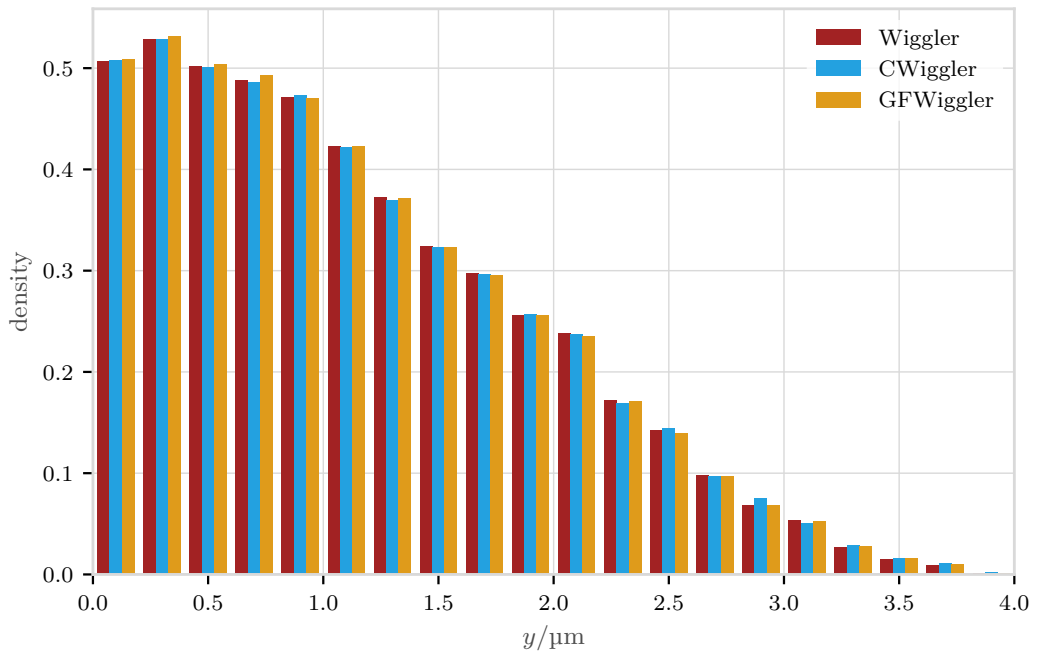


**Figure 4.4.:  $y$ -coordinate change caused by a wiggler compared to a drift (F-0).** Particles tracked through the matched test optics and shown immediately after the wiggler for different wiggler implementations with the field data set F-0. The differences between the  $y$ -coordinates of runs through the respective wiggler implementation and through a drift space ( $y_{\text{implementation}} - y_{\text{drift}}$ ) are plotted into the histogram. Small differences are visible and not just one bin is filled, so all wiggler implementation show behaviours different from a drift space.

does not work in our case and does not provide results different from a naïve sinusoidal implementation.

For the case F-0 all wiggler implementations follow the expectations and show differences from the drift as is shown in Fig. 4.4.

If the field representation does include more than one Fourier component (F-N), such that the advantage of the GFWIGGLER can be used, the tracking code does not behave as expected. As can be seen in the  $y$ -coordinate histograms in Fig. 4.5 on the next page the wiggler does behave like a drift space and not like a wiggler, because there is no difference between its  $y$ -coordinates and the drift space. This shows that the implementation of the GFWIGGLER in *elegant* is too sensitive on small changes of higher field components to be reliably used in simulations.

Additional investigations have been carried out using field data generated using Opera 3d [plc17]. Opera 3d is a finite element method simulation software for three-dimensional electromagnetic models. These investigations can only yield possible causes of the missing focusing effect of the implementation, but no solution to this problem. The case that the quality of the input field data set is not sufficient can be ruled out though. Even using dense field data of an ideal wiggler generated by the finite element method simulation tool Opera 3d the focusing effect is not properly simulated by GFWIGGLER. So the size of the data set and

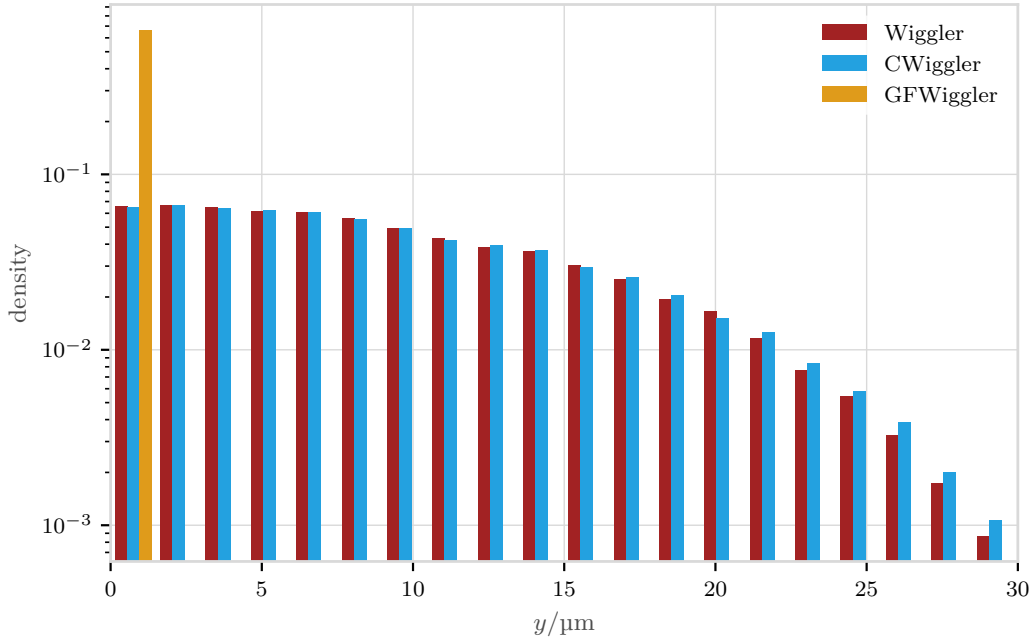


**Figure 4.5.: y-coordinate change caused by a wiggler compared to a drift (F-N).** Particles tracked through the test optics and shown immediately after the wiggler for different wiggler implementations with the field data set F-N. The differences between the  $y$ -coordinates of runs through the respective wiggler implementation and through a drift space ( $y_{\text{implementation}} - y_{\text{drift}}$ ) are plotted into the histogram. The GFWIGGLER does not show any difference from a drift space and thus has only the bin  $y = 0$  filled.

the field data point density is not the cause of this unexpected behaviour. Another possible difficulty might be in the transformation of the field data into Fourier components, but this would also affect the results of the CWIGGLER, which is not the case, as discussed in Section 4.2.3.

To conclude the GFWIGGLER implementation is not suitable for us, because we want to investigate more than the purely sinusoidal field, but also higher-orders; The GFWIGGLER could not provide reliable results in our scenarios.

### CWiggler

A look at the phase space histograms does not indicate misbehaviour of the CWIGGLER implementation. Either using only the harmonic F-0 or many harmonic F-N does result in a slight focusing effect that results in coordinate changes as compared to the drift space in the histograms Figs. 4.4 and 4.5 on the previous page and on this page, so measurements and the tune dependence on the field were used to judge its quality.

### Comparison of the F-N representation with the experiment

*elegant* simulations of the wiggler in the KARA ring with F-N as well as for the F-0 show an expected behaviour for the vertical plane and the simulated field data. For the measured field data that was processed like for the F-N case a slight discrepancy appears compared

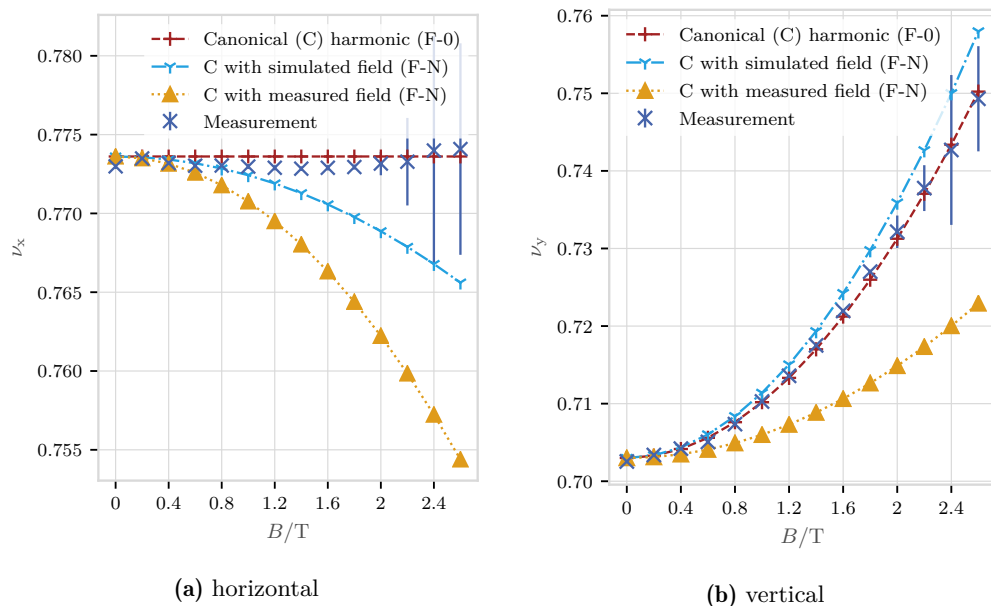


**Figure 4.6.: CATACT wiggler’s field dependent tune shifts.** Measured fractional tune (blue) depending on the CATACT wiggler’s magnetic field for both transverse planes ( $\nu_x$ : left,  $\nu_y$ : right). The error bars for the measured values indicate the standard deviation of the tune read-out. For comparison of the F-0 representation (red, dashed) and the F-N representations of the wiggler for the simulated (light blue, dash-dotted) and measured field (orange, dotted) data are shown. Note the different scales for the horizontal and vertical tunes in the left and right figure, respectively. The F-N simulations vary in the horizontal plane. The measured field does show differences to the measurement in the vertical plane.

to the tune measurements. However, in the horizontal plane the simulations with the CWIGGLER do show a strong disagreement with the measured tunes. Also the simulations with the simulated wiggler field data show this disagreement with the measurement. This suggests that the higher field components that can cause such a behaviour seen in Fig. 4.6 are weighted too strongly by the simulation.

#### Comparison of the F-4 representation with the experiment

For the data processing scheme described in Section 4.1 on page 38 the results, shown in Fig. 4.7 on the next page as “C with Fourier series field”, match the measurements in both planes. The higher components can be represented in the CWIGGLER implementation as well and do not cause severe issues.

#### CLIC damping wiggler field data sets

Only when the CLIC damping wiggler was installed, it was possible to do similar field data sets studies to those with the CATACT wiggler. Since the other implementations besides the CWIGGLER have already shown not to perform well, the discussion of the CLIC damping wiggler representation here focuses on the CWIGGLER only. Here the measurements indeed show some defocusing effects in the horizontal plane which could

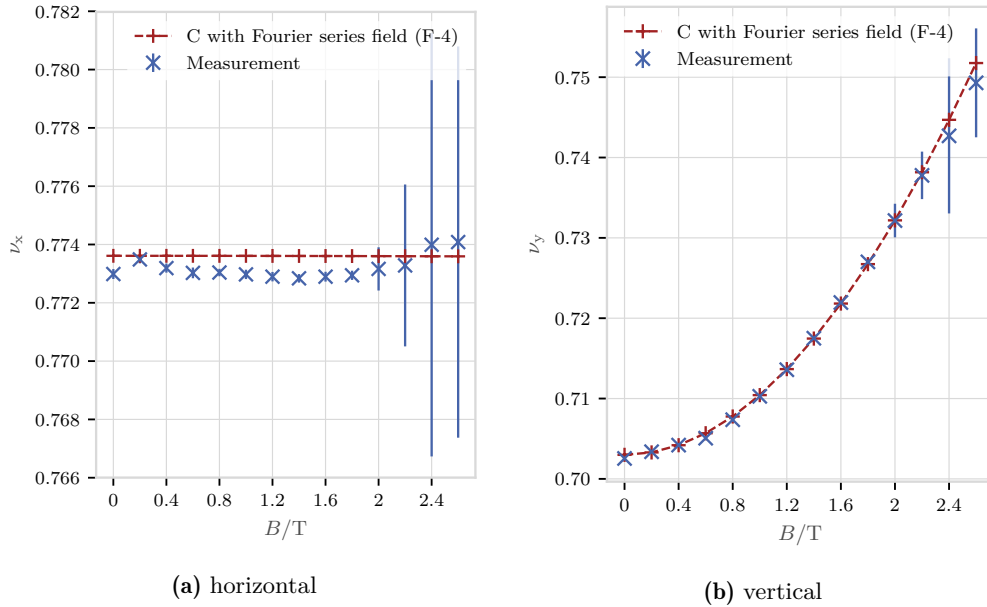


**Figure 4.7.: CATACT wiggler’s field tune dependence.** Like Fig. 4.6 on the previous page, but with the simulation results for the F-4 data set. It does not show a difference to the measurements. This case fits the measurement best.

be described best by the F-N data set, noted as “C with simulated field” in Fig. 4.8 on the facing page. So in contrast to the CATACT the F-N data set is preferred over the F-4 one. Tune simulations for the CWIGGLER show differences in the less important horizontal plane between different field data sets. The F-N data set is more accurate in the case of the CLIC damping wiggler with relatively strong non-linear behaviour, but too unstable in the case of CATACT where one should stick to the F-4 set which is more stable. That also means that it’s not sufficient to judge the wiggler’s implementation based on simulations, but a comparison with measured data is crucial for the selection of the implementation for each wiggler.

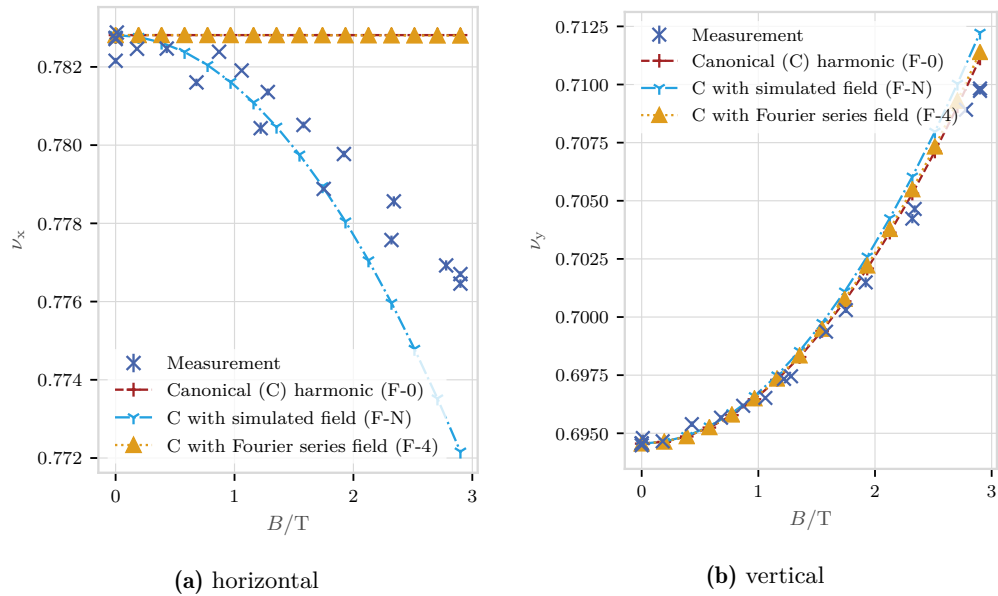


**Figure 4.8.: CLIC wiggler's field tune dependence.** Measured fractional tune depending on the CLIC damping wiggler's magnetic field for both transverse planes ( $\nu_x$ : left,  $\nu_y$ : right). The error bars for the measured values indicate the standard deviation of the tune read-out. Comparing the different wiggler implementations: the *canonical (C)* CWIGGLER and the *Generating functions (GF)* GFWIGGLER one for different field data sets: the one *harmonic* F-0, the *simulated* F-N and the *Fourier series field* F-4. The *simulated* F-N is the only model that predicts a horizontal tune shift, though it cannot describe the measured tune shift precisely.

**Table 4.2.: Comparison of the wiggler implementations.** The different tracking algorithms for wigglers (CWIGGLER, GFWIGGLER, “wiggler”) and different magnetic field representations (“Field”) are listed in this table.

Field	CWIGGLER	GFWIGGLER	wiggler
F-0	linear theory well described for <b>CATACT</b> , non-linear theory for <b>CLIC</b> not so well	behaves like the wiggler implementation	not ok for <b>CLIC</b> in horizontal plane
F-N	simulations and measurement mismatch for <b>CATACT</b> in vertical plane → extremely sensitive to many Fourier components $\nu_x$ <b>CATACT</b> linear theory not matched well $\nu_x$ <b>CLIC</b> damping wiggler non-linear theory ok.	$\nu_y$ does not fit for <b>CLIC</b> damping wiggler	-
F-4	<b>CATACT</b> behaves as expected. non-linear effects of <b>CLIC</b> damping wiggler in the horizontal plane not represented	$\nu_y$ dose not fit for <b>CATACT</b>	-

### **Conclusion**

In this chapter three different algorithms for tracking through wigglers that are implemented in *elegant* were presented. As can be seen in the comparing Table 4.2 on the preceding page the CWIGGLER implementation with the F-N is the most accurate, and reliable way to track through the **CLIC** wiggler. For the **CATACT** the F-4 is the best magnetic field representation. Therefore these configurations are used in the following.



## 5. Developing and refining models of the storage ring **KARA**

In the last chapter we looked into the different aspects concerning the simulation of wigglers. This chapter will deal with the electron storage ring **KARA** that is located at KIT Campus North. In this chapter the beam dynamics simulation models are presented for the two operational modes that are relevant for this work.

At first, the more robust and better understood “normal operation mode” at 2.5 GeV is considered. It can serve for evaluating the beam dynamics simulation model and find its limitations and sensitivity. Later on the more challenging 1.3 GeV short-bunch operation mode will be discussed.

It will be discussed that it is not possible to build up one model that is completely based on first principles and that could scale with the beam energies. Instead two models of the lattice that include the wiggler and that can be used for the two interesting operational modes were developed and are presented in the following. These models are based on **LOCO** and tune measurements and by this can be kept up-to-date. How this is done will be explained, too. In the end one wants to separate the effects of the wiggler from those of the optics changes.

### 5.1. Normal operation mode

This operation mode is used for benchmarking and characterisation experiments of the wiggler and optics with the wiggler for all cases that do not rely on the 1.30 GeV optics.

#### Understanding the storage ring **KARA**

In this section the subtleties of the accelerator are introduced to the reader and issues that arise with a first principle approach are discussed. For the storage ring the magnet currents are not measured independently, but by the power supplies themselves. There exists a difference between the set values of the power supplies and the readback values. This difference is in the range of 10 mA. Beam dynamics simulations with magnetic strength differing by the corresponding magnetic strength values result in tune changes in the second decimal place. This difference is two orders of magnitude larger than the typical error on the tune measurements at **KARA**.

### First principle approach

The existing *elegant* model of the 2.5 GeV optics [Get14] was updated to use the latest measured beam energies [Cha16]. The difference of  $6.94 \times 10^{-9}$  and  $-6.08 \times 10^{-9}$  for the horizontal and vertical tunes caused by the energy change from 2.5 GeV to 2.47 GeV is negligible. Also the chromaticity changes by  $8.00 \times 10^{-3}$  and  $1.95 \times 10^{-2}$  are smaller than the typical measurement resolution.

The model is primarily based on first principles and fitted functions of the magnetic strength depending on the current of the magnets. It is not based on fits of the magnetic strength to, for example, measured tunes or other optics characterising measures. It used to have fringe fields of bending magnets which depend on the energy and are not represented in the machine model used for e. g. **LOCO**—see below. The advantage of that is that one can correlate the effects caused by a deviation of the lattice more easily with the model. Neglecting hysteresis effects of the magnets one could also scale one model to a different one with different beam energy. Unfortunately, the magnets go into saturation [EKP99] and the generalized functions of the magnetic strength do not include this effect properly. Hence one needs to have two different models for the two energies 2.5 GeV and 1.3 GeV.

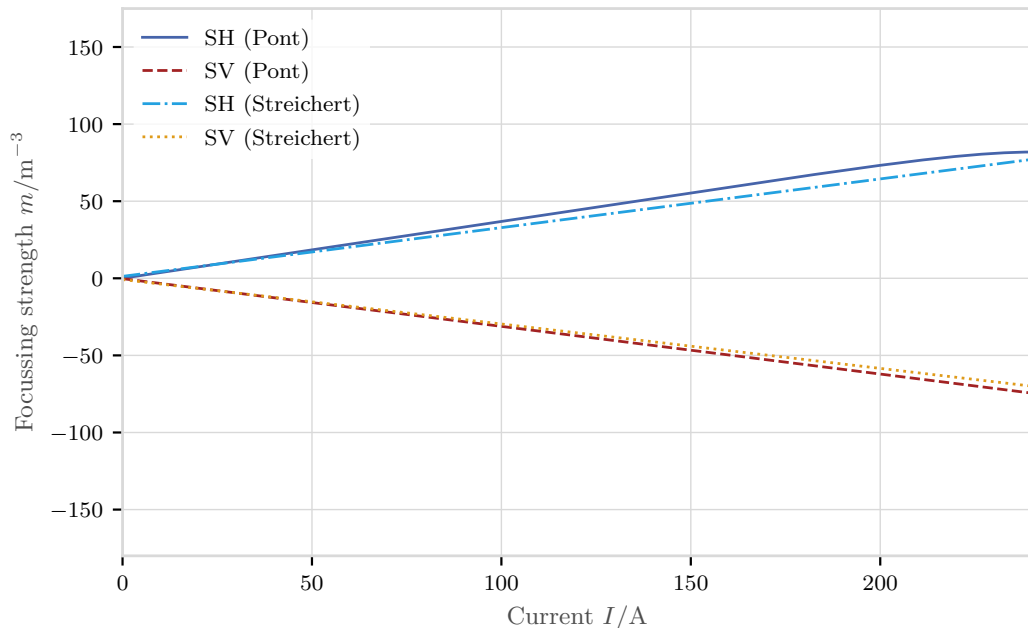
There are three different numerical rules in use for the transformation from currents of the quadrupole and sextupole magnets to magnet strengths. One is based on the magnet prototypes [EKP98], referred to as “Pont’s model” and one is based on the first measurements of the magnets installed in the ring [EKP99]. The third one is based on the second, but improved with changed sextupole strengths [Str12] (referred to as “Streichert’s model”). Therefore only the first and last one are compared here. The transformations for the sextupoles show large differences and will be discussed in the following. The differences of the transformations for the quadrupoles are in the range of  $\pm 2\%$  in the typical operation range and are discussed in Section 5.1.0.1 on the facing page.

Fig. 5.1 on the next page depicts two fits of the sextupoles strength in the whole working range of the sextupole magnets. As can be seen more clearly in the differences of the sextupole strengths fits plotted in Fig. 5.2 on page 54 occur mainly at the very low end. This is, because there both limit 0 as does the division. Above 10 A the differences are below 20%.

Also the transformation rules for the quadrupoles result in differences to measurements. Table 5.1 on page 55 shows the tunes for the two transformation rules, a **LOCO** fit—which will be discussed in a moment—, and a measurement. The root of the squared differences between the measurement and Streichert’s transformation formulas (0.31) is smaller (better) than that one between the measurement and Pont’s transformation rules (0.46). Both are worse than that of the **LOCO** fit.

This approach of first principles does provide a model of the ring which is not good enough to reproduce the tunes and to be a model for realistic simulations to a percentage level.

Though these transformations from field strength to current do not suffice for the complete



**Figure 5.1.: Fit functions of the sextupole strength by [EKP99] and [Str12].** Two different fits of the sextupole strengths  $m$  in both planes (SH: horizontal sextupole, SV: vertical sextupole). One ([EKP99]) is based on the initial measured field (blue, solid; red dashed) and the other (light blue, dash-dotted; orange, dotted) is based on measurements done with the beam ([Str12]). The complete working range is depicted. Both different approaches of translating the current of the sextupoles to a corresponding sextupole focussing strength differ.

model, it's still useful for calculating the set currents for simulated magnet strength and as estimates in cases where optics measurements aren't feasible.

#### 5.1.0.1. LOCO fits of the model for 2.5 GeV and 1.3 GeV

The next approach to improve the model is fitting the model to the ring using the **LOCO** ([Saf97]) technique, already mentioned in Section 3.3.5 on page 32. Therefore the **ORM** was measured as well as the tunes. Comparing simulated tunes for the three models with magnetic strength taken from the **LOCO** fit, and the two current to magnetic strength transformations with the corresponding measurement, provides us with the results shown in Table 5.1 on page 55. One can see, that the **LOCO** fit results in smaller differences to the measurements in comparison to the just discussed transformation rules. So the **LOCO** fit is the best of the compared methods to get quadrupole strength values for our beam dynamics model. However, Table 5.1 on page 55 also shows that the **LOCO**-fit is not fully sufficient to provide proper simulations. Unfortunately fits of the **LOCO** fitting routine themselves do not converge very well at accelerators with a small circumference and relatively few kickers and **BPMs** either, see [Saf97]. For example, the fit done for Table 5.1 on page 55 had a normalized  $\chi^2$  of  $\frac{\chi^2}{DOF} = 31514$ . This means that one has to improve the model further.

Anyhow, it is possible to extrapolate the quadrupole strength change of one optics to

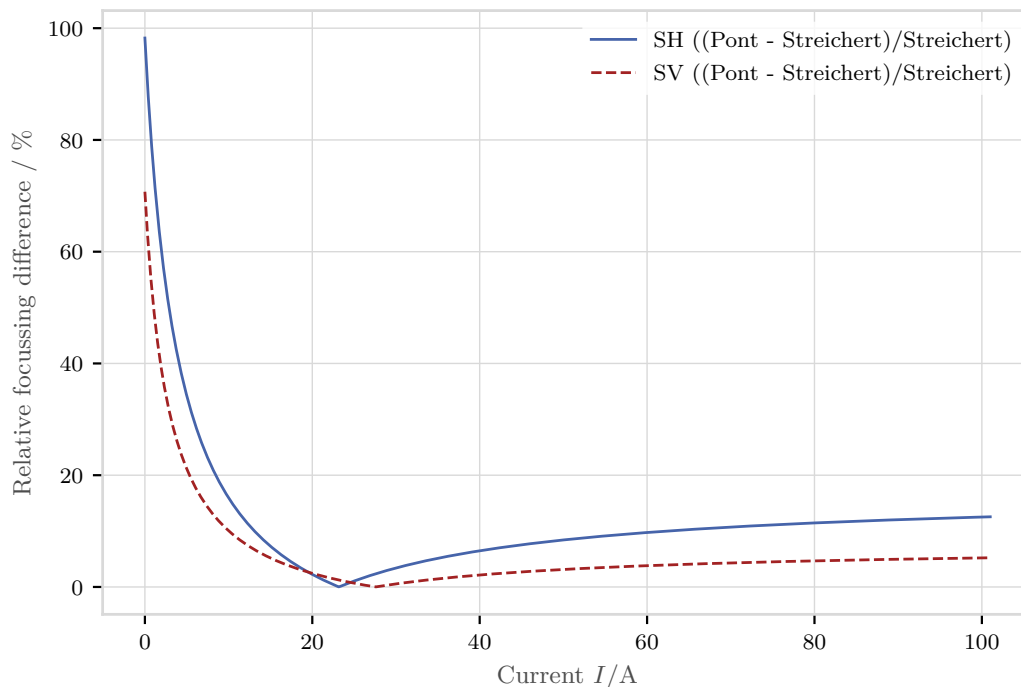


**Figure 5.2.: Differences between two fits of the relationship of sextupole strength and current.** The differences between the originally measured relationship [EKP99] of sextupole strength and sextupole current minus a fit done by [Str12] and then divided by the fit show differences in the typical range of operation (up to 100 A). For low sextupole currents the differences between the two conversion functions disagree much. However, both limit 0, so the deviation by a small value likely causes this effect. For higher sextupole currents the differences stays below 15%. These differences occur for both sextupole families—the horizontal (blue, solid, SH) and the vertical (red, dashed, SV).

another one. So taking two optics and one **LOCO** fit for one of these settings, one can calculate the quadrupole strength for the second one applying Streichert’s transformation rule, to get to the results of a second **LOCO** fit for the second optics.

Thus the **LOCO** fits are taken as a starting point for fits of the quadrupole and sextupole strengths to the actually measured tunes and chromaticities. The allowed variation of the strengths in these fits is within the variation of the difference of the readback and the set values of the currents translated into magnet strength.

This procedure of getting an optics model was done multiple times for different optics. Because of the octuple components introduced by the superconducting wigglers, as described in Chapter 6 on page 59, the normal operation mode optics were changed during this work, see [PBG<sup>+</sup>17, PBB<sup>+</sup>19].

The optics and therefore the tune change is shown in Fig. 5.3 on the next page. In the plot the old tune (lower, left point) is near different resonance lines, especially to the third order which corresponds to octupoles. Therefore, a lifetime decrease was the result. Parts of the beam, which has a finite size, hit the resonance when the wiggler was turned on and this resonance gets more relevant. The new tune is closer to a second order resonance line,

**Table 5.1.: Comparison of tunes by modelling.** Tunes simulated with magnetic strength calculated with M. Streichert’s and with M. Pont’s formula for the magnet current (readback) values. The **LOCO** fit was made for the orbit response matrix measurement for fill 6009.

	Horizontal	Vertical
Streichert	6.99686	2.9128
Pont	6.85182	3.1410
LOCO	6.82683	2.5519
Measurement	6.78113(20)	2.6896(2)

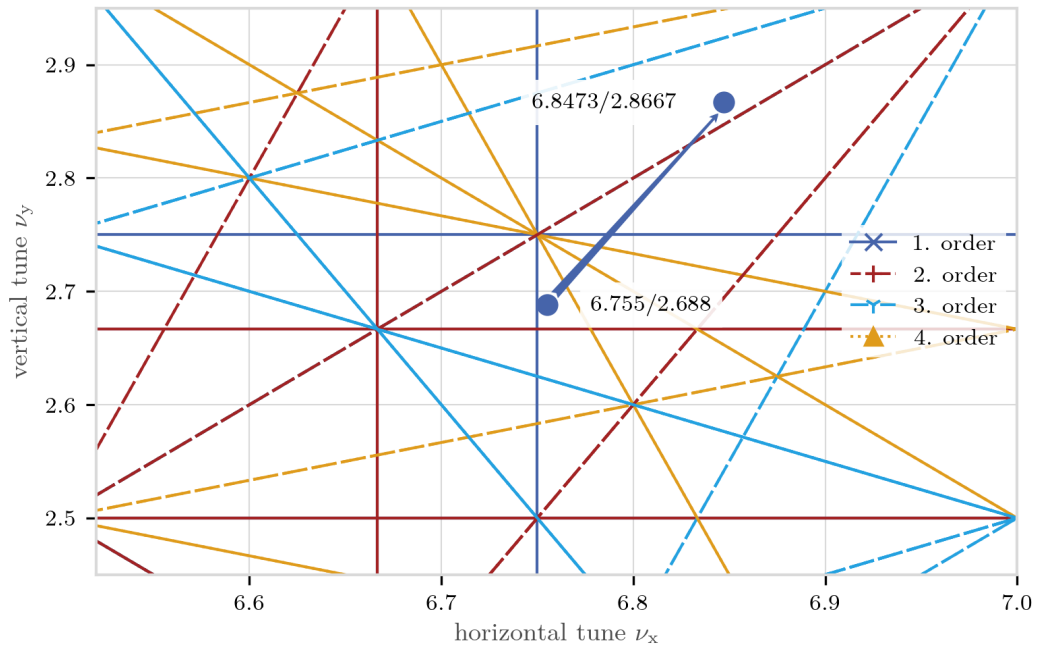


**Figure 5.3.: Tune change caused by the optics change.** Comparison of the tune in 2016 and the tune from 2017 on. In the relevant section of the tune diagram one can see the resonance lines of the important first four orders and the old and new tunes. The arrow points from the old (2016) tune to the new (2017) tune.

but far enough to be not affected by it and it is far away from the third order. During the development of the new optics by A. Papash, cross-checks with *elegant* models were done, as part of this work, showing the strong effect of additional octupole components on the old optics on the dynamic aperture and thus lifetime.

After the new optics were implemented as the new normal operation mode, they could be modelled the same way as the old one was before, showing the approach to use the **LOCO** fit and fitting to measured tune values is a feasible approach.

### 5.1.0.2. Conclusion

The first principle approach to get a model for the optics does not satisfy the need of a model being able to predict the tune up to the third decimal place. This might come from

e. g. displacements of the magnets. One needs to use fitting routines like **LOCO** and tune matching to get to proper models. However, it is possible to extrapolate from a given fitted model to a situation where the optics are changed, e. g. by a wiggler, with the first principle approach.

## 5.2. Short-bunch mode

As it was done for the simulation of the 2.5 GeV operation mode, the quadrupole strengths for the optics of the 1.3 GeV long bunch mode and the 1.3 GeV short-bunch mode were determined. Therefore also the **ORM** measurements and dispersion measurements were done to get **LOCO**-fits as a first approximation to the lattice. In this case with smaller energy the beam is not as stiff as with 2.5 GeV, therefore the kicks applied in the measurements cause much greater effects and the risk of losing the beam during the measurements increases. Furthermore, the beta functions are larger by a factor of up to 4.4, as well as the emittance by a factor of 1.41 with these different optics. Hence the transversal beam size is larger which also increases the chance of beam losses.

Since the low-energy optics with a longer bunch is more stable than the ones with short bunches, the long bunch optics is used for general investigations of energy-dependent effects with the wiggler. The latter is used to investigate effects on the THz-spectrum. This means that both optics need to be investigated. Shrinking the longitudinal beam size is done by minimising the distributed dispersion—in case of **KARA** by lowering the strength of the third quadrupole family (Q3 in Fig. 3.4 on page 30). When the wiggler's field is ramped one may need to adjust the optics, because the tune change caused by the wiggler is potentially so large that resonances are crossed. This will be discussed in the sections about alignment (6.2) and the short-bunch operation (7.1). This means that the optics which is taken from the **LOCO** fit and tune matching needs to be adjusted using the transformation rule from the currents to the strength and vice versa.

For different optics (fill 6450 and fill 6487) at 1.3 GeV **LOCO** fits have been created. Both fits are relatively good with  $\frac{\chi^2}{DOF} = 846$  and  $\frac{\chi^2}{DOF} = 1695$ . The normed subtraction of the current differences of the **LOCO** fitted models ( $\Delta I_{\text{LOCO}} = I_{\text{LOCO}(f6487)} - I_{\text{LOCO}(f6450)}$ ) and the actual quadrupole currents ( $I_{f6487} - I_{f6450}$ ) is  $\Delta I_{\text{extrapolation}}/\Delta I_{\text{LOCO}} - 1 = 40\%$  or 3.50 A.

These differences of currents cause a difference of the  $\beta$ -function of  $\langle(\beta_{f6487} - \beta_{f6450})/\beta_{\text{extrapolated}} - \beta_{f6450}\rangle \approx 20\%$  in the horizontal and 30% in the vertical plane. This results in fractional tune differences in the second decimal place, as can be seen in Table 5.2 on the next page.

Because of this the tune also needs to be measured and finally the model needs to be matched to the tunes. For the matching the limits of the fitting range were set to the limits provided by the difference of the set and readback values of the currents.

**Table 5.2.: Tunes for different lattices.** Different fractional tunes for a LOCO fitted model, the extrapolated and a measured tune for fill 6487.

	Horizontal	Vertical
LOCO	0.7433	0.7725
Extrapolated	0.7897	0.7928
Measurements	0.7283	0.7499

### Conclusion

It is not possible to build up a model that is completely based on first principles. Nevertheless, the goal to have an up-to-date model that is based on measurements can be achieved. Using a **LOCO** fit and then matching the tunes, one can generate a model that can predict tune changes to an uncertainty of 20%. The effects of the wiggler are expected to be stronger, so that they can be separated from those of the optics changes.



## 6. Experimental characterisation of the wiggler in the storage ring

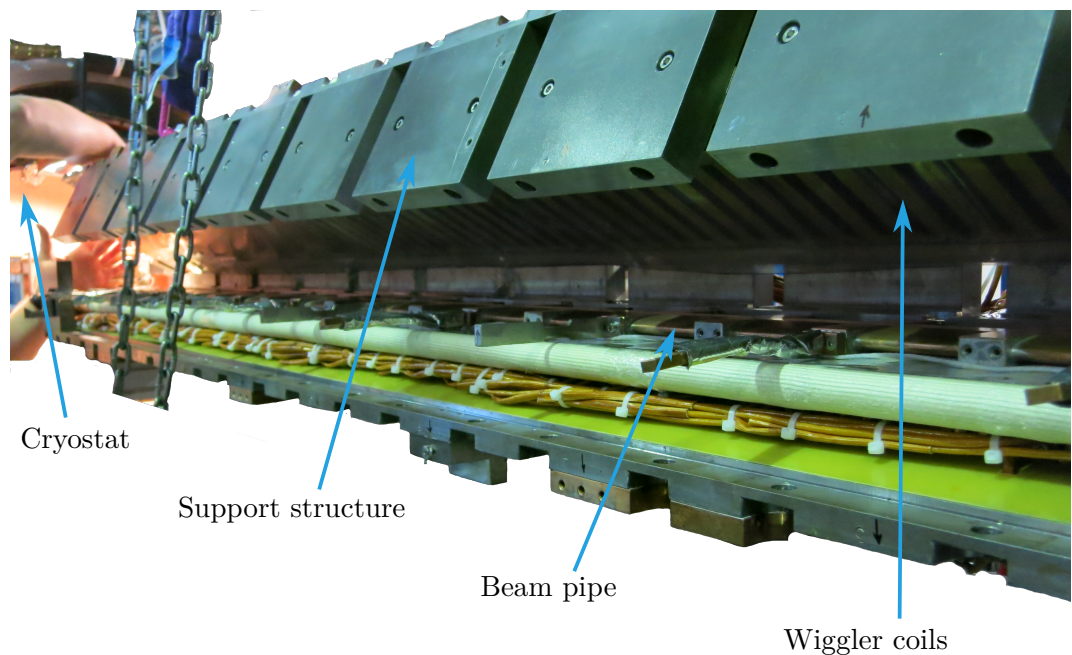


**Figure 6.1.: Wiggler during site acceptance test** Before the site acceptance test the wiggler was outside its cryostat. On the left side in the background the cryostat is visible. In the foreground the top coils of the wiggler are visible, because the wiggler's top and upper support structure are opened. The wiggler's bottom coils are below the beam pipe and not visible when the beam pipe is installed. Courtesy: Steffen Hillenbrand (not CC-BY)

In this chapter it will be investigated how the wiggler is aligned, if it has the expected optical properties and if it has an unexpected impact on the beam dynamics that have not been taken into account in simulations so far. These investigations start with the basic effects tune change and alignment error effects.

But at first an important investigation that is not related to beam dynamics is presented in order to fully focus on the beam dynamics afterwards.

## 6.1. Heat load measurements

One goal of the collaboration between CERN and KIT was to test if the cooling concept is good enough for the demands of the CLIC project. The wiggler is the first ever built conduction-cooled and not bath-cooled wiggler. Because in the CLIC damping rings it is foreseen to operate about 100 m of wigglers in a row, the capabilities of the wiggler to deal with high heat-loads needed to be verified. The synchrotron radiation spectrum of the wigglers in the CLIC damping rings is similar to that of KARA at 2.50 GeV, so we could investigate this at KARA. As described in more detail in [BBC<sup>+</sup>16], we tracked the temperatures during normal “user operation” and wiggler fields of 2.90 T to see if there are long term effects. Furthermore, we tracked the temperatures while heating the beam pipe with an additional 50 W to simulate heat input from synchrotron radiation of upstream wigglers in the damping rings.

The longer-term investigations, in the time range of several weeks, yielded constant temperatures of 3 K during operation and temperatures of up to 3.60 K during ramping of the wiggler’s field. Long term observations in the time range of 15 minutes show a slight increase of temperature on the downstream side of the wiggler which is caused by some unknown defects, and started after a quench during normal operation.

The test with additional heating power showed that the field ramping speed needs to be decreased slightly, in that case, to avoid reaching critical temperatures. Nonetheless, operation at 2.90 T, 2.50 GeV and this simulated heat-impact is no problem. So we could conclude that operation up to 2.90 T with this wiggler should be feasible for the CLIC damping rings, too.

## 6.2. Tune measurements

One main feature of a damping wiggler is its vertically focusing behaviour. This can be seen as a tune change depending quadratically on the wiggler field as was shown in Eq. (2.22) on page 19:

$$\Delta\nu_y = \frac{\beta_y}{4\pi} L \left( \frac{e}{\gamma m_0 c} \right)^2 \langle B^2 \rangle \quad (6.1)$$

Fig. 6.2 on the next page shows the measured tune shift caused by the CLIC damping wiggler in 2.5 GeV operation. The vertical tune shift—red crosses—, clearly shows the expected quadratic change and nicely matches to the analytically predicted curve—red dash-dotted line. For the analytical prediction the vertical beta-function at the position of the wiggler,  $\beta_y = 1.99$  m, was simulated for the optics without the wiggler.

Because crossing a tune resonance has to be avoided and tune changes with wiggler field are smaller for higher beam energies and because the beam is generally more stable at 2.5 GeV, this measurement is easier to do in this operation mode.

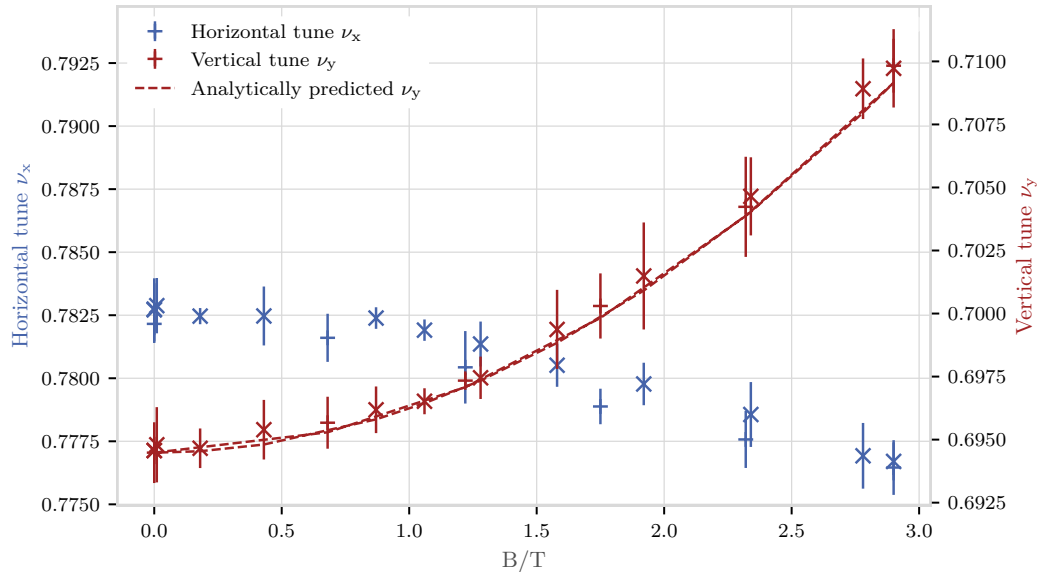


**Figure 6.2.: Wiggler field dependent tune shift at 2.5 GeV.** The analytical prediction of the vertical tune  $\nu_y$  (red line, right axis) is done for the wiggler field strength  $B$  at which the measurements took place. It shows the quadratic dependence on the wiggler field. For the analytical prediction  $\beta_y = 1.99$  m was taken from *elegant* simulations. The error bars of the measured horizontal tunes  $\nu_x$  (blue, left axis) and vertical tunes  $\nu_y$  (red, right axis) indicate 10 times the standard deviation of the tune measurement, because they wouldn't be visible otherwise. The vertical tune increases with the wiggler field as the analytical prediction does. The horizontal one decreases slightly though no change at all is expected from linear theory. The curve for the horizontal tune shift shows a difference between ramping the wiggler up (+ marker) and ramping it down (x marker) again. A similar plot was also published at [BBC<sup>+</sup>16]. Fill 5837.

However, because we are interested in the 1.3 GeV optics, too, measurements at 1.3 GeV were also done. They also show the expected behaviour in the vertical plane, though it is necessary to adjust the optics while one increases the wiggler's field, because otherwise the beam is lost due to resonance crossing. Therefore the shift consists of several smaller shifts that show the quadratic behaviour, separated by tune shifts of the opposite sign caused by the optics change at each measurement point. This is depicted in Fig. 6.3. The analytical prediction is evaluated at the markers only.

As can be seen in both cases, 2.50 GeV and 1.30 GeV, there is also a tune shift in the horizontal plane, but with opposite sign. This defocussing effect is not expected in the linear theory when  $k_x = 0$  and the field in  $x$  is homogeneous [Smi86]. The so-called roll-off-effect [SLT<sup>+</sup>02] that caused such behaviour at other accelerators can be excluded as the cause of this behaviour in our case, because the wiggler's poles are 15 cm wide [MVS<sup>+</sup>16] and the measurements were carried out at the reference trajectory  $\pm 3$  mm. This is inside of the so-called “good field region” where the field integrals are less than  $10^{-4}$  Tm as measured by BINP [MVS<sup>+</sup>16]. The roll-off-effect—occurring at the horizontal edges—would let the wiggler act like an additional quadrupole. In that case the vertical and horizontal tune change would sum up to the expected vertical tune change, or in other words, the vertical

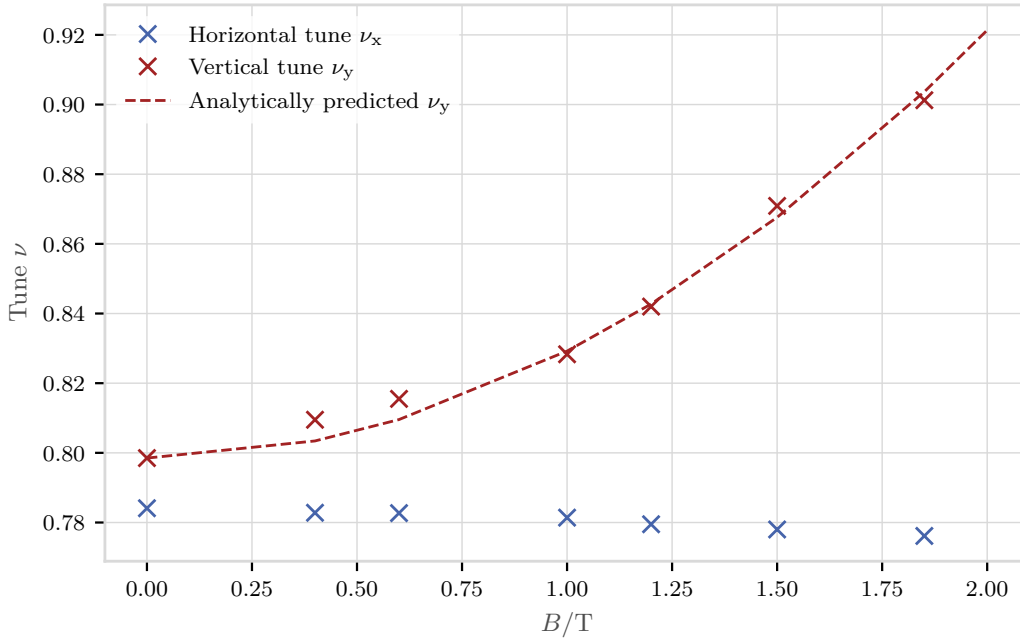


**Figure 6.3.: Wiggler field dependent tune shift at 1.3 GeV.** The vertical tune  $\nu_y$  (red) increases with the wiggler field whereas the horizontal one  $\nu_x$  (blue) decreases slightly. The tune increase is measured in steps. Between each step the tune shift was compensated by adjusting the quadrupole strength. Afterwards, the tune changes are summed up so the tune corrections by the quadrupoles is not visible any more. The beta function used for the analytical prediction (dashed line) is simulated using *elegant*. Fill 6477.

tune change would be diminished by the absolute value of the horizontal one. Since this is not the case, we can exclude the roll-off-effect as the cause of the horizontal tune shift. Unfortunately, the tracking simulation of the wigglers do not show these effects either, and only the wiggler simulation with the CWIGGLER and F-N, elaborated in 4.2.3, shows the same tendency, albeit not in the measured intensity.

If one takes a look at higher-order field expansions of the wiggler’s field, like done e. g. by Smith in [Smi86], a horizontal tune change emerges. These higher-order components cause, amongst others, **amplitude-dependent tune shift, also-called detuning with amplitude (ADTS)**—as will be elaborated in Section 6.4.2 on page 71.

These effects of horizontal focusing, as well as ADTS, have also been observed at Bessy [KB90] and SPEAR [SLT<sup>+</sup>02].

Another unexpected behaviour that can be seen best in Fig. 6.2 on the previous page are small hysteresis effects that result in a different slope of the horizontal tune for ramping the field up and down. The wiggler’s field was ramped up and down and the tune change is slightly different for the same currents, here labelled as wiggler’s field ( $B/T$ ). These different tunes for the increased and decreased field might have different origins. First of all, there might be hysteresis effects in the iron poles of the wiggler. Especially inside the matching coils where the magnetic field is not as strong as in the main coils this hysteresis might be stronger than in the main coils. That might cause the differences in

the tune changes between the vertical plane, where the tune change with wiggler field is dominated by the main coils, and the horizontal plane, where the tune change originates from imperfections foremost from the fringe fields. Another origin might be the normal conducting dipole corrector coils at the end of the wiggler that correct for unsatisfying first field integrals in the horizontal plane. These corrector coils are not well characterised, so that one cannot exclude them causing this hysteresis-like effect.

However, this is not critical for standard operation scenarios since the wiggler is operated at one wiggler field most of the time or only ramped up, but not ramped down to a smaller magnetic field.

To conclude the wiggler's field dependent tune measurement gave hints on higher-order components of the wiggler field, due to the behaviour onto the horizontal plane, as well as hysteresis effects, but could confirm the expected vertical tune shift.

### **Alignment measurements in analogy to field integral measurements**

A measurement of the dependence of the tune on the beam axis inside the wiggler can be used to test for alignment errors. Alignment errors can cause multipole components which cancel out in the central axis integrating over the complete wiggler, but do not cancel out off-axis. Multipole component errors also occur for different reasons than alignment errors and are already tried to eliminate in the production phase of an **ID**. Outside the ring multipole components and the second field integral can be investigated by applying a current to a stretched wire and measuring a shift of this wire. This measurement technique mimics the electron beam as the wire. In the accelerator ring a tune shift occurs instead of the shift of the wire. Both methods will be described in the following.

Simulations of a simple Halbach type wiggler field [Hal81] using Opera 3d [plc17] show a clear quadratic dependence of the second field integral, see Section 2.1.6.1 on page 18, on the vertical position. As shown in Fig. 6.4 on the next page the field should not depend on the horizontal position though, as long as we are away from the edges of the magnet.

The field integrals of the **CLIC** damping wiggler have been measured by **BINP** with the stretched wire technique [WBC<sup>+</sup>95, ZW96, Sch92] on-axis where they should be zero, and with an accuracy of  $2 \times 10^{-5} \text{ Tm}$  and  $5 \times 10^{-5} \text{ Tm}^2$  for the first and second field integrals respectively. The stretched wire method is a magnetic (multipole component) measurement technique where a wire is stretched through the magnetic gap and returned outside of the magnetic structure. When a current is applied to the inner wire, it moves, because of the Lorentz force. The movement of the wire is measured. The first field integrals can be determined from the horizontal shift of the wire (or vertical for the horizontal field integral respectively) where both ends create a force in one direction. The second field integral reflects in an anti-parallel force of the ends. The exact equation can be found in B.5.

After installation the alignment of the wiggler was measured by shifting the electron beam as described in Section 3.3.3 on page 29 and measuring the tune. The orbit was

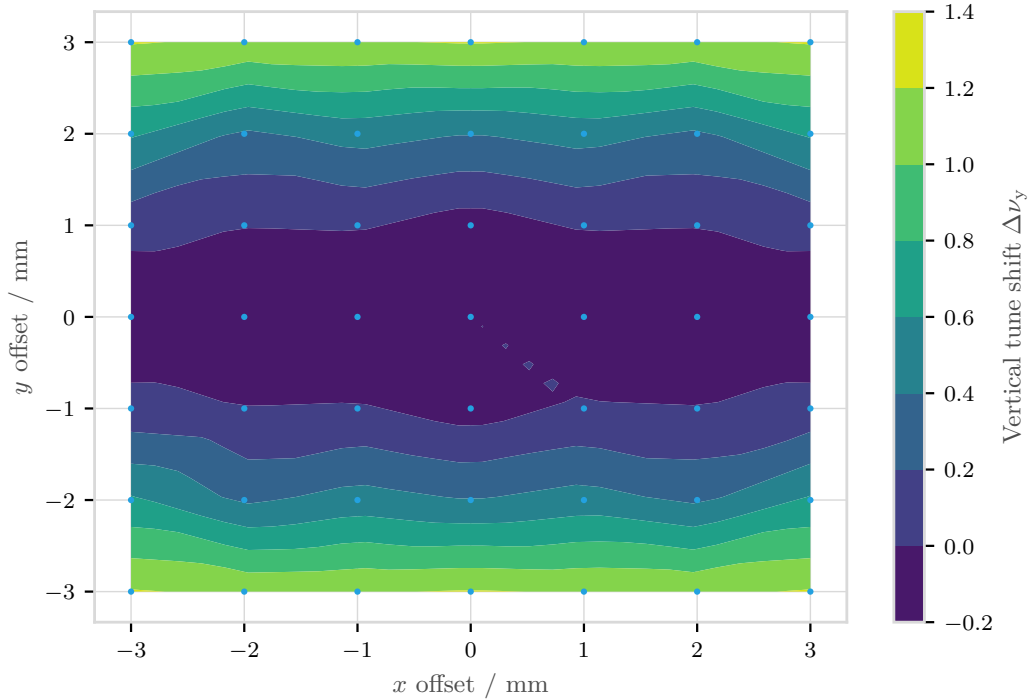


**Figure 6.4.: Second field integral dependence on the horizontal and vertical offset.** The plot shows a Opera 3d simulation of the second field integrals of an ideal wiggler calculated for the light blue points and linearly interpolated for illustration. The vertical gap is 18 mm high. The second field integrals increase quadratically with the vertical offset from the mid plane, but do not increase with the horizontal plane.

shifted in both planes to get a raster like before in the Opera 3d simulations. As can be seen in Fig. 6.5 on the next page the measurement (measured at the grey dots and then linearly interpolated) ranges not as far as for the simulations, but could be only proceeded up to 1.50 mm in the horizontal plane and 2 mm in the vertical. Nevertheless, the quadratic change of the tune shows a minimum in the vertical plane at 0 mm which shows the correct vertical alignment and only a slight variation in the horizontal plane.

The 3d orbit bump measurement shows that the vertical tune for a shift along the vertical plane behaves, within the uncertainty of the tune measurements in the range of  $\pm 10^{-4}$ , as expected by the theory and the raster scan simulations, so it shows the symmetrical, quadratic behaviour. The uncertainty on the alignment of this measurement is smaller than the technical alignment precision, so one can say the wiggler is vertically aligned correctly. The tune shifts along the horizontal plane, on the other hand, shows small differences to the simulations and expectations, that gives hints on higher-order effects which need more investigations, which will be described in more details in Section 6.4.1 on page 67.

### 6.3. Search for sextupole and other not expected multipole components

Besides the multipole components measurable with stretched wires, there might also be so-called dynamic multipole components. These multipole components are called “dynamic”,

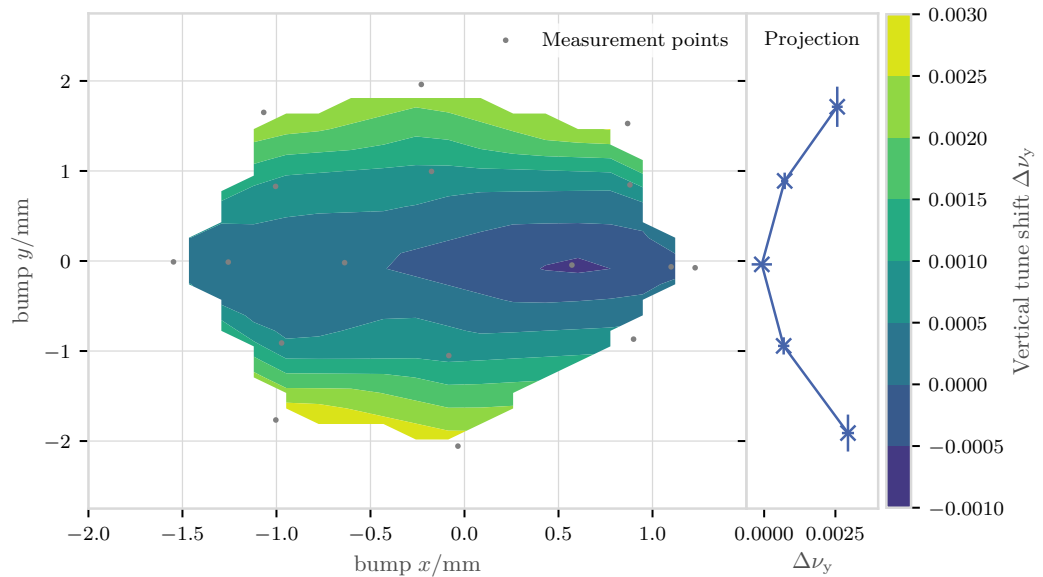


**Figure 6.5.: Vertical tune for orbit raster scan.** Measurement of the vertical tune depending on the position of the beam going through the wiggler. The beam position change is caused by local orbit bumps, as explained in Section 3.3.3 on page 29. The plot also shows a linear interpolation of the grey measurement points. On the right hand side there is a projection of the measured points along the  $y$ -axis. There the line is for visualisation purposes solely. The standard deviation of the projected vertical position and of the vertical tune shift are shown as error bars in the projection plot. A quadratic behaviour is expected.

because they affect the movement of the electrons, but are not accessible to measurements utilising stretched wires. The quadrupole-like behaviour of the wiggler in the  $y$ -plane causes the aforementioned vertical focussing and tune change. We proceed with the next higher-order multipole component after the quadrupole which is a sextupole like component.

There should be no even multipoles (sextupoles, decapoles, etc.) since the wiggler is symmetric in  $x$ , cf. [SLT<sup>+</sup>02]. This is, because if  $B_y(x)$  depends on  $x$  then the Lorentz force acts on the electrons entering each pole at a different position differently. Doing the integration over their path yields:  $\int B_y ds \approx -\frac{1}{2} L x_p(x_i) \frac{dB_y(x_i)}{dx}$  [SLT<sup>+</sup>02]. It has got an odd function, but no even functional part. Therefore even multipoles are not expected.

Also there are no indications by the tune vs. shifted orbit measurements that there are sextupole or skew-octupole components. As described in [KB90] these would appear as a linear dependence of the vertical tune shift on a horizontal orbit displacement and as an additional tune shift depending on displacements in  $y$ , which is not the case as plotted in Fig. B.2 on page 104 and Fig. B.1 on page 103.

Nevertheless, the chromaticity—the measure of sextupoles—is changed indirectly by the different focussing, because the changed focusing results in a different phase advance between the sextupoles of the magnetic lattice of the storage ring [Wal93]. As for the tune, there is no horizontal chromaticity change expected in the linear theory.

To get to know the chromaticity change caused by the phase advance changes, I also measured the chromaticities depending on the wiggler's field, as described in Section 3.3.2 on page 27. The measurements were performed for different wiggler strengths and for different optics.

Since we are interested in the relative change of the chromaticity caused by the wiggler, for this purpose it is best to operate at chromaticities between 0 and 1.

Also operation above 0 is preferred, because head-tail instabilities are suppressed then [MZ03]. However, small but positive chromaticity values are better than high chromaticities, because small absolute effects show up as bigger relative effects and are thus better to detect. In addition the tune readback improves at smaller absolute chromaticities, because the tune is not depending on the momentum, which results in a smaller tune spread, so the signal width of the tune decreases and the peak can be found more precisely.

From the values listed in Table 6.1 on page 68 and shown in Fig. 6.6 on the next page one can say that a horizontal chromaticity shift is clearly visible, but no vertical one. The horizontal chromaticity shifts by 0.18 for the field change from 0 T to 2.80 T. The uncertainties of the horizontal chromaticities, caused by the tune measurement, are up to a factor of 2 smaller than those of the vertical ones, too.

Further measurements with vertical chromaticities less than 1 also do not show a trend.

Chromaticity measurements done in collaboration with Panagiotis Zisopoulos from CERN, using a different approach for the data acquisition and analysis, developed by Panagiotis Zisopoulos [ZPL19, ZPA<sup>+</sup>15], show similar behaviour [Zis18].

In theory the effects are even stronger for lower beam energies. However, a measurement at lower energies is more difficult and the risk of beam losses increases. At 1.60 GeV and 1.3 GeV measurements with no field and 1 T were done, but the uncertainties are too large to see any significant effects.

### Conclusion with respect to the chromaticity

There seems to be no effect in the vertical plane on the chromaticity, which is in accordance with theory. In the horizontal plane on the other side, there is a small effect observable if one goes down to low chromaticity. The horizontal chromaticity increases with increasing CLIC damping wiggler field, which is not compatible with linear theory, but which is reasonable with respect to the horizontal tune change already discussed in Section 6.2 on page 60.

### 6.4. Measurement of octupole components

Besides sextupole components, there might be even higher-order multipole field components. The next order is the octupole component. This order does not cancel out, because it is an odd multipole component.

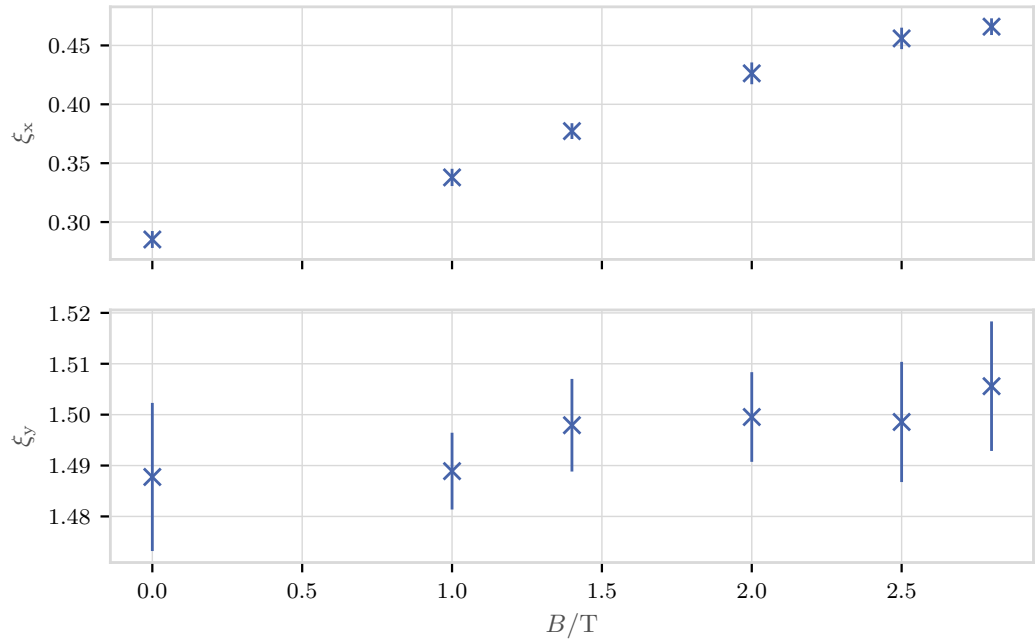


**Figure 6.6.: Wiggler field dependent chromaticity measurements at low chromaticities.** The horizontal chromaticity  $\xi_x$  increases with increasing wiggler field  $B$  (upper plot). The uncertainty of the tune measurements and the resulting uncertainty on the fit for the vertical chromaticity  $\xi_y$  (lower plot) dominate this measurement. The error bars indicate the standard deviation of the cubic fits to the momentum dependent tune change—the chromaticity. This measurements were performed at 2.5 GeV optics with a reduced chromaticity. Fill 6262.

Most storage rings do not have dedicated octupole or higher multipole magnets. At **KARA** there are none either. However, the dipoles show an octupole component, as described in [MBH<sup>+</sup>03]. In other storage rings wigglers also caused additional octupole components, like at SPEAR or BESSY [Saf89, Wal93]. These additional octupole components cannot be compensated, because there are no octupole magnets that could act against them. But since these multipole components are the next higher-order components they are the most likely to influence the operation of the ring, because the effects of higher multipoles decrease with the order. Furthermore, octupole components are interesting, because due to the four-fold symmetry of **KARA** their effects cause fourth-order resonances of the kind  $m\nu_x + n\nu_y = N/4$  where  $m, n$ , and  $N$  are integers, see e. g. [KB90].

#### 6.4.1. Orbit bumps

One way to find octupole components is to use orbit bump measurements as described in Section 3.3.3 on page 29.

From the expansion of the equation of motion for the vertical plane the octupole component of the wiggler field can be identified as the third-order term, highlighted in green here, as

**Table 6.1.: Wiggler field dependent chromaticity.** Chromaticities (horizontal–top ( $\xi_x$ ) and vertical–bottom ( $\xi_y$ )) depending on the wiggler’s magnetic field. The first order chromaticity was chosen to be small to see even small absolute changes of it. Higher order chromaticities are dominated by their uncertainties. The horizontal chromaticity increases slightly with increasing wiggler field whereas the vertical chromaticity is dominated by the uncertainties on the measurement. Measurements were done at 2.5 GeV with optics with reduced chromaticities. The tunes  $\nu_{x,y}$  show the already discussed quadratical behaviour in the vertical plane and slightly decrea in the horizontal plane. Fill 6262.

Wiggler field / T	$\xi_x$	$\nu_x$
0.00	$0.285 \pm 0.007$	$0.77949 \pm 0.00003$
1.00	$0.338 \pm 0.008$	$0.7786 \pm 0.0003$
1.40	$0.377 \pm 0.007$	$0.77713 \pm 0.00003$
2.00	$0.426 \pm 0.009$	$0.77616 \pm 0.00004$
2.50	$0.456 \pm 0.009$	$0.77566 \pm 0.00004$
2.80	$0.466 \pm 0.007$	$0.77575 \pm 0.00003$
Wiggler field / T	$\xi_y$	$\nu_y$
0.00	$1.488 \pm 0.015$	$0.69035 \pm 0.00006$
1.00	$1.489 \pm 0.008$	$0.69245 \pm 0.00003$
1.40	$1.498 \pm 0.009$	$0.69393 \pm 0.00004$
2.00	$1.500 \pm 0.009$	$0.69774 \pm 0.00004$
2.50	$1.499 \pm 0.012$	$0.70155 \pm 0.00005$
2.80	$1.506 \pm 0.013$	$0.70415 \pm 0.00005$

described in [KB90, Saf89]:

$$\begin{aligned}
 \langle y \rangle'' &= -\frac{1}{4\rho^2 k} \sinh(2k_z \langle y \rangle) \\
 \langle y \rangle'' &\approx -\frac{1}{2\rho^2} \langle y \rangle - \frac{k_z^2}{3\rho^2} \langle y \rangle^3 - \dots,
 \end{aligned} \tag{6.2}$$

with the bending radius  $\rho$  at the wiggler’s poles, the focussing strength  $k$ , the wave number  $k_z = k_y = \frac{2\pi}{\lambda_w}$ , and the mean offset in  $y$ -direction  $\langle y \rangle$  and its second derivative. The octupole-like component—sometimes also-called pseudo octupole—that would cause a similar behaviour of the electrons is, see [Wal93]:

$$B_3 = \frac{e}{\gamma m_0 c} \frac{B^2 k_z^2}{3}. \tag{6.3}$$

For the connection between the third-order term of the equation of motion in a wiggler Eq. (6.2) and the octupole component of a general magnetic field Eq. (6.3) see Appendix B.7 on page 106.

One method to measure the octupole component is the **amplitude-dependent tune shift, also-called detuning with amplitude (ADTS)** measurement technique which will be described in Section 6.4.2 on page 71. Bumping the orbit to investigate the octupole components is a simplification of the ADTS method. It has been used e. g. by [Saf89] as well. Because

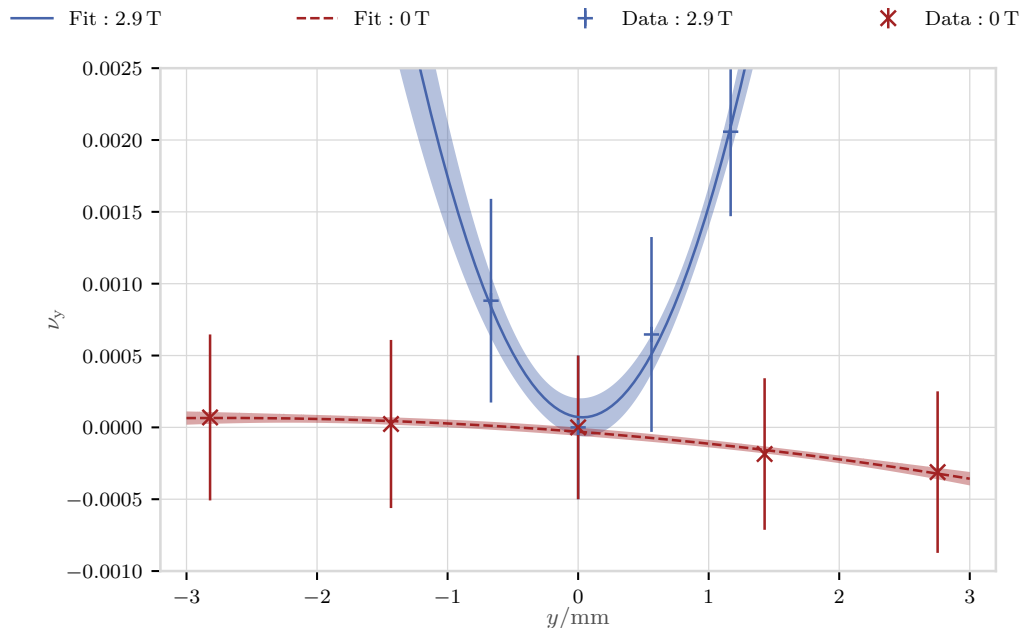


**Figure 6.7.: Vertical tune shift with vertical bump.** The measurement points for 2.9 T (blue) and 0 T (red) wiggler field of the vertical tune difference between an orbit with a vertical bump and one without are shown in red and blue with their propagated uncertainty on the tune readout. Fits including their  $1\sigma$  confidence bands (measured in Aug. 16):  
 $\nu(y)_{\text{without}} = (-1.3 \pm 7.6) \cdot 10^{-5}y^2 + (-7 \mp 13) \cdot 10^{-5}y + (-3 \pm 42) \cdot 10^{-5}$   
 $\nu(y)_{\text{with}} = (1.6 \pm 0.8) \cdot 10^{-3}y^2 + (-1 \mp 7) \cdot 10^{-4}y + (7 \pm 37) \cdot 10^{-5}$   
 The tune shift with  $x^2$  at 0 T, so *without* field, is compatible with 0, whereas the one *with* a wiggler’s magnetic field of 2.9 T is not.

the bump is done using the corrector magnets, and not just the injection kickers like in the case of ADTS, also a vertical bump is possible. If the vertical (horizontal) tune shifts quadratically with the vertical (horizontal) orbit offset from the centre, it indicates an octupole-like component of the wiggler’s field. If it shifts linearly it is a sextupole like component and if it shifts in the opposite plane then it might be a skewed sextupole or octupole-like component.

In plot Fig. 6.7 the vertical tune change is plotted against the vertical orbit bump at the wiggler’s position. The quadratic fit through the red data points of the 0 T field with the blue  $1\sigma$  error-band does not show a clear quadratic behaviour, but is consistent with zero tune shift. The blue data points for the case of a wiggler field of 2.9 T, however, do show a polynomial behaviour with an even polynomial. Though the uncertainty is very large, due to the small accessible bump range, the difference between the two cases is clearly visible.

A similar behaviour should be visible for the horizontal plane, as with Eq. (2.22) on page 19, but scaled with the horizontal  $\beta$ -function. The  $\beta$ -functions are taken from simulations based on models for the exact optics of each measurement campaign. The horizontal  $\beta$ -function is 9 times larger at the wiggler’s position than the vertical one. That implies that the tune shift caused by the bump should be larger by this factor, too.

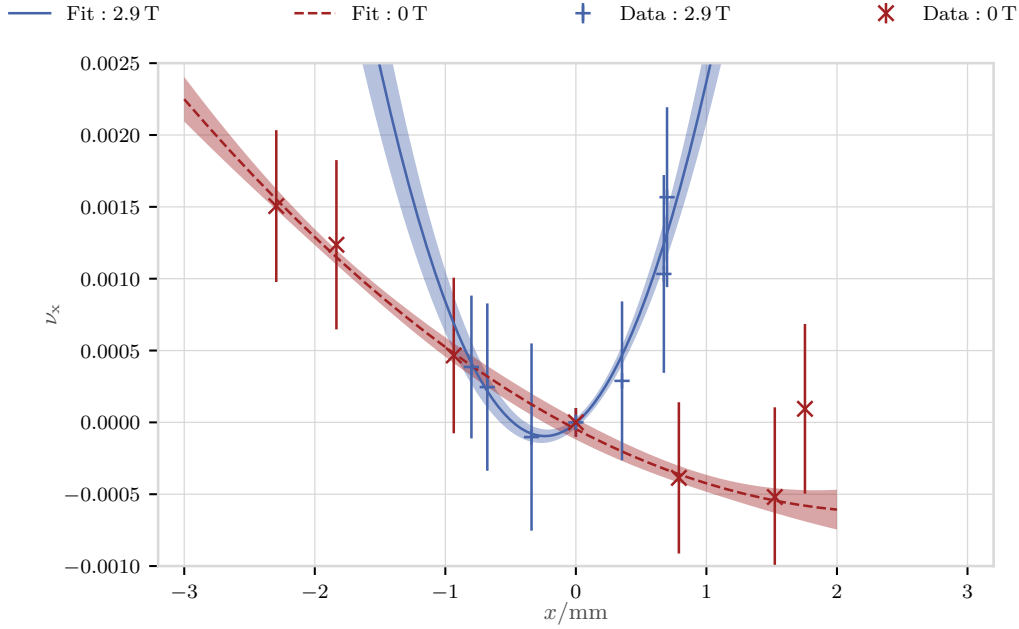


**Figure 6.8.: Horizontal tune shift with horizontal bump.** The measurement points for 2.9 T and 0 T wiggler field of the horizontal tune difference between an orbit with a horizontal bump and one without are shown in red and blue with their propagated uncertainty on the tune readout. For the reference fit of the 0 T case, the data point at  $x = 1.8$  was not included into the fit, because this large tune change in the opposite direction is most likely caused by other causes, though including it into the fit does not change the qualitative result. Fits including their  $1\sigma$  confidence bands (measured in Aug. 16):

$$\begin{aligned}\nu(x)_{\text{with}} &= 1.6 \pm 0.6 \cdot 10^{-3}x^2 + 8 \pm 4 \cdot 10^{-4}x - 0 \pm 1 \cdot 10^{-4} \\ \nu(x)_{\text{without}} &= 1.4 \pm 0.9 \cdot 10^{-4}x^2 - 3.7 \pm 1.6 \cdot 10^{-4}x - 1 \pm 10 \cdot 10^{-5}\end{aligned}$$

The tune shift with  $x^2$  at 0 T, so *without* field, is one order smaller than the one *with* a wiggler's magnetic field of 2.9 T.

Fig. 6.8 shows the plot of the horizontal tune change for a horizontal orbit bump. It also shows the expected parabolic behaviour for the case where the wiggler is turned on. Furthermore, it has got already a gradient of the fit through the data points for no wiggler field. Nevertheless, the gradient is compatible with a linear change. Thus the difference of these two gradients, with and without wiggler field, still reflects a change caused by an additional octupole component. In comparison to Fig. 6.7 on the previous page the dependency on the  $\beta$ -function is not visible, since the change is not larger by a factor of 9.

Further measurements were dominated by instabilities of the tune readout or drifting orbits. Non-linear orbit drifts also cause non-linear tune shifts and therefore spoiled further measurements. They are listed in the appendix in Table A.3 on page 100 for completeness.

The octupole component results from the difference of the quadratic term of the fits for

0 T and 2.9 T. For the vertical case it results in

$$\begin{aligned}\frac{\Delta\nu_y}{y^2} &= \frac{\nu_{y,2.90\text{T}}}{y^2} - \frac{\nu_{y,0\text{T}}}{y^2} \\ &= (1.6 \pm 0.8) \cdot 10^{-3} \frac{1}{\text{m}^2} + (1.30 \pm 7.60) \cdot 10^{-5} \frac{1}{\text{m}^2} = (1.6 \pm 0.8) \cdot 10^{-3} \frac{1}{\text{m}^2}\end{aligned}$$

and for the horizontal case in

$$\frac{\Delta\nu_x}{x^2} = (1.6 \pm 0.6) \cdot 10^{-3} \frac{1}{\text{m}^2} - (1.4 \pm 0.8) \cdot 10^{-4} \frac{1}{\text{m}^2} = (1.5 \pm 0.6) \cdot 10^{-3} \frac{1}{\text{m}^2}.$$

## 6.4.2. Amplitude Dependent Tune Shift (ADTS)

### 6.4.2.1. Tunes acquisition with FFT

In principle the ADTS measurement, see Section 2.1.6 on page 16 and Section 3.3.4 on page 31, is the more accurate measurement of the multipole component, but is only applicable on the horizontal plane where the injection kickers excite the beam.

However, a tune readback is needed that is appropriate for short measurements to measure the tune amplitude-dependent. If one calculates the tune as it is usually done via an FFT, the accuracy of the calculation scales with  $1/N$  where  $N = 1750$  is the number of turns per measurement. This limits the resolution of the measurement to tune changes of 0.00057. Increasing the number of data points, or turns in this case, does not make sense, because the beam is already damped after this time, as can be seen in the numbers of turns in Fig. 6.9a on page 73. The amplitudes can be differentiated with e.g. 100 points, but the tune differences must be greater than 0.01. Using a sliding window  $(i, i + 1, i + 2, \dots)$  with more data points instead of a shifted window  $(i, i + \text{window length}, i + 2 \cdot \text{window length})$  with less points can improve the situation slightly. Nonetheless, this is not sufficient, as the tunes change about 0.0007 at the maximum as we will see further below in this subsection, so too few tunes, two, could be distinguished.

In the measurements the BPM sensing the highest orbit excitation amplitude is taken for the tune calculation and the two ones closest to the wiggler for determining the average amplitude inside the wiggler. This can be done since the tune is an integrated value and therefore it does not depend on the position in the ring where it is determined.

Because each shot differs from the next one, 20 shots were taken in a row to get more samples to average over, to get statistics also for higher amplitudes.

To evaluate the ADTS method, measurements have been carried out. These showed that it is possible to go up to an amplitude of 0.75 mm with the injection kicker at 2.5 GeV at maximum kick strength. For smaller energies the amplitude is larger for the same kick strength. For the much less stiff beam at 1.3 GeV the limit was not the kicker magnet, but the beam stability. It was only possible to go to amplitudes of 0.50 mm. Knowing this, one can calculate the ADTS for the respective energies and corresponding beta functions

**Table 6.2.: Theoretical ADTS predictions.** Theoretical horizontal amplitude dependent tune shift using Eq. (2.26). Rows with a grey background indicate that the tune shift is too small for a measurement with the discussed ADTS measurement technique. Already published in [G<sup>B</sup>B<sup>+</sup>17].

Wiggler field $B/\text{T}$	Energy $E/\text{GeV}$	Amplitude $\Delta x/\text{mm}$	Tune change $\Delta\nu_x$
1.40	1.30	0.50	0.0002
1.40	2.50	0.75	0.0002
2.00	1.30	0.50	0.0005
2.30	1.30	0.50	0.0005
2.90	2.50	0.75	0.0007

using Eq. (2.26) on page 21. This was done as shown in Table 6.2, already published in [G<sup>B</sup>B<sup>+</sup>17]. The values shown in grey do not show a tune change that is larger than a range of two times the uncertainty. The listed values in Table 6.2 for the 1.3 GeV case show energy, amplitude, and tune change firstly for the maximum magnetic field values of the wiggler possible with an unchanged 1.3 GeV optics— $B = 1.40$  T—, secondly the realised maximum value with optics corrections, that is  $B = 2$  T, and thirdly the maximum value reached in simulations, which is 2.30 T.

From this calculation it is clear that it is not possible to achieve sufficiently large tune changes for the stable 1.40 T at 1.3 GeV case, nor for the same field at 2.5 GeV. That implies that it is not possible to use FFTs for ADTS comparisons at different energies. At least it is not, without developing new optics for the 1.3 GeV mode that would have to result in higher possible wiggler’s fields, which is out of the scope of this work.

#### 6.4.2.2. Tunes acquisition with NAFF

Another method to get the tune is the Numerical Analysis of Fundamental Frequencies (NAFF) [Las93, ZPA<sup>+</sup>15]. With this method it is possible to get to the precision of KARA’s regular tune readout of  $10^{-4}$  within 25 turns [ZPA<sup>+</sup>15]. It also was tested for this purpose similar to how it is described in [ZPA<sup>+</sup>15].

#### 6.4.3. Evaluation of the ADTS measurements

After measuring the beam position for about 1750 turns after a kick, and repeating this 20 times (shots) per kick strength, one data set is compiled. For the energies 1.3 GeV, 1.60 GeV, and 2.5 GeV these measurements have been carried out for different wiggler fields while not compensating the optics changes introduced by increasing wiggler field. Therefore the maximum wiggler fields are 1.40 T, 1.40 T, and 2.90 T for the different energies, respectively.

The first step of the evaluation consists of the following parts. The oscillations are shifted by subtracting the mean of the signal, because the centre of the BPM is not necessarily the centre of the oscillation. Then the data taken before the kick, including the kick itself is removed, so that ca. 1750 turns of initially 2000 turns are available for further analysis.

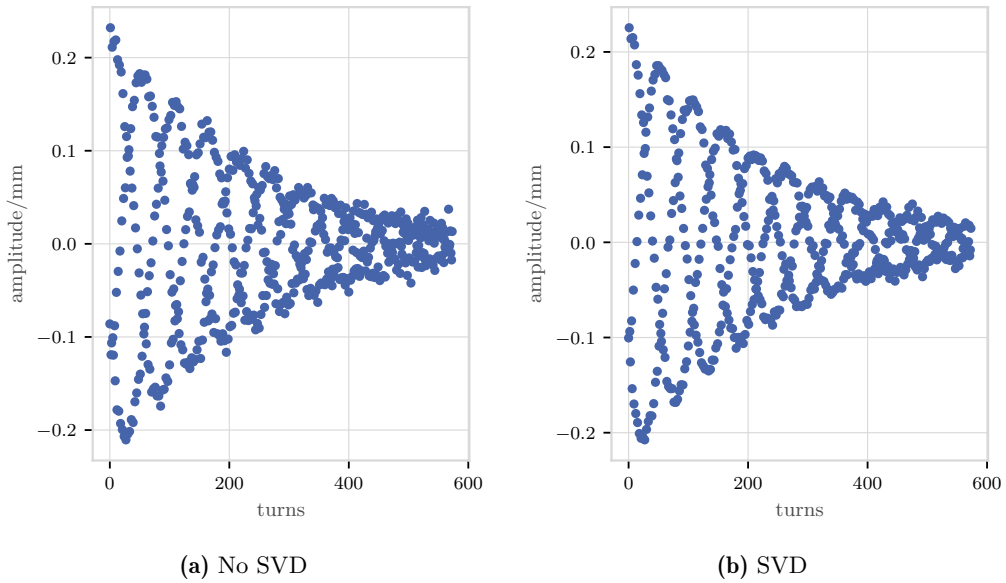


**Figure 6.9.:** Comparison of unprocessed data and after SVD. The oscillation of caused by a kick is damped in less then 1000 turns. The raw turn by turn data in 6.9a has been smoothed in 6.9b by applying a singular value decomposition (SVD) onto the turn by turn signals for each turn times the BPMs. In both cases only each third turn is displayed for a better visualisation.

The amplitudes of these measured beam oscillations are normalized to the  $\beta$ -function by dividing by the square root of the  $\beta$ -function (see Eq. (2.3) on page 7). Now data measured by different BPMs for one shot should start at the same amplitude and should be damped similarly. Of course the amplitude is not the same for different kick strength. Afterwards the data have been smoothed by applying a singular value decomposition (SVD) to the  $\text{BPM} \times \text{turns}$ -matrices, as described in e. g. [ZPA<sup>+</sup>15, Wan03]. With the SVD the data points not following a periodic pattern are sorted out so the proper signal is enhanced. This does not always improve the data. Due to practical reasons a comprehensive analysis of *one* shot was done and the hyper-parameter—the limit of modes to take—was chosen ( $\text{lim}=4$ ). This implies it is not necessarily the best choice for *all* shots.

Each of these pre-processed data sets can now be processed further. The amplitudes are calculated by first getting the envelope of the damping with SciPy’s Hilbert transform ([VGO<sup>+</sup>20]) and averaging over the slices used for the tune calculation. The tunes were calculated using the NAFF algorithm for all 39 BPMs sliced into slices of 64 turns which is sufficient to get a proper tune readout, following [ZPA<sup>+</sup>15]. The Numerical analysis of fundamental frequencies (NAFF) [Las93] finds the most dominant frequencies for quasi-periodic functions

$$f(t) = \sum_{k=1}^{\infty} a_k e^{i\nu_k t} \quad (6.4)$$

for decreasing  $a_k$ . It searches the maximum amplitudes of the weighted products of  $f(t)$  with  $e^{i\sigma t}$ . Weighting is done using e. g. the Hann window ( $\chi(t) = 1 + \cos(\pi t/T)$ ). This maximum provides the first frequency from which the corresponding first amplitude can be

deduced by orthogonal projections. Further frequencies and amplitudes are then calculated by applying this algorithm to the function itself minus the first dominant part  $f(t) - a_1 e^{i\nu_1 t}$ . Lastly, the function set needs to be orthogonalised.

When using the Hann window the error decreases with  $1/T^3$  instead of  $1/T$  like for the **FFT**.

A further advantage of using **NAFF** in comparison to **FFT**s is that the error can be minimised to  $1/(M^{2p+1}N^{2p+2})$  with the order of the Hann window  $p$  for  $M$  **BPM**s and  $N$  turns when using the information of all **BPM**s as described by P. Zisopoulos in [ZPL19, ZPA<sup>+</sup>15]. This is possible, because the **BPM** signals depend on the  $\beta$ -function linking the information from one to the next **BPM** and the signals repeat after a turn. For **NAFF** the errors occurring due to not equidistant **BPM**s cancel out, whereas they do not for **FFT**s, resulting in the performance improvement only for **NAFF**.

As the tune depends on the amplitude, but not on the initial state, all data for one energy and one wiggler's magnetic field are taken as one measurement.

These data are depicted in Fig. 6.10e on page 76 for the example of 2.5 GeV and 2.90 T as well as for all magnetic fields in Fig. 6.13c. The parameters of the quadratic fits through the different cases are listed in Table 6.3 on the next page. Especially for smaller amplitudes the tune spread is very large, which originates mainly from the fact that the tune measurement expects an excited beam and the beam is already damped at these amplitudes. The large uncertainty in the higher amplitudes comes from the Hilbert transformation which tends to overshoot at the discontinuous beginning. The fits are done using SciPy's [VGO<sup>+</sup>20] least-square implementation.

The gradients of the fits against the magnetic fields are plotted in Figs. 6.13 and 6.13a to 6.13c on page 79. In the case of 2.5 GeV the slopes of the **ADTS** measurements increase with increasing field up to 2.5 T, but decrease for the 2.90 T case. All second-order gradients are negative. Except for the 2.5 T case the second-order gradient is almost the same with respect to the uncertainties. For the 1.60 GeV case the 0 T slope is the lowest again and the slopes rise with the field. However, the differences between the slopes of 0.50 T and 1 T are not significant though the step size is equal to that down to 0 T or up to 1.50 T. The values of the second-order gradients are in the range of 500 to 1000. The 1.3 GeV measurements behave even more differently. The slopes and second-order gradients do not show a trend, instead the slopes for 0.50 T and 1 T are below that for 0 T, whereas that for 1.50 T is above and the second-order gradients for 0.50 T and 1 T are positive.

Because the magnetic field of the wiggler is optimised for working above 1.3 T, the behaviour below this value might be spoiled by not well compensated field integrals. This might explain especially the incoherent behaviour of the 0.50 T and 1 T case.

However, also with the **NAFF** evaluation method it was not possible to see the relationship between the amplitude dependence and the tune shift for different wiggler fields nor for

**Table 6.3.: Fits for ADTS measurements.** Linear fits to the ADTS measurements with their standard deviations are listed for the three different energies 2.5 GeV (6.4a), 1.6 GeV (6.4b), and 1.3 GeV (6.4c).

(a) 2.5 GeV	
$B/T$	Fit $\nu(x)$
0.00	$(0.779833 \pm 0.000005) + (0.00404 \pm 0.00013)x - (0.0048 \mp 0.0006)x^2$
1.50	$(0.777365 \pm 0.000004) + (0.00459 \pm 0.00012)x - (0.005 \mp 0.0005)x^2$
2.00	$(0.776589 \pm 0.000005) + (0.00496 \pm 0.00013)x - (0.0054 \mp 0.0006)x^2$
2.50	$(0.776326 \pm 0.000005) + (0.00692 \pm 0.00015)x - (0.0124 \mp 0.0007)x^2$
2.90	$(0.776020 \pm 0.000005) + (0.00486 \pm 0.00014)x - (0.0053 \mp 0.0007)x^2$
(b) 1.60 GeV	
$B/T$	Fit $\nu(x)$
0.00	$(0.775506 \pm 0.000006) + (0.95 \pm 0.06)x - (966 \mp 117.0)x^2$
0.50	$(0.774329 \pm 0.000005) + (0.98 \pm 0.05)x - (886 \mp 90.0)x^2$
1.00	$(0.773487 \pm 0.000004) + (1.06 \pm 0.04)x - (992 \mp 77.0)x^2$
1.50	$(0.771993 \pm 0.000009) + (0.98 \pm 0.09)x - (665 \mp 178.0)x^2$
(c) 1.3 GeV	
$B/T$	Fit $\nu(x)$
0.00	$(0.79417 \pm 0.00001) + (0.00122 \pm 0.00016)x - (0.0014 \mp 0.0005)x^2$
0.50	$(0.79355 \pm 0.00001) - (0.0006 \mp 0.00011)x + (0.0026 \pm 0.0003)x^2$
1.00	$(0.79261 \pm 0.000008) - (0.00048 \mp 0.00010)x + (0.0027 \pm 0.0002)x^2$
1.50	$(0.78970 \pm 0.000008) + (0.00297 \pm 0.00011)x - (0.0028 \mp 0.0003)x^2$

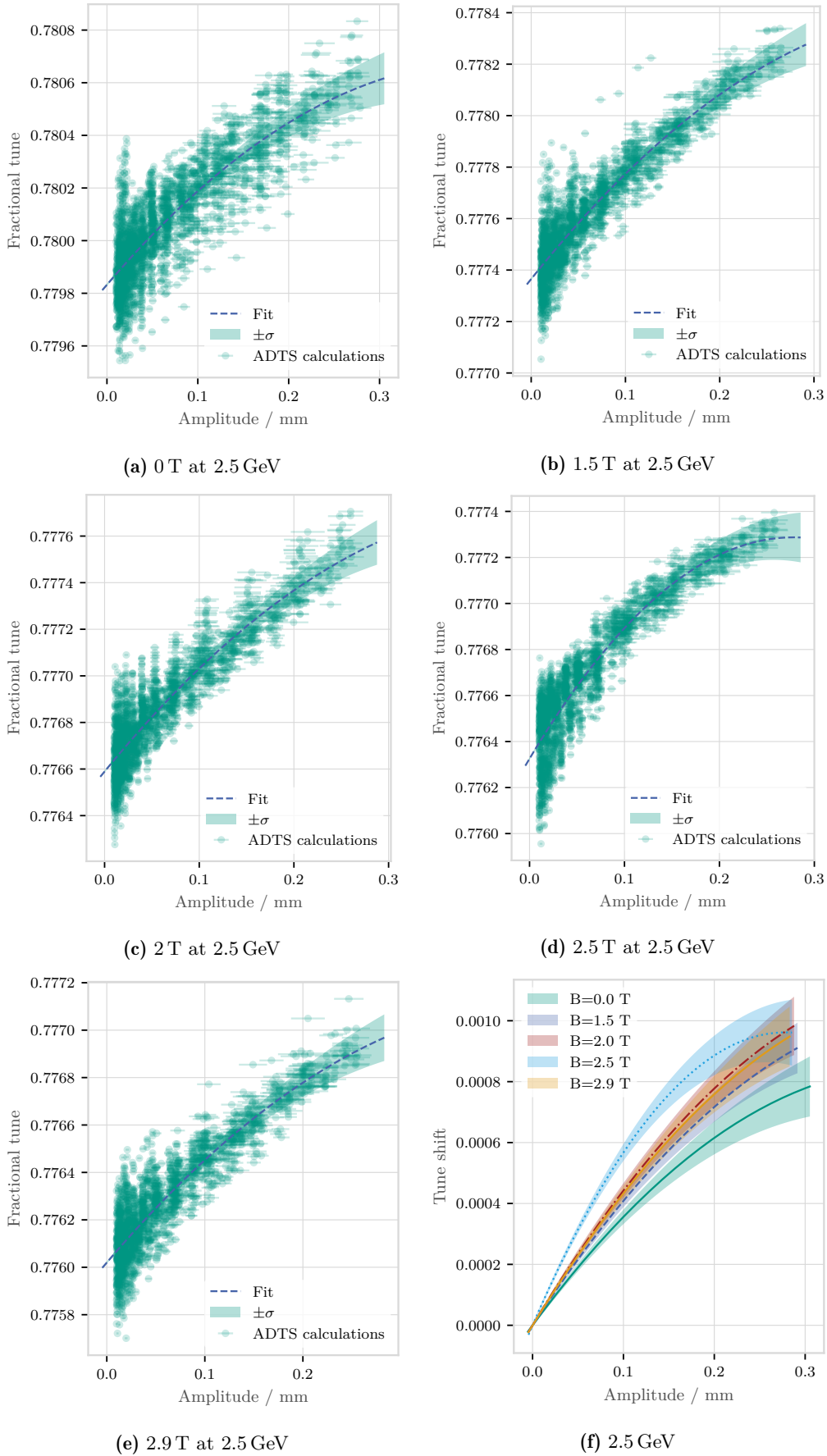


**Figure 6.10.: Amplitude dependent tune shift measurement at 2.5 GeV.** Measurements for different wiggler fields. In Fig. 6.13c the individual orthogonal distance regression fits for the different fields have been subtracted by their means to compare the fits without the offset caused by the tune shift of the wiggler's field.

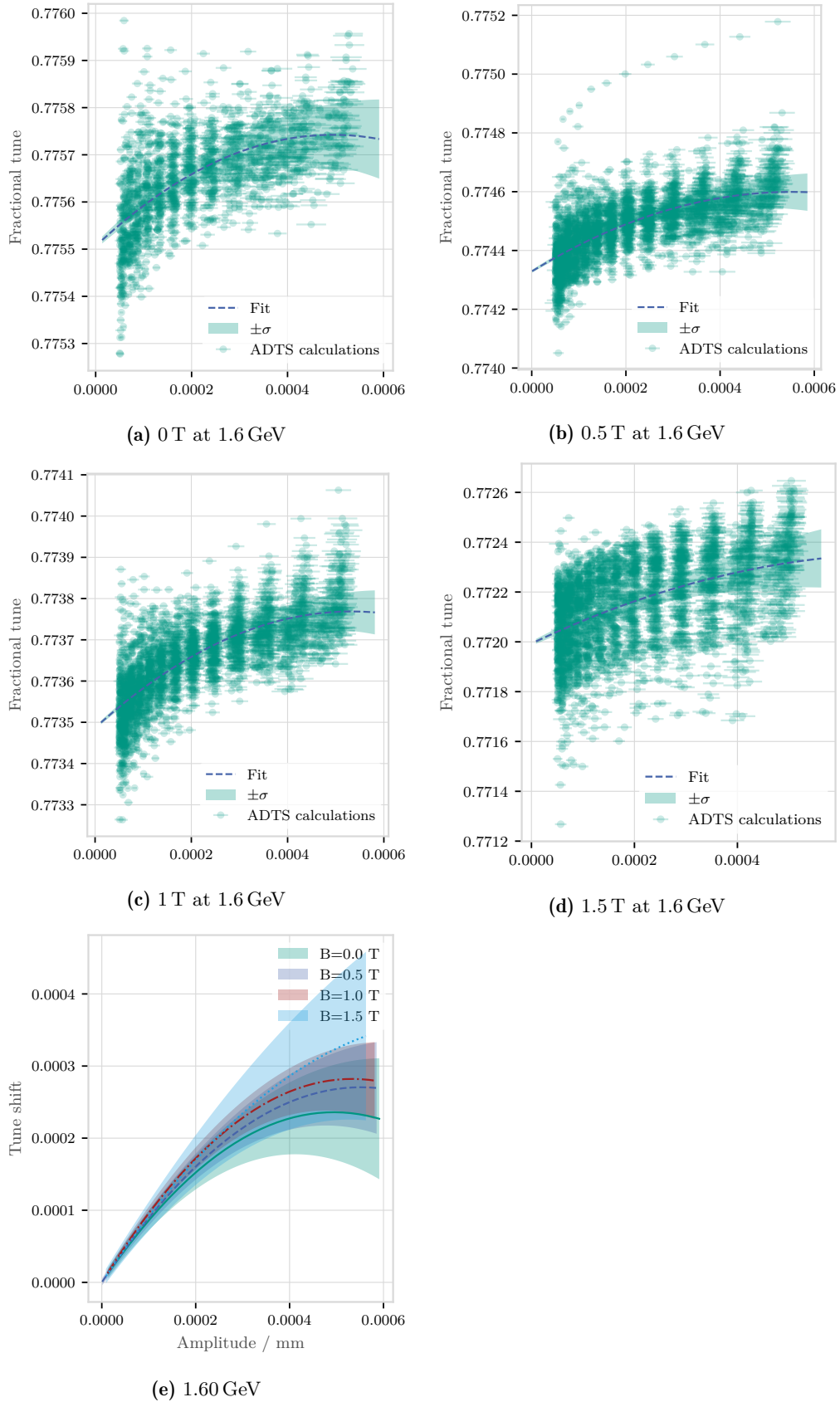


**Figure 6.11.: Amplitude dependent tune shift measurement at 1.6 GeV.** Measurements for different wiggler fields. In Fig. 6.13b the individual orthogonal distance regression fits for the different fields have been subtracted by their means to compare the fits without the offset caused by the tune shift of the wiggler's field.

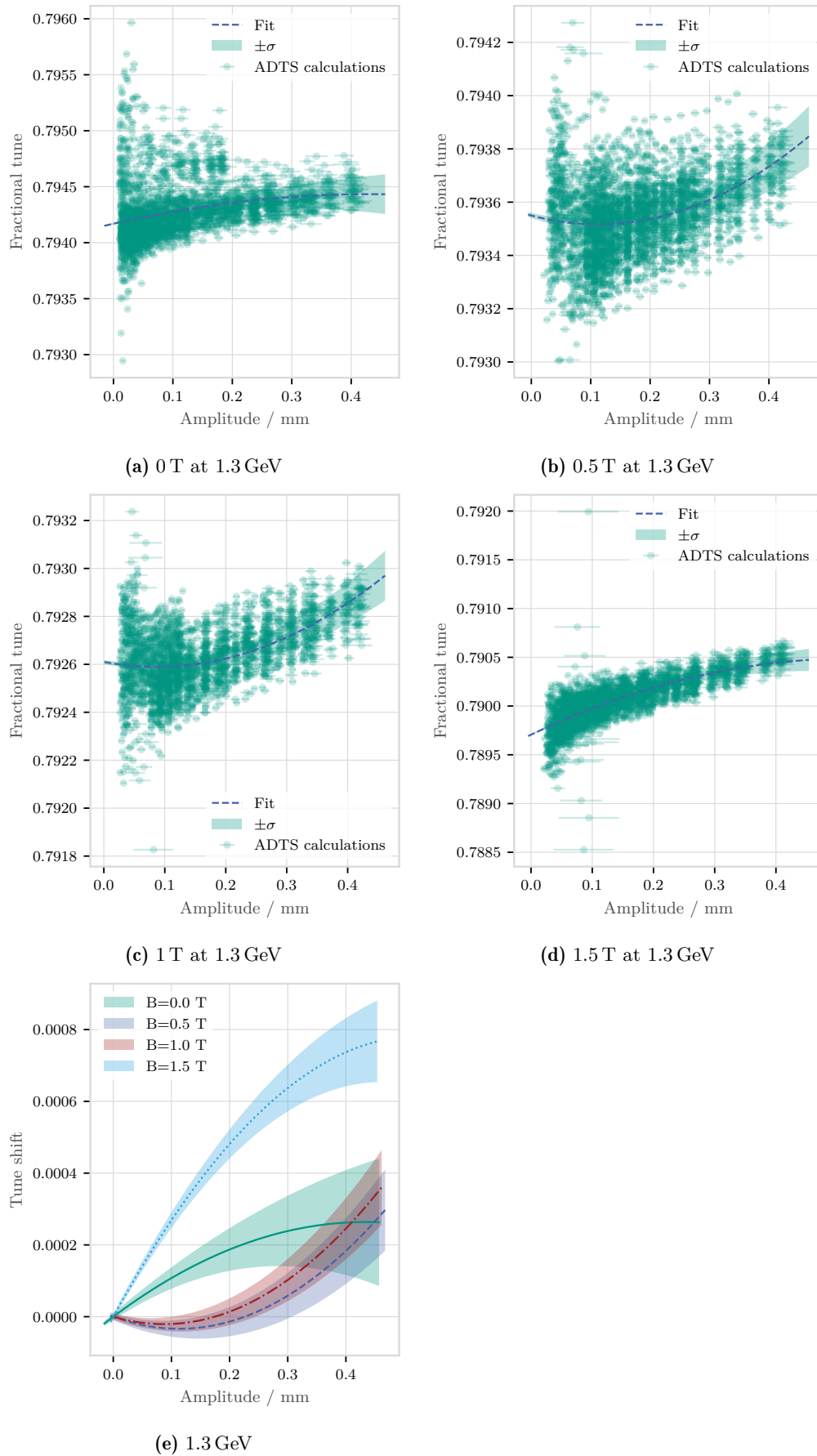


**Figure 6.12.: Amplitude dependent tune shift measurement at 1.3 GeV.** Measurements for different wiggler fields. In Fig. 6.13a the individual orthogonal distance regression fits for the different fields have been subtracted by their means to compare the fits without the offset caused by the tune shift of the wiggler's field.

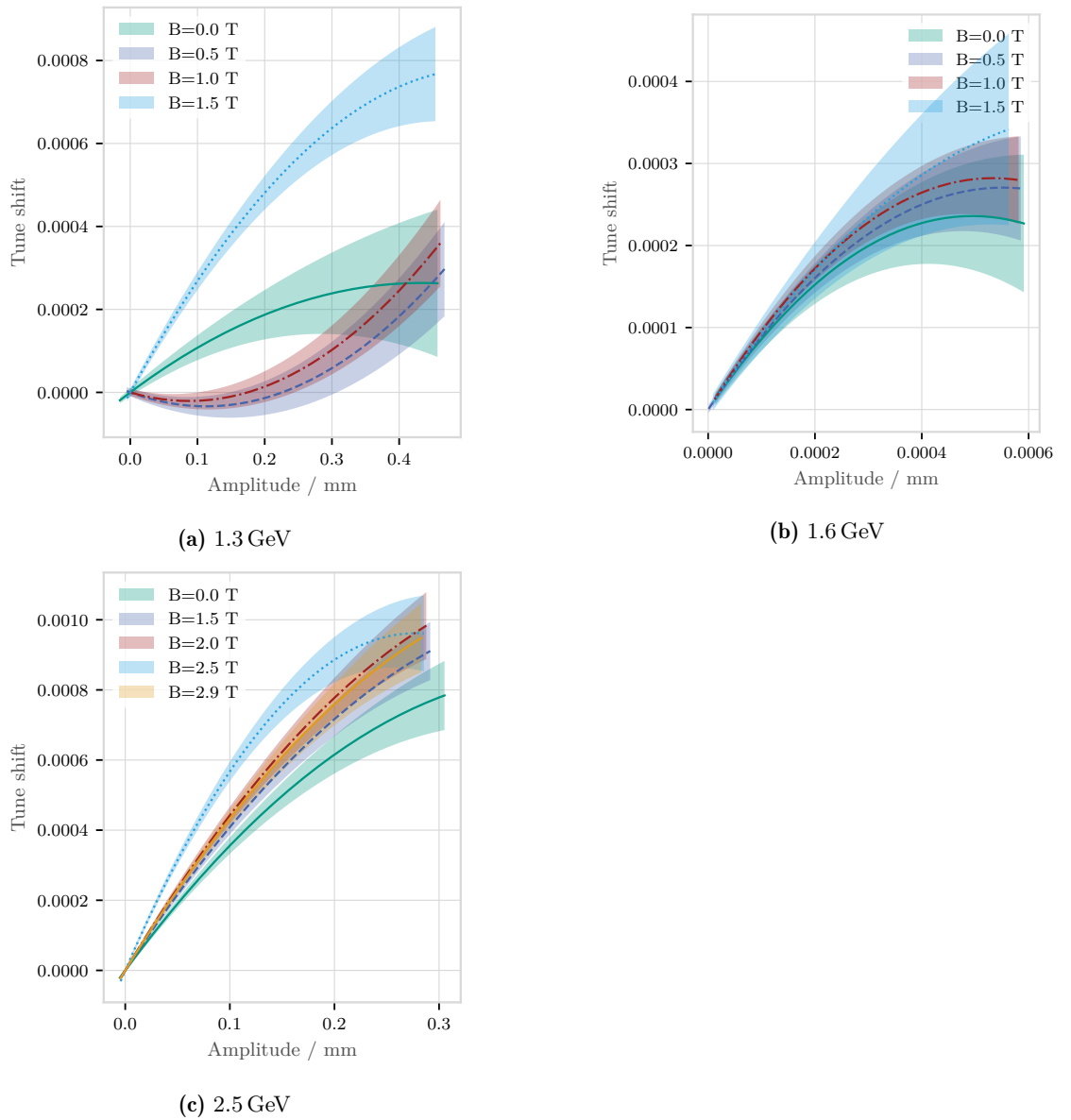


**Figure 6.13.: Comparison of the fits.** Comparison of the fits to the ADTS measurements for the different energies.

different energies. Hence the octupole component of the wiggler field cannot be determined precisely. This method mainly suffered from too small amplitudes of the kicks. They are also limited by the strength of the injection kicker, so one cannot predict the type of function that might describe the shape of the distribution of measurement points. In contrast to the orbit bump measurement the general shape of the distribution is similar for the different energies 1.3 GeV, 1.60 GeV and 2.5 GeV and furthermore, there is no wiggler field dependence visible.

#### **6.4.4. Conclusion of the evaluation of octupole components utilising tune measurements**

To conclude, the orbit bump measurements indicate that the wiggler has got an additional octupole component, but they are not precise enough to give a proper value of it. The **ADTS** method fails to measure the octupole component, because the resolution of the tune read-out is lower than the small amplitude changes caused by the wiggler.

Nevertheless, these indications led to further investigations of beam lifetime decrease at **KARA** caused by octupole resonances caused by **CLIC** damping wiggler and the **CATACT**-wiggler and finally to change of the working point, see [PBG<sup>+</sup>17].

## 7. Effects in the short-bunch operation mode

In this section, the effects of the wiggler on the beam and the THz-spectrum in the short-bunch, low- $\alpha$ -mode are discussed. There are two dominant effects. The wiggler changes the optics a lot, and it also reduces the damping time which has got an influence on the radiation spectrum.

The section starts with the expected effects on the transverse and the longitudinal phase space, continues with the experimental setup and the measurements and ends with a discussion of the findings.

### 7.1. Beta-beating mitigation, radiation damping, and further transversal beam dynamics considerations

Besides the effects directly caused by the short bunches and the THz-bursting, there are many effects caused by the lower energy of 1.3 GeV as compared to 2.5 GeV and the modification of optics for this special low- $\alpha$ -mode. For the low- $\alpha$ -mode, the optics are not just adjusted to match the lower energy, but also to shorten the bunches. Therefore the dispersion is not positive all around the ring, but also negative in some parts to be close to zero when integrated over the whole ring. That causes a negative dispersion in the wiggler. Because the energy is lower, the beam is less stiff, meaning magnetic fields bend the electron beam stronger, as per the definition of  $\rho$ . Hence, the wiggler's magnetic field causes a stronger focusing and thus a stronger vertical tune change. This tune change then causes resonance crossing. This means one cannot increase the wiggler's magnetic field that much and one has to compensate the tune shift to get to fields above 1.3 T.

The wiggler introduces strong so-called vertical beta-beating, a local increase of the beta function that disturbs the beta function all over the ring. As can be seen in Fig. 7.1 on the next page the horizontal beta functions look the same for the three simulated cases of 0 T, 1.50 T—both not optimized—and 1.50 T with a lattice optimized for low beta beating. This shows that the optics in the horizontal plane is not affected by the beating, in agreement with the unchanged horizontal tune. Besides the horizontal beta function, the dispersion is also not affected much by the wiggler. The wiggler's contribution to the dispersion and therefore the local disturbance is in the order of  $10^{-5}$  m (see B.4). This is negligible

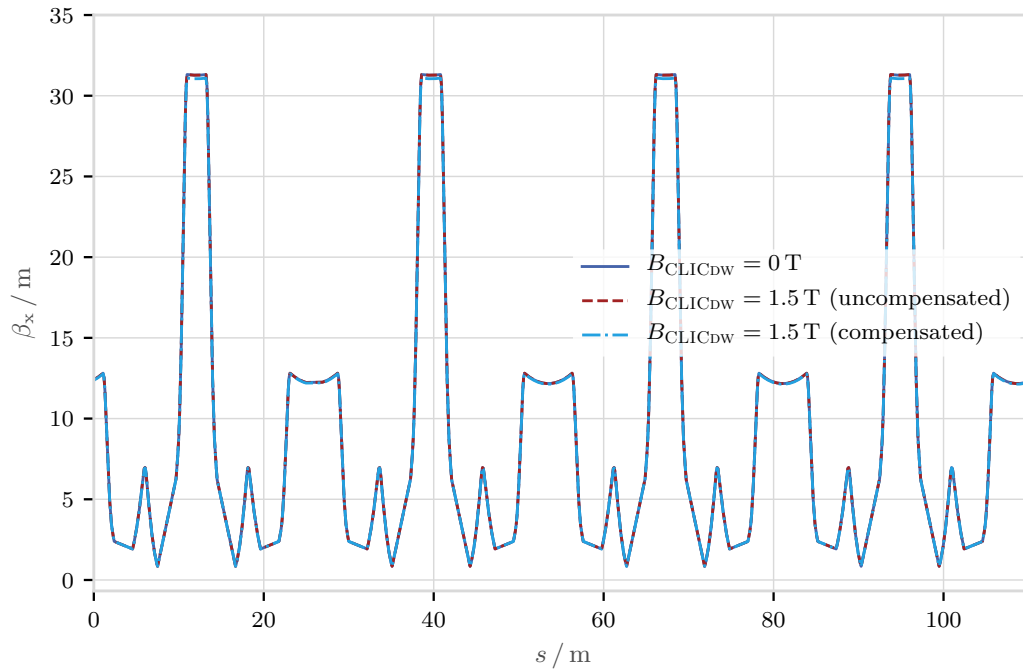


**Figure 7.1.: Simulated horizontal beta functions.** Simulations of the horizontal beta function for KARA at 1.3 GeV in the short bunch mode are shown for the three cases no wiggler field, 1.50 T (uncompensated), and 1.50 T (compensated). In the horizontal plane a wiggler should not change the beta function, so that one would not expect differences between the 0 T case and the uncompensated 1.50 T case. Optimally, one would also have no additional change caused by the compensation.

in comparison to  $-0.74$  m in the wiggler and the maximum of 1.39 m, as can be seen in Fig. 7.3 on page 84.

The vertical beta function on the other hand is strongly disturbed by the wiggler. In Fig. 7.2 on the next page the vertical beta function reaches values of about 60 m for the uncompensated case (centre plot), whereas it reaches its maximum of 25 m in the unperturbed case (topmost plot). The simulation of the 2 T case failed in the vertical plane, most likely because of too high beta amplitudes. However, if one compensates this beta beating one can reach higher wiggler fields. To increase the field optics optimizations were done, by changing the quadrupole strength and optimizing for a low maximal  $\beta_y$ -function and beta-beating. In the bottom plot of Fig. 7.2 on the facing page the best compensation for 1.50 T is shown. As one can see, it is not possible to compensate the beating completely, because the quadrupoles with which the compensation is done are not powered individually, but only in families. It is not possible to fully compensate this local disturbance with the global countermeasure. However it is possible to increase the wiggler field up to 2 T, due to these corrections.

Another effect that is caused by the wiggler that plays an important role in the later discussed low- $\alpha$  mode is that on damping time, see 2.1.6. It depends on the radiated power which is independent of the tune. Hence the beta-beating compensation does not

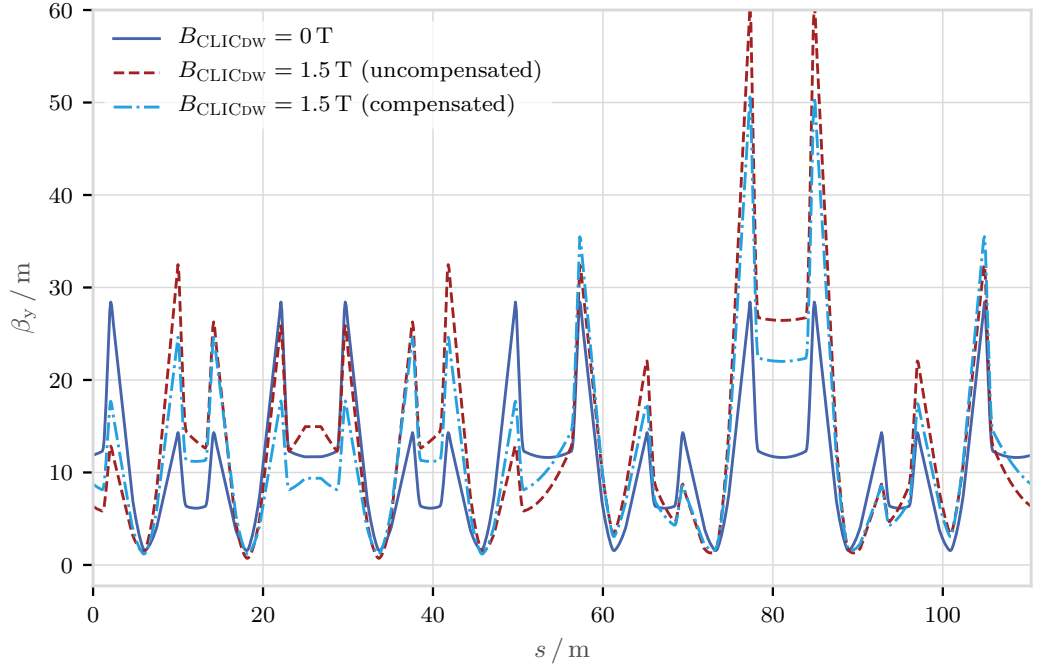


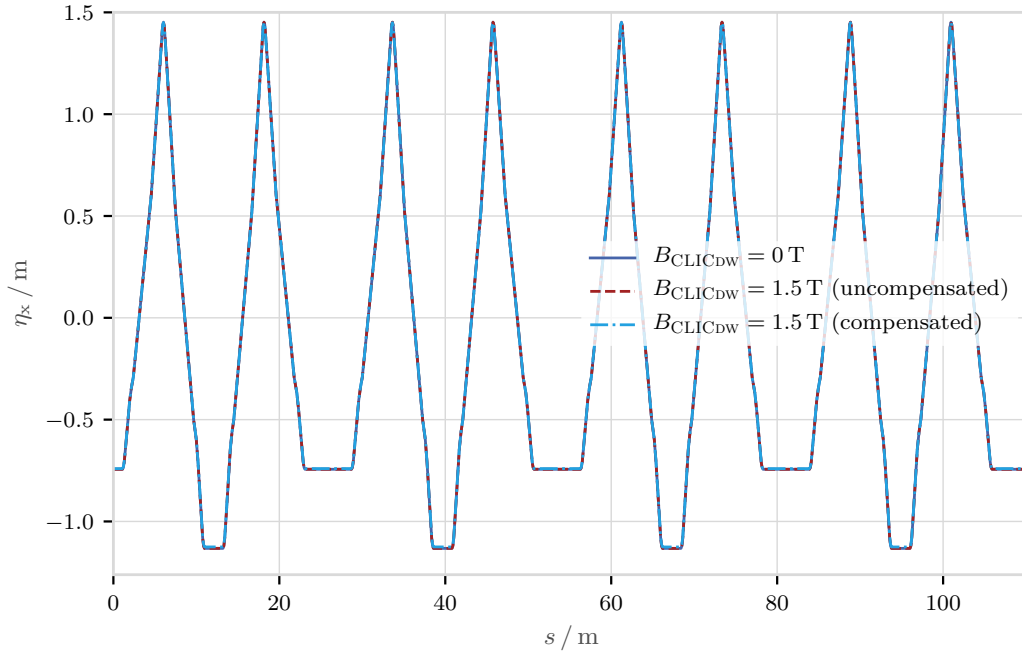
**Figure 7.2.: Simulated vertical beta functions.** Simulation of the vertical beta function for **KARA** at 1.3 GeV in the short bunch mode are shown for the three cases no wiggler field, 1.50 T and 1.50 T. The wiggler disturbs the beta function locally which leads to a global disturbance in a storage ring. The compensation tries to minimise the maximum beta and the mean deviation of the beta function. Because this local disturbance can only be acted against globally, it is expected that a complete compensation is not possible.

affect the damping time. The damping time primarily depends on the beam energy, the radiated power, and via the synchrotron radiation integrals  $\mathcal{I}_2$  and  $\mathcal{I}_4$  the local bending radius and the dispersion. Of these properties, the wiggler changes the radiated power, the local bending radius and as discussed earlier the dispersion, albeit just a little. The radiation integrals change by approximately  $\Delta\mathcal{I}_2 = 0.20 \frac{1}{\text{m}}$ , and  $\Delta\mathcal{I}_4 = -2.87 \times 10^{-5}$  using the equations for the increase caused by wigglers by [Wal93]. Simulations provide the initial  $\mathcal{I}_2 = 1.14 \frac{1}{\text{m}}$ , and  $\mathcal{I}_4 = -1.49 \times 10^{-2} \frac{1}{\text{m}}$ , as well as the changed values ( $\mathcal{I}_2 = 1.35 \frac{1}{\text{m}}$ ,  $\mathcal{I}_4 = -1.49 \times 10^{-2} \frac{1}{\text{m}}$ ). The changes of  $\Delta\mathcal{I}_4 = 2.00 \times 10^{-8} \frac{1}{\text{m}}$  are smaller and the change of the damping partition numbers  $j_x$  of 2‰ is negligible with respect to the radiation power increase of 20%, caused by the change of ( $\Delta\mathcal{I}_2 = 0.21 \frac{1}{\text{m}}$ ).

The radiation power increase is also simulated with the *elegant* model and calculated via analytical expressions. This yields the energy loss as the dominating factor for the damping time change. Therefore the focus lays on the latter in the following if the transverse plane is considered.

## 7.2. Considerations of bucket deformation in short bunch mode

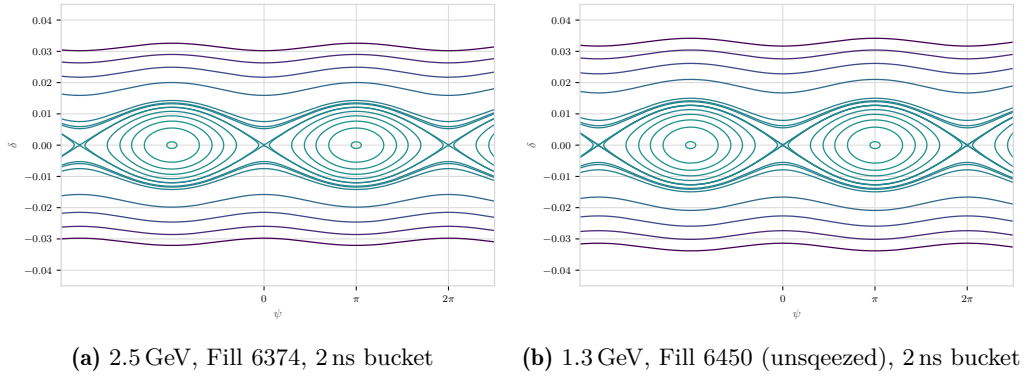
The low- $\alpha$ -mode is changing the longitudinal dynamics very much, not just the transversal planes. Thus we need to have a closer look at it as well. Tracking simulations with the



**Figure 7.3.: Simulated dispersion function.** The simulated dispersion for KARA at 1.3 GeV in the short bunch mode are shown for the three cases no wiggler field, 1.50 T and 1.50 T. As with the horizontal beta function no influence is expected, because the dispersion is a horizontal phenomenon in linear order.

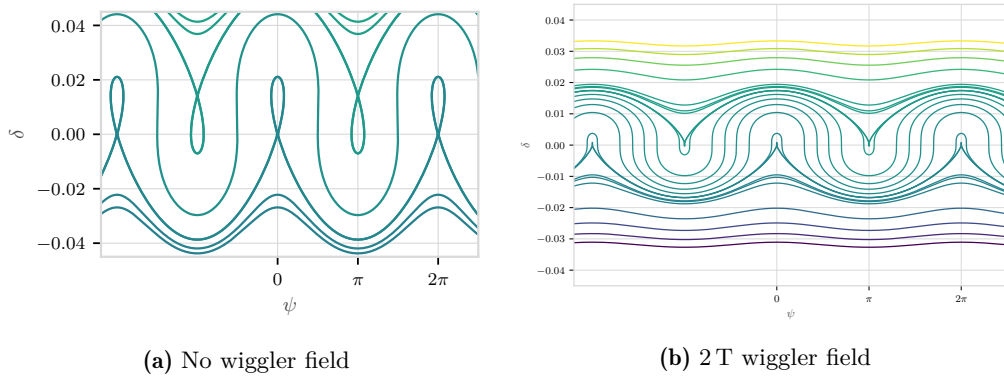
settings of the respective measurements—see also A.1—and with 1024 turns, result in a momentum compaction factor of  $\alpha_c = 3.30 \times 10^{-4}$  and with the wiggler at 2 T of  $\alpha_c = 2.72 \times 10^{-4}$ . The second-order momentum compaction factor changes from  $-2.45 \times 10^{-2}$  to  $-41.83 \times 10^{-2}$ . These changes are larger than the analytical estimates of the changes by the field change of the wiggler alone suggest, which are  $1.19 \times 10^{-7}$ , using [Wal93]. Because the synchrotron tune scales proportional to the reciproc of the squared  $\alpha_c$  and it was constant in the measurements, the momentum compaction factor should also be considered constant.

It was not possible to reliably measure the chromaticity which could have provided further information especially for the second order momentum compaction factor. Though the changes of the second order momentum compaction factor aren't negligible, their sign stays the same. Then only the size of the bucket is changed, but not the orientation of the bucket, which would be the case for a change of sign of one of the different order momentum compaction factors. As in Fig. 2.6c on page 13 the longitudinal Hamiltonian Eq. (2.10) on page 14 has been used to illustrate the phase space for the simulated parameters. In Fig. 7.4 on the next page one can see simulations of the longitudinal phase spaces for both energies 2.5 GeV and 1.3 GeV, but before shortening the bunches by optics manipulations. The plots show results of tracking simulations done for two fills at the respective energies. The size of the buckets of circa 1.80 ns does not change much. In contrast to that, the simulated buckets of the shortened bunch optics look very different as depicted in Fig. 7.5a.



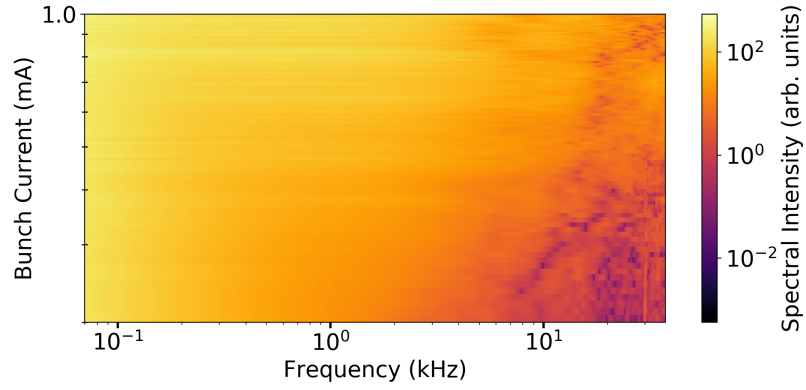
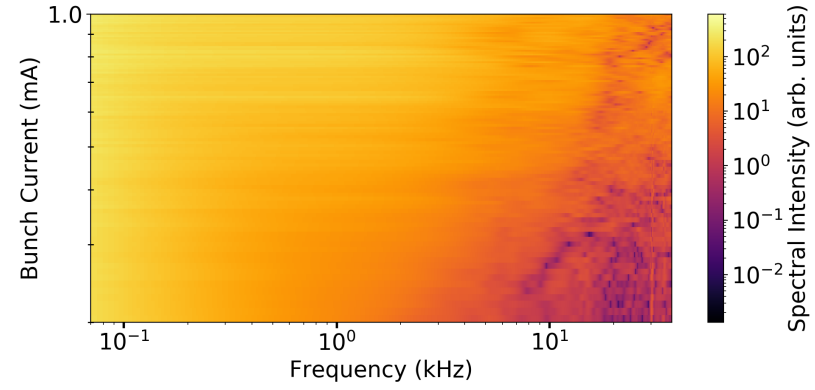
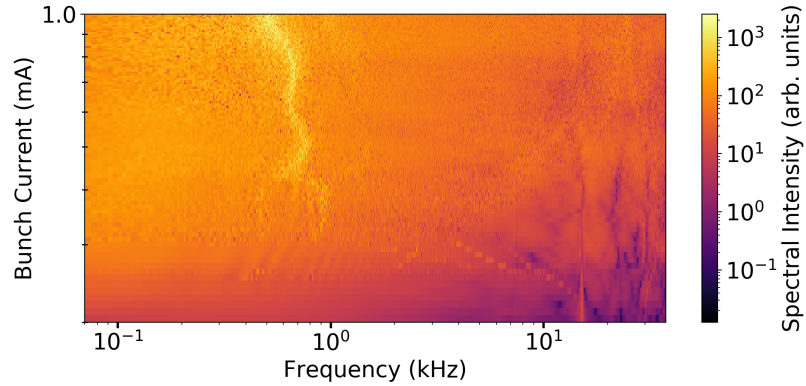
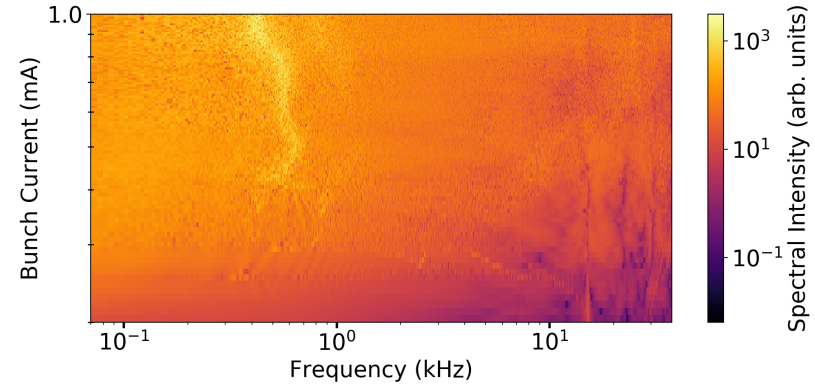
**Figure 7.4.: Simulated longitudinal phase spaces.** *elegant* simulation of the longitudinal phase spaces with LOCO fitted optics. The bucket reaches its maximum length of a bucket at **KARA** for Fill 6450 and for Fill 6374 of 2 ns or  $2\pi$ .

The bucket of the short-bunch mode with the wiggler turned on is tilted in comparison to the normal long-bunch operation mode. The figures show the isolines of the Hamiltonian plotted for the first and second-order momentum compaction factor that *elegant* simulations provide for these two optics.



**Figure 7.5.: Low-alpha bucket simulation.** Plots of the low- $\alpha$ -Hamiltonian Eq. (2.10) on page 14 showing typical low- $\alpha$ -bucket for  $\alpha_c$  values from simulations of KARA during low- $\alpha$  experiments with the **CLIC** damping wiggler turned off (Fig. 7.5a) and at 2 T with a compensated optics (Fig. 7.5b).

To ensure that the observed effects on the THz-signal are not caused by the shrunken  $\alpha_c$ -bucket, but by the change in damping time, see Section 2.1.6 on page 17, simulations with the Vlasov-Fokker-Planck solver Inovesa [SSB<sup>+</sup>19] were done. Two different momentum compaction factors  $\alpha_{c1,2}$  and two different damping times  $\tau_{1,2}$  were taken as input for simulations leaving the other input parameters the same. By this, the effects caused by this specific parameter can be separated in the model. In Fig. 7.6 on the following page the spectral intensity of radiation in the THz range is plotted as a function of the bunch current.

(a)  $\alpha_{c2} = 2.72 \times 10^{-4}, \tau_0 = 9 \text{ ms}$ (b)  $\alpha_{c2} = 2.72 \times 10^{-4}, \tau_2 = 11 \text{ ms}$ (c)  $\alpha_{c0} = 3.30 \times 10^{-4}, \tau_0 = 9 \text{ ms}$ (d)  $\alpha_{c0} = 3.30 \times 10^{-4}, \tau_2 = 11 \text{ ms}$ **Figure 7.6.: Effect of changed  $\alpha_c$  vs. effect of damping time change.**

Inovesa simulations with changed  $\alpha_c$  (rows) and with changed damping time  $\tau$  (columns).

$\tau_0 = 9 \text{ ms}$  stands for the damping time at 0 T wiggler field and  $\tau_2 = 11 \text{ ms}$  for the one at 2 T field.

Here  $\alpha_{c0} = 3.30 \times 10^{-4}$  stands for the linear momentum compaction factor at 0 T wiggler field and  $\alpha_{c2} = 2.72 \times 10^{-4}$  for that one at 2 T

field respectively. Different  $\alpha_c$  (top vs. bottom) have got very different spectra as can be seen in the comparison of the top to the bottom spectra. Accelerator optics changes can cause such changes of the  $\alpha_c$ . There is a frequency shift of the light/intense kink slightly below  $10^0 \text{ kHz}$  in the bottom plots. The top plots do not show such features for “low” frequencies in the first place. Theory predicts changes of low frequencies for different damping times (left vs. right). Damping wigglers change the damping time and thus might be responsible for the latter effects.

In the top row simulations with the damping time expected for 2 T wiggler field are shown and in the bottom row the ones for 0 T. On the left columns the damping times are unchanged and on the right side they are at the value for the 2 T wiggler's field. One can see the threshold current where the intensity is much higher than below this threshold. Also one can see dominant bursting frequencies at higher frequencies. These two effects depend on the accelerator settings, but not on the damping time, as [BCS10] showed. As  $\alpha_c$  integrates over the dispersion, it depends on the accelerator parameters. Furthermore one can see a band of strong intensity at frequencies below 1 kHz in the bottom row. These frequencies correspond to the outbursts in the THz radiation which repeats in a sawtooth-like manner. The sawtooth behaviour is described by [VW02] in more detail. As can be seen already here in plots 7.6c and 7.6d the frequency of this intensity band in the lower frequencies shifts.

To conclude the effects simulated by the Vlasov-Fokker-Planck solver, a change of  $\alpha_c$  causes changes in higher frequencies, and the current threshold. A change in the damping time on the other hand shifts the intensity band in the lower frequencies which will be discussed in the following subsection.

### **Experimental investigations of the Wiggler's influence on THz radiation spectrum**

In this section the experiments done to investigate the influence of the wiggler on the THz radiation spectrum will be discussed. The question if the wiggler can be used to further investigate the phenomena of the bursting of radiation in the THz regime was the key motivation. Especially the influence of the damping time can be addressed by different wiggler field strength. For this the THz radiation signal was measured by Miriam Brosi using a Schottky barrier diode, as described in more detail in [BGB<sup>+</sup>18, BSB<sup>+</sup>16, Bro20].

The optics were set-up as discussed before. Measurements had to be done during different accelerator fills, because one is interested in current-dependent effects and especially in the lower currents. Hence a reproducible initialization procedure for the optics was developed. As already mentioned ramping the wiggler's field to 2 T in one step would cause a beam loss. Therefore the wiggler's field was increased in small steps, each following by the correction of the transverse tunes using the simulations to match the previous values. This procedure was repeated until the wiggler was at its final field value of 2 T and all steps were saved to a routine to ramp the wiggler's field in parallel with the optics' compensation. This routine did not change the transverse tunes by operating and after ramping the wiggler's field reproducibly. Therefore it could be used for the intended experiments. For the actual measurement the tunes weren't measured, to maximize the span of the measurement of the THz radiation signal. The synchrotron tune was corrected only during the initial optics adjustment procedure, but not during the automated procedure, firstly, because the initial radio frequency is not always the same, because of orbit corrections during the set-up of the accelerator for each fill. Secondly, because one does not expect huge effects in the radiation frequency regime we are interested in. And lastly, because measuring the synchrotron tune

**Table 7.1.: Bunch current and frequency at instability threshold.** Measured bunch current and frequency at the instability threshold. Courtesy Miriam Brosi/Already published in [BGB<sup>+</sup>18].

Property	A (f06479)	B (f06534)	C (f06488)	D (f06483)	E (f06489)
$B_{\text{wig}} / \text{T}$	0	0	0 $\rightarrow$ 2	2	2
$I_{\text{th}} / \mu\text{A}$	$217 \pm 3$	$213 \pm 3$	$215 \pm 2$	-	$220 \pm 4$
$f_{\text{th}} / \text{kHz}$	$30.9 \pm 0.3$	$30.1 \pm 0.3$	$29.6 \pm 0.3$	-	$29.7 \pm 0.3$
$f_s / \text{kHz}$	7.90	7.70	7.50	7.50	7.50

at that point couldn't be done automatically with the fast-feedback system, because of other strong signals in that frequency range. In the end, this leads to slightly different synchrotron frequencies (7.50 kHz, 7.70 kHz, and 7.95 kHz) for different runs. These values are not taken from the fast feedback system but extracted from the radiated frequency spectrum procedure carried out by Miriam Brosi. Also the accelerator parameter-dependent threshold current  $I_{\text{th}}$  and frequency  $f_{\text{th}}$  listed in Table 7.1 are calculated by her based on the analysed spectrum. There are no values for  $I_{\text{th}}$  and  $f_{\text{th}}$  for fill D, because this fill did not reach the threshold current.

The reference fills without any wiggler field (A, B) were filled with two trains and different beam currents in each bucket. By this, one gets the radiation behaviour for different currents simultaneously and can speed up the measurements, see [BSB<sup>+</sup>16]. If there were multi-bunch effects interfering with the damping time dependent effects, this method would not be suitable, but until now, no evidence for the existence of such effects has been found. Anyway, to avoid any influences of preceding bunches the measurements have been carried out with three separated single bunches.

Of course, measuring during different fills may cause some minor changes of the accelerator settings e. g. caused by hysteresis or changes of the radio frequency during the beam energy ramp which caused later manual corrections of the synchrotron tune. To deal with this, one fill was used to start without the wiggler and turn it on during the fill. In total, besides the reference fills (A, B), two fills with the wiggler at 2 T (D, E) were done and one cross-check fill where the wiggler was ramped up during the measurement (C), such that the changes of the spectrum in this measurement definitely are caused by the wiggler.

### Orbit distortion

Another effect that can influence the measurement results is the orbit distortion. Since the optics is changed slightly by the wiggler and the compensation, the orbit might be disturbed. Indeed it is disturbed at some places in the ring, as can be seen in 7.7 where the measured orbit during the optics setup is depicted. Each cross represents one BPM at which the orbit position is measured and they are connected for visualization purposes only. In the horizontal plane—top plot—, one can see that the difference between the orbit at 0 T

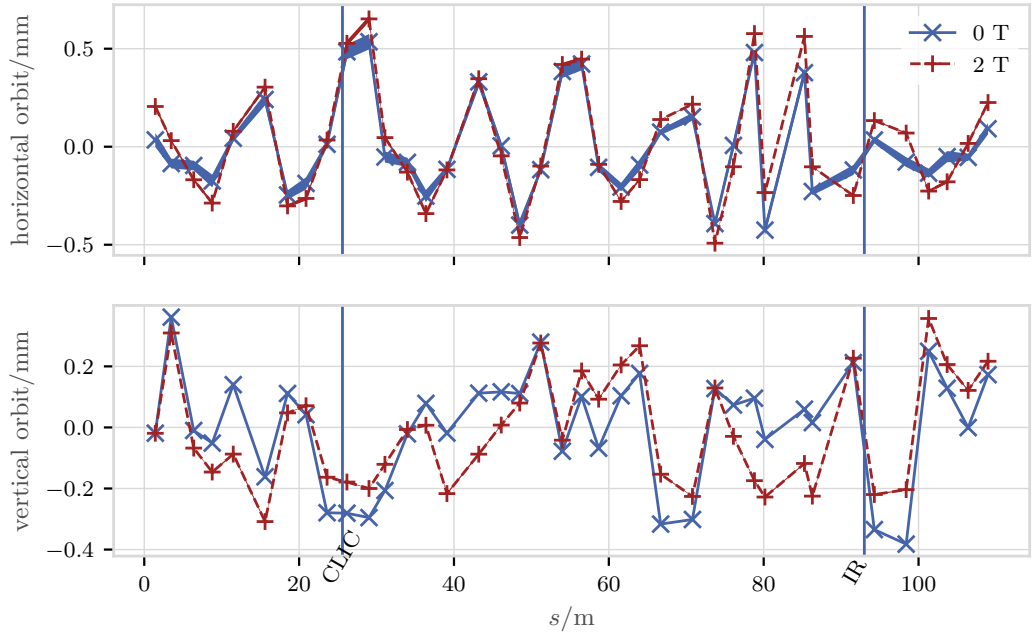


**Figure 7.7.: Orbit distortions with the wiggler.** The orbits for 0 T and 2 T are shown including their  $\pm 1\sigma$  error band on the BPM readout. The connections between the marker (BPMs) is for visualisation solely. The first line at 25.6 m indicates the position of the wiggler and the second line the position of the infrared (IR) beamline port where the THz radiation was measured. An orbit distortion at the IR beamline port could result in an shifted signal in the measurement and should therefore be small—same position of the blue and the red line at the IR line.

(solid green) and that at 2 T (dashed blue) is small. In the vertical plane—bottom plot—, where one might expect a small distortion there is a distortion of maximum 0.80 mm. The position of the wiggler, and that of the IR-beamline, where the THz-spectrum measurement takes place is marked by vertical lines. The orbit distortion at the THz-light port of the IR-beamline is less than 0.01 mm as can be seen in Fig. 7.7. An orbit change increases the total observed power of the spectrum, but does not shift the frequencies, as observed by [Hei13]. Here we are interested in a frequency shift which is not affected by the orbit shift.

### Discussion/Results

As already mentioned briefly the spectrum for the case with wiggler field and that one for no wiggler field look similar and the threshold currents are the same.

This is in good agreement with [BCS10]’s argument that the micro-bunching instability is a strong instability and therefore its threshold current should be independent of the longitudinal damping time. Also, the frequency of the fluctuations immediately above this threshold  $f_{th}$  is the same as shown in Table 7.1 on the preceding page.

In Fig. 7.8 on the following page the band of high intensity in the low frequencies is shown for the different cases. In comparison to Fig. 7.6 on page 86 and Fig. 7.9 on page 91 the axis are switched for visualization purposes and the current axis is not logarithmic, too.

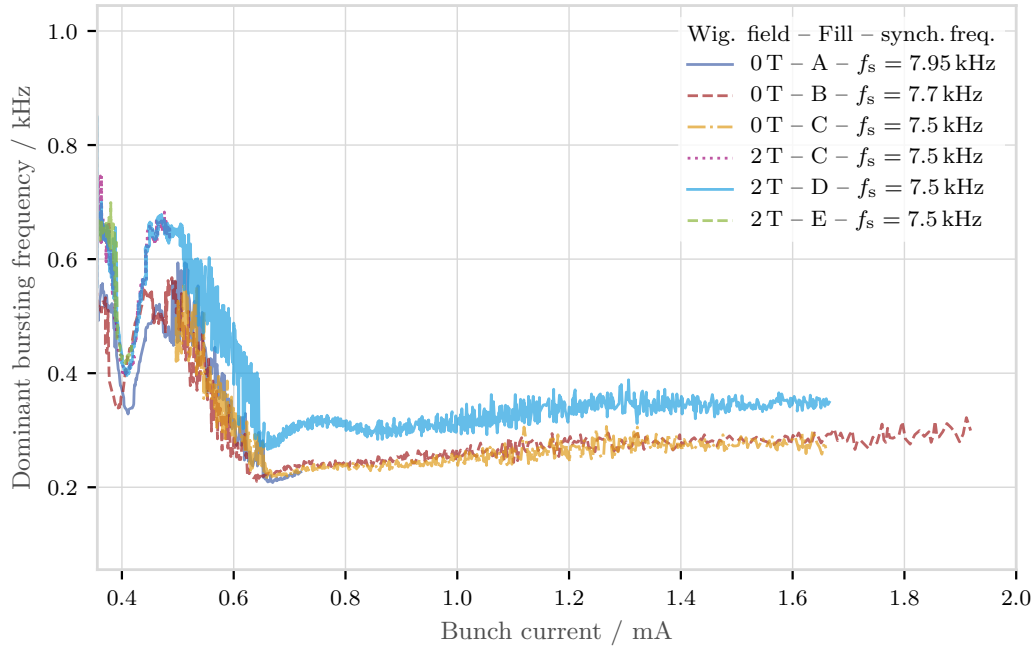


**Figure 7.8.: Dominant bursting frequency change caused by the CLIC damping wiggler.** The dominant bursting frequency of the coherent synchrotron radiation is plotted against the bunch current for different fills. The synchrotron frequency of was different at Fill 6479. The dominant bursting frequency is shifted when the wiggler was at 2 T. Courtesy M. Brosi.

The fills without wiggler field are shown in green, blue, and light blue whereas the ones with a wiggler field are shown in orange, red, and lilac. The shape of the curves with and without wiggler are very similar. This includes that the kinks at  $(0.65 \pm 0.01)$  mA and  $(0.40 \pm 0.01)$  mA are at the same positions. However, a change of the frequency of the occurrence of the fluctuations depending on the magnetic field of the wiggler is significant. The frequencies move up with wiggler field.

The damping time is the main effect as can be seen by comparing the shift of the low-frequency band in the simulations with the solution of the Vlasov-Fokker-Planck solver, see Fig. 7.6 on page 86, and shift in the measured spectra, see Fig. 7.8.

As already mentioned in the theory part the bursting occurs in saw-tooth like patterns. The shorter rise time of the bunch length depends on  $I_b$ . The shrinking of the bunch length depends on the minimum and maximum bunch length at a given  $I_b$  and also on the longitudinal damping time.

The current dependent frequency change is caused by the interaction of the longitudinal charge distribution and the impedance changes. This is not damping time-dependent, but may vary with current and thus can explain e. g. the kink at lower currents.

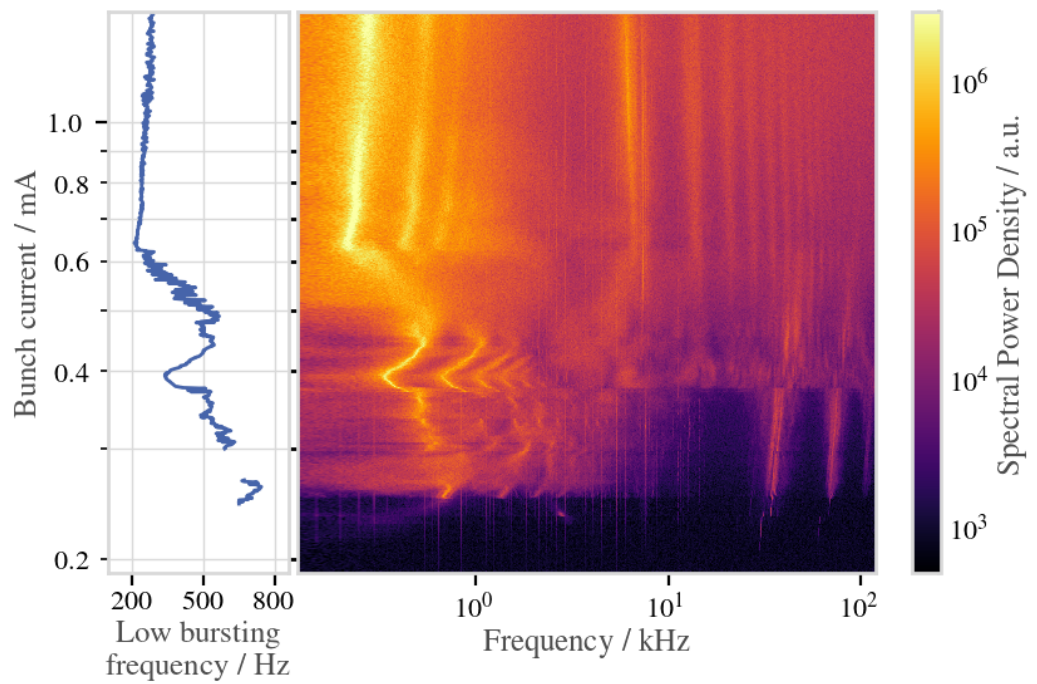


**Figure 7.9.: Measured THz bursting spectrum.** The right side of the plot shows the bursting frequency of the coherent synchrotron radiation depending on the bunch current and the frequency. The left side shows the low bursting frequency which has been extracted from the right side. This spectrum was taken at fill A. Courtesy M. Brosi.



## 8. Summary and outlook

A superconducting wiggler prototype with a novel cooling concept designed for the **Compact Linear Collider (CLIC)**'s damping rings and KIT's IMAGE beamline was characterised in the **KARlsruhe Research Accelerator (KARA)** storage ring and used to experimentally confirm the theoretically predicted influence of the damping time on the radiation spectrum of short bunches. For this, optics models of **KARA**'s low-energy short-bunch mode including the wiggler were developed. These successful tests encourage to proceed with exploiting damping effects of wigglers in large scales to reach ambitious luminosity goals of future high energy particle colliders, like in the **CLIC** damping rings.

For the next generation electron collider **CLIC**, about 200 high-field superconducting damping wigglers were proposed to be installed in two damping rings. A prototype of such a wiggler was built by the **Budker Institute of Nuclear Physics** and installed in **KARA** in 2016 for technology tests and beam dynamic studies. Tests and studies with it were part of this work. A second major aspect of this work was the question if the wiggler can be used to get further insights into the phenomena of the bursting of radiation in the THz regime. The demand for high brilliant light in this frequency range exists, but still the phenomena is not fully understood.

Experiments done with the wiggler prototype for the **CLIC** damping rings could confirm the maturity of the novel cooling system and showed the influence of the wiggler on the beam dynamics. Particularly, an unexpected behaviour was found in the transverse phase space, namely tune shifts in the horizontal plane, that may come from higher order multipoles of which an additional magnetic octupole component introduced by the wiggler was found, too. Furthermore, experiments were conducted with the wiggler in conditions with strong collective effects—coherent synchrotron radiation at **KARA**—, which could be important results for the **CERN**, but also for better understanding of the mechanisms of coherent synchrotron radiation. As the wiggler could be used to increase the damping time, synchrotron light measurements done by colleagues could, for the first time to our knowledge, confirm the theory of a shift of low frequencies in the THz-range of coherent synchrotron radiation.

For the experiments with the wiggler, optics models including the wiggler were developed. To differentiate effects caused by the wiggler from those of the accelerator both must be

understood. To operate the wiggler in the low-energy, short-bunch mode where certain measurements are not feasible this is essential, too. Though it sounds appealing, it is not advisable to scale a model based on first principles, e. g. because the magnets go into saturation, so two different models, one for the 2.50 GeV and one for the 1.30 GeV optics, had to be developed. Different existing transformation rules from magnet currents to quadrupole strength  $k$  were contrasted with tune measurements, resulting in boundary conditions of their validity. The transformation rules developed by M. Streichert can be used for relative changes only. Although **Linear Optics from Closed Orbits (LOCO)** fitted optics showed to be closer to measurements than the models with purely transformed strength, still they are not satisfying. Using the **LOCO** fits as start parameters for tune matching showed to result in satisfying optics models. They can be used with M. Streichert's transformation rules to match changes of the machine from the state where the **LOCO** fit was done. Though **LOCO** fits are more challenging for the 1.3 GeV operation mode, the same procedure could be applied for this operation mode. In that case a comparison of two **LOCO** fits and an extrapolation of the optics with the quadrupole transformation rules agreed within 20 % and 30 % concerning beta-beating of the horizontal and vertical plane for the long vs. short-bunch 1.3 GeV modes. As there are these relatively strong deviations from the reality, a dedicated model for the short-bunch mode had to be developed and was matched to measured tunes. It then could predict tune changes of quadrupole adjustments needed for the operation of the wiggler.

Besides the accelerator, the wiggler installed into it needs to be modelled, too. For this, different representations of the wiggler in the optics code *elegant* were evaluated. Different transformation procedures from sparse measured magnetic field data to a Fourier series representation which is required by the optics code were investigated. It turned out that the **CWIGGLER** implementation of an explicitly canonical integration can be used with differently transformed fields for the two evaluated high field wigglers **CATACT** wiggler and **CLIC** damping wiggler. An approach with an **FFT** and iteratively fitting of the  $y$ -component (F-N) turned out to be too sensitive for the case of the **CATACT** wiggler that was installed already at the beginning of this work. It was replaced by the F-4 approach to fit a Fourier representation of the field with boundary conditions to the existing field data. The robustness of the fits and the best number of free parameters was checked using optics simulations and the Fourier series representation with  $N = 4$  was selected. The implementation using generating functions for integration is fast but turned out to be too sensitive to multiple Fourier components even when used with artificially generated pure sinusoidal field data, using a FEM code. By experiments it could be shown that the combination of the **CWIGGLER** implementation and the F-4 field data can describe the reality the best for the **CATACT** and with the F-N for the **CLIC** damping wiggler. As the implementations describe the reality best with different input field data (F-N vs. F-4) for the different wigglers, one can also conclude that experimental tests are essential for wiggler simulations in storage rings as **KARA** and one cannot choose the best option from simulations only.

Experiments with the wiggler showed that heat load by synchrotron radiation seems not to be an issue for damping rings of future lepton colliders, like foreseen for linear colliders like the **CLIC** or the **ILC**. Another important figure of merit for these communities are beam dynamics, where our experiments showed expected tune shifts in the vertical plane, but also an additional tune shift in the horizontal plane. Either one has to include such effects in simulations or preferably develop mitigating strategies in the construction process of damping wigglers. Similarly, a chromaticity change could be observed which might be caused by the phase advance in the respective plane. Here also the horizontal chromaticity change can only occur due to the horizontal tune change. These measurements were also used as a benchmark for a new less perturbing chromaticity measurement technique under development at **CERN** and jointly tested at **KARA**. No hint on higher multipole components of the wiggler's field, beside an octupole component, were found. Octupole components of the wiggler's field were found using orbit bump measurements and **ADTS** measurements. Such additional octupole components caused beam lifetime decrease at **KARA** and further investigations conducted mainly by colleagues resulted in a change of the working point of **KARA**. The accuracy of the **ADTS** measurement was investigated and could be stated to be too inaccurate using **FFTs** and not satisfying the requirements set by measurements. Sufficient resolution can be reached using **NAFF** though. For the daily operation of the wiggler in **KARA**, the correct alignment of the wiggler is more important than the aforementioned measurement techniques. The correct alignment could be verified using orbit bumps to be within the alignment accuracy.

For the **CLIC** project, as well as for other next-generation colliders, this means that it is possible to operate a 51 mm period length Nb-Ti wiggler at a field of 2.9 T in the long term. However, one has to take care of higher multipole components and include them into simulations, too, in order to then specify the tolerances of the device correctly. When taking this into account, it should be possible to operate damping rings for linear electron-positron colliders or include damping wigglers in circular electron-positron colliders to increase the luminosity.

In addition, experiments in the short-bunch low- $\alpha$  mode were realised, which is very interesting for the synchrotron light-source community. The influence of the wiggler in the short-bunch mode on the beta-functions, dispersion and momentum compaction factor was simulated. With this model new optics with minimal vertical beta-beating caused by the wiggler were found which enabled the operation of the wiggler at higher fields. A procedure to increase the wiggler's field to 2 T in the low-energy, short-bunch mode was developed. It avoids beam losses caused by tune resonance crossings and that ends in the same transversal tunes and synchrotron tunes as with no wiggler field. Several measurements of the radiated synchrotron light were conducted together with Miriam Brosi, including one that features both cases of no wiggler field and 2 T wiggler field. Differences in the optics caused by the wiggler, such as a small distortions of the orbit or non-linear effects caused by the influence of the  $\alpha_c$  on the bucket shape, were discussed and could be excluded from causing the measured effects by simulating different scenarios. It could be observed that the wiggler

shifts the intense low frequencies to higher frequencies over the complete range of bunch current 0.40 mA to 1.90 mA. To our knowledge, these were the first measurements showing the theoretical predictions of [BCS10] for a shift of low frequencies with increased damping time.

It would be good to confirm the influence of the damping time on the frequencies with the wiggler also in the negative  $\alpha_c$  mode that is under development at KARA right now [SBB<sup>+</sup>19]. Nonetheless, the realisation might be even more challenging, because there KARA is operated at 0.50 GeV so the wiggler field might not exceed the not well compensated field strength. Another interesting idea to proceed with, would be the integration of the wiggler into the low- $\alpha$  mode for users of the THz radiation. Users of the low frequency THz radiation might want to shift the frequency to their needs by changing the wiggler's field and adjusting the optics correspondingly, based on the optics developed in this thesis.

# Appendix

## A. Parameter tables

### A.1. Measurements

In this section the parameters used for the short-bunch mode THz measurements described in chapter 7 are listed. Firstly, the measured machine settings with values simulated with the optics code *elegant* for the values not directly measured are listed in Table A.1 on the next page. Secondly, the input values for the Vlasov-Fokker-Planck solver Inovesa are listed in A.2.

Furthermore the fitted values for the orbit bump measurement—described in section 6.4.1 of chapter 6—are listed in Table A.3 on page 100.

**Table A.1.: Storage ring settings during main measurement campaign.** Fills 6479, 6483, 6488. These settings were used during the measurements of chapter 7.

Parameter	Value	Unit
RF	499.73	MHz
RF-voltage	772170.00	V
Horizontal tune	$0.7863 \pm 0.0001$	
Vertical tune	$0.7992 \pm 0.0001$	
0 T		
$\alpha_0$	$3.30 \times 10^{-4}$	-
$\alpha_1$	$-2.45 \times 10^{-2}$	-
$\tau$	0.01	s
2 T		
$\alpha_0$	$2.72 \times 10^{-4}$	-
$\alpha_1$	$-4.18 \times 10^{-1}$	-
$\tau$	0.01	s
$f_s$		kHz

**Table A.2.: Inovesa settings.** Settings of the Inovesa Vlasov-Fokker-Planck solver. The exact version of it is Inovesa v0.15 alpha, Branch: makepkg, Commit: f23a362616a425756fc236f4d3871c9284ff81c9. The bunch current was adjusted accordingly and the  $\alpha_0$ ,  $\alpha_1$ , and  $DampingTime$  were chosen to match the respective case shown in Fig. 7.6 on page 86.

AcceleratingVoltage	$771 \times 10^3$
BeamEnergy	$1.30 \times 10^9$
BeamEnergySpread	0.00
BendingRadius	5.56
BunchCurrent	\$CURRENT
CollimatorRadius	0
CutoffFreq	$2.30 \times 10^{10}$
DampingTime	0.01
ForceOpenGLVersion	2
GridSize	256
HarmonicNumber	184
InitialDistStep	-1
InitialDistZoom	1
InterpolateClamped	0
InterpolationPoints	4
PhaseSpaceShiftX	0
PhaseSpaceShiftY	0
PhaseSpaceSize	12
RenormalizeCharge	0
RevolutionFrequency	$2.70 \times 10^6$
RotationType	2
RoundPadding	1
SavePhaseSpace	0
SaveSourceMap	0
SyncFreq	7500
UseCSR	1
VacuumGap	0.03
WallConductivity	0
WallSusceptibility	0
alpha0	0.00
alpha1	0
alpha2	0
cldev	0
derivation	4
gui	0
outstep	100
padding	8
rotations	1500
steps	1000
tracking	
verbose	0

**Table A.3.: Octupole component fits.** Quadratic fits of the tunes of the respective plane (Tune) to the bump planes (Bump) and the wiggler field (Wiggler field/T) and its “hysteresis” (history). The fits include the mean-squared-error (MSE) and the offset from the origin (null). The history flag indicates if the bumping magnets were used before and might show hysteresis effects or if the very measurement was done with a new fill after demagnetizing the corrector magnets.

Plane		Wiggler field/T	history	Fit
Bump	Tune			
y	x	2.90	yes	$0.7755 + 0.0008894x + 0.0001312x^2$ MSE: 0.00 null: $-3.20$ mm
y	x	2.90	yes	$0.781 + 0.0008059x + 6.707e - 5x^2$ MSE: 0.00 null: $-6$ mm
y-angle	y	2.90	yes	$0.713 + 0x + 0.0006x^2$ MSE: $2.24 \times 10^{-5}$ null: 0 mm
y	x	2.90	yes	$0.776816 + 0.000195207x + 0.000229116x^2$ MSE: 0.00 null: 0 mm
y	y	2.90	yes	$0.70988 - 3.24145e - 5x + 0.00010581x^2$ MSE: 0.00 null: 0 mm
x +(3mm y)	x	2.90	yes	$0.778424 + 0.000601597x + 0.000404476x^2$ MSE: $8.60 \times 10^{-17}$ null: 0 mm
x +(3mm y)	y	2.90	yes	$0.710102 - 0.00028217x + 0.000442435x^2$ MSE: $2.02 \times 10^{-16}$ null: 0 mm
y	y	0	no	$\Delta = (-2e - 5 \pm 1.8e - 5)x^2 + (-6.7e - 5 \pm 3.4e - 5)x + (-7.53e - 28 \pm 1e - 12)$
y	x	0	no	$\Delta = (4.30e - 05 \pm 2.15e - 06)x^2 + (0.0001123 \pm 5e - 6)x + (-3e - 26 \pm 10e - 12)$
x	x	0	no	$\Delta = 0.00014 \pm 4e - 6)x^2 + (-0.00023 \pm 6.2e - 6)x$
x	y	0	no	$\Delta = (7.1e - 5 \pm 5.1e - 5)x^2 + (0.00057 \pm 0.00013)x$
y	y	0	no	$\Delta = (-1.3e - 05 \pm 7.6e - 05)y^2 + (-7e - 05 \mp 0.00013)y + (-3e - 05 \pm 0.00042)$
y	y	2.90	no	$\Delta = (0.0016 \pm 0.0008)y^2 + (-0.0001 \mp 0.00068)y + (7.2e - 05 \pm 0.00037)$

## B. Derivations

In this section some detailed derivation of equations used throughout this thesis are shown.

### B.1. Rigidity

The rigidity  $B\rho = p/e$  and various forms of the relation are used very often, therefore it is derived here for completeness.

The magnetic component of the Lorentz force (as scalar values due to the perpendicularity of the electron motion and the magnetic field) on the one side is counter acted by the centripetal force.

$$F_L = evB \quad (\text{B.1})$$

$$F_C = m_0 \frac{v^2}{\rho} \quad (\text{B.2})$$

$$B.1 = B.2$$

$$(\text{B.3})$$

$$\begin{aligned} evB &= m_0 \frac{v^2}{\rho} \\ eB &= m_0 \frac{v}{\rho} \\ B\rho &= m_0 v / e \\ &= \frac{p}{e} \end{aligned} \quad (\text{B.4})$$

### B.2. Further comments on phase space and trace space

As was mentioned in the theory chapter 2 many optics codes, like *elegant* do not use the phase space of the particles, but use the trace space. With the definition of the momentum in one plane  $u$

$$p_u = m_0 v_u \gamma,$$

the relation between the phase space coordinates and momenta and the trace space coordinates and momenta is the following:

$$\begin{aligned} u' &= \frac{du}{ds} = \frac{du}{dt} \frac{dt}{ds} = v_u \frac{dt}{ds} \\ &= \frac{p_u}{\gamma m_0} \frac{dt}{ds} = \frac{p_u}{p_s} \end{aligned}$$

### B.3. Orbit bump correctors

The following corrector magnets have been used for the local orbit bumps around the CLIC damping wiggler.

- MCV\_S1.03, MCV\_S1.04, MCV\_S2.01, MCV\_S2.02, and
- MCH\_S1.06, MCH\_S1.08, MCH\_S2.01, MCH\_S2.03.

The names used internally by the machine’s control system and in variations in the measurement database stand for “magnet”, “corrector”, “vertical” or “horizontal”, then followed by the sector and then by the number of the specific corrector within that sector.

#### B.4. Dispersion variation

The wiggler’s bending radius is

$$\rho_w = \frac{B\rho}{B_w} = 1.50 \text{ T} \cdot 5.559 \text{ m}/2 \text{ T} = 4.17 \text{ m}.$$

With this, one can approximate the contribution to the dispersion as

$$|\eta_0| = \frac{1}{\rho_w k_w^2} = \frac{1}{4.17 \text{ m} \left(\frac{2\pi}{0.054 \text{ m}}\right)^2} = 1.60 \times 10^{-5} \text{ m}.$$

#### B.5. Field integral measurements

The first and second field integrals, see Section 2.1.6.1 on page 18, have been measured by BINP using the stretched wire method. This is described in [MVS<sup>+</sup>16] and adapted for this section. On the stretched wire a current was applied and the horizontal deviation of the wire’s position before ( $\Delta x_1$ ) and after ( $\Delta x_2$ ) the wiggler with a distance of  $L = 2.5 \text{ m}$  between the two measurement points was measured.

$$I = \frac{T}{I} \left( \frac{\Delta x_1}{L_1} + \frac{\Delta x_2}{L_2} \right) \quad (\text{B.5})$$

$$II = \frac{T}{I} \left( \Delta x_2 \left( 1 + \frac{L}{2L_2} \right) - \Delta x_1 \left( 1 + \frac{L}{2L_1} \right) \right) \quad (\text{B.6})$$

provide the first and second field integrals where  $T = 42 \text{ N}$  is the tension of the stretched wire and  $L_1 = L_2 = 1 \text{ m}$  are the distances between the measurement points of  $\Delta x_{1,2}$  and the fixation points of the wire.

#### B.6. Further field components

As discussed by [KB90], skewed octupole or sextupole components would reflect in dependencies of the tune on an orbit shift in the  $xy$  plane. In B.1 no dependence of the tune on orbit bumps in the x-y plane are visible.

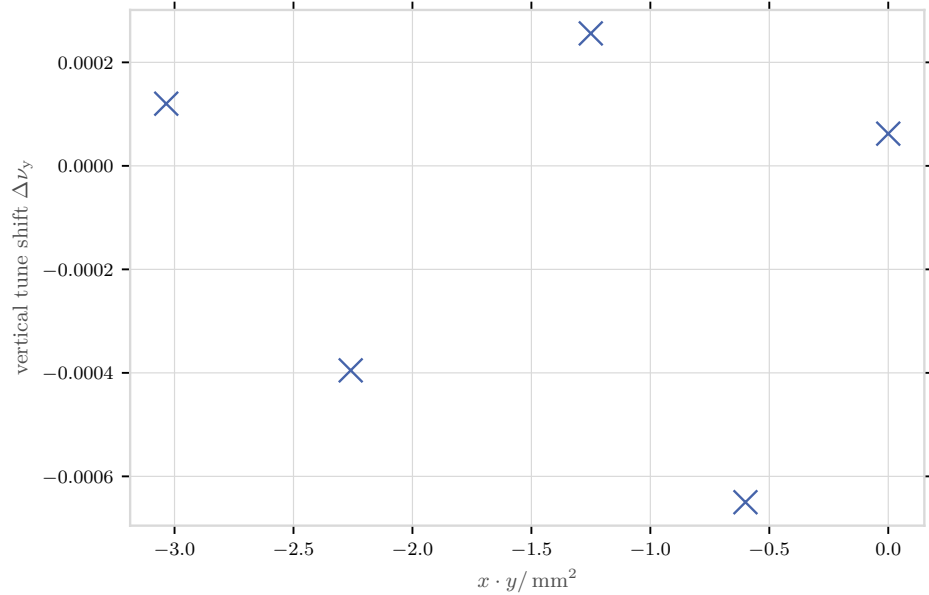


**Figure B.1.: Tune shift with  $xy$  bump.** Tune shift (y-axis) vs. orbit bump (x-axis) in the x-y-plane. A linear effect of the tune depending on a shift by  $xy$  would give a hint on a skewed octupole component cf. [KB90]

## B.7. Field representations

In the following listings of the input files for *elegant* for the different field representations are shown.

### F-0 field representation

This is the simplest case of a pure sinusoidal field, represented by only one Fourier component with the amplitude  $C_{mn} = 1$  and only in the vertical plane  $K_y \text{Over} K_w$ .

```

1 SDDS1
  &description text="Harmonic analysis of wiggler field", &end
3 &column name=Cmn, units=none, description="Relative Amplitude", type=double, &end
  &column name=Phase, units=none, description="Phase", type=double, &end
5 &column name=KxOverKw, units=none, description="Normalized hor. wave number", type
  =double, &end
  &column name=KyOverKw, units=none, description="Normalized ver. wave number", type
  =double, &end
7 &column name=KzOverKw, units=none, description="Normalized long. wave number",
  type=double, &end
  &column name=zHarm, units=none, description="Long. harmonic number", type=double,
  &end
9 &column name=xHarm, units=none, description="Hor. harmonic number", type=double,
  &end
  &data mode=ascii &end
11 1
    1.0  0.0  0.0  1.0  1.0  1.0  1.0

```

### F-4 field representation

The F-4 representation with four Fourier component values.

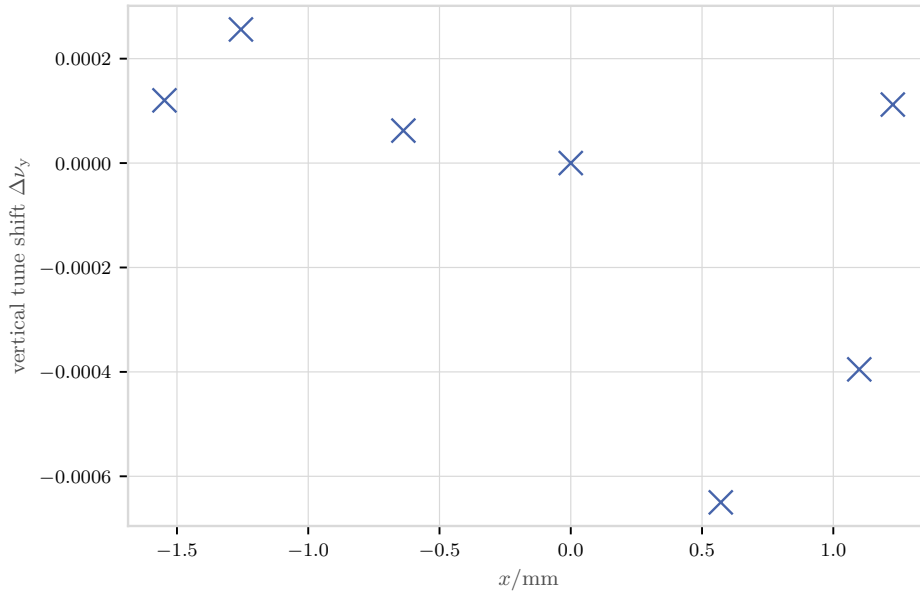


**Figure B.2.: Vertical tune shift with horizontal bump.** Vertical tune shift (y-axis) vs. horizontal orbit bump (x-axis), so effects on the other plane are shown. Since there seems to be no linear effect of the vertical tune depending on a horizontal orbit shift there is not an indication for a sextupole component cf. [KB90]

```

1 SDDS1
  &description text=text, contents="Fourier series of a wiggler short model
    simulation field.                                     Generated on 2016-04-01
    13:14:21.031157", &end
3 &parameter name=Kw, type=double, &end
  &column name=Cmm, type=double, &end
5 &column name=KxOverKw, type=double, &end
  &column name=KyOverKw, type=double, &end
7 &column name=KzOverKw, type=double, &end
  &column name=zHarm, type=double, &end
9 &column name=xHarm, type=double, &end
  &column name=Phase, type=double, &end
11 &data mode=ascii, &end
  ! page number 1
13 1.222409592836495e+02
    10
15 1.008360222780846e+00 8.453783284191002e-03 1.000035732587499e+00
    1.000000000000000e+00 1.000000000000000e+00 1.000000000000000e+00
    0.000000000000000e+00
    -6.219643434312879e-06 8.453783284191002e-03 2.000017866533151e+00
    2.000000000000000e+00 2.000000000000000e+00 1.000000000000000e+00
    0.000000000000000e+00
17 7.925664210451877e-05 3.071640465190009e+00 3.665375171437802e+00
    2.000000000000000e+00 2.000000000000000e+00 2.000000000000000e+00
    0.000000000000000e+00
    7.515266178878295e-03 8.453783284191002e-03 3.000011911051657e+00
    3.000000000000000e+00 3.000000000000000e+00 1.000000000000000e+00
    0.000000000000000e+00
19 -5.101022140382642e-05 3.071640465190009e+00 4.293596994059024e+00
    3.000000000000000e+00 3.000000000000000e+00 2.000000000000000e+00
    0.000000000000000e+00

```

```

5.665457806035423e-04  3.321130870558429e+00  4.475478774318585e+00
3.000000000000000e+00  3.000000000000000e+00  3.000000000000000e+00
0.000000000000000e+00
21 -1.615053000298672e-04  8.453783284191002e-03  4.000008933296502e+00
4.000000000000000e+00  4.000000000000000e+00  1.000000000000000e+00
0.000000000000000e+00
-1.808325948989349e-04  3.071640465190009e+00  5.043309939652003e+00
4.000000000000000e+00  4.000000000000000e+00  2.000000000000000e+00
0.000000000000000e+00
23 -1.075965057266321e-04  3.321130870558429e+00  5.199029742113059e+00
4.000000000000000e+00  4.000000000000000e+00  3.000000000000000e+00
0.000000000000000e+00
-1.174843566623134e-04  8.901231599162805e-03  4.000009903978237e+00
4.000000000000000e+00  4.000000000000000e+00  4.000000000000000e+00
0.000000000000000e+00

```

### Derivation of the ADTS

Starting with the emittance dependent tune change from [Smi86] (Eq. (2.25) on page 21)

$$\Delta\nu_u = \frac{1}{16\pi} \frac{k_u^4}{k_z^2 \rho^2} L \beta^{*2} \left[ 1 + \frac{2}{3} \left( \frac{L}{2\beta^*} \right)^2 + \frac{1}{5} \left( \frac{L}{2\beta^*} \right)^4 \right] \varepsilon_x$$

For a wiggler with wide enough poles we can assume  $k_u = k_z$ . Furthermore we ignore everything except for the first order.

(B.7)

$$\approx \frac{1}{16\pi} \frac{k_z^2}{\rho^2} L \varepsilon_x \beta^{*2} = \frac{1}{16\pi} \frac{4\pi^2}{\lambda_w^2 \rho^2} L \varepsilon_x \beta^{*2}$$

and use the common rigidity relation  $p = \rho B e$  with  $B$  and  $\rho$  from the wiggler of course

$$= \frac{\pi}{4} \frac{L}{\lambda_w^2} \beta^{*2} \frac{B^2 e^2}{p^2} \varepsilon_x = \frac{\pi}{4} \frac{L}{\lambda_w^2} \beta^* \frac{e^2 B^2}{p^2} \beta^* \varepsilon_x$$

and the relation between the emittance and the beam size  $\varepsilon_x = \sigma^2 / \beta$  where we also replace  $\beta^* = \beta$

$$= \frac{\pi}{4} \frac{L}{\lambda_w^2} \beta \frac{B^2 e^2}{p^2} \sigma^2$$

Finally we replace  $\sigma$  by  $u$  to look at a single particle instead of a particle distribution

$$\Rightarrow \frac{\Delta\nu_u}{\sigma_u^2} \doteq \frac{\Delta\nu_u}{u^2} = \frac{\pi}{4} \frac{L}{\lambda_w^2} \beta \frac{e^2 B^2}{p^2}.$$

That is the form which is also used in [Saf89] and Eq. (2.26) on page 21.

### Derivation of the octupole component

Starting with the well known relation  $1/\rho = \frac{e}{p} B_y$  we can derive  $B_x(y)$  at  $y = 0$  to get

$$\begin{aligned} \frac{e}{p} B_x(y) &= \frac{e}{p} \frac{dB_x}{dy} y + \frac{1}{2!} \frac{e}{p} \frac{d^2 B_x}{dy^2} y^2 + \frac{1}{3!} \frac{e}{p} \frac{d^3 B_x}{dy^3} y^3 + \dots \\ &= \frac{1}{\rho} + ky + \frac{1}{2!} my^2 + \frac{1}{3!} oy^3 + \dots \end{aligned}$$

Here we identify  $\frac{1}{6} oy^3 = Oy^3$  as the octupole with  $O = \frac{1}{6} \frac{e}{p} \frac{d^3 B_x}{dy^3}$ .

Inserting the equivalent octupole strength [Wal83]  $B_x = B_3 y^3$  with  $B_3 = \frac{e}{\gamma m_0 c} \frac{B_0^2}{3} k_z^2$  into the octupole component  $O$  leads to the equivalent octupole component of the wiggler:

$$\begin{aligned} O &= \frac{1}{6} \frac{e}{p} \frac{d}{dy^3} \frac{e}{\gamma m_0 c} \frac{B_0^2}{3} k_z^2 y^3 \\ &= \frac{1}{18} \left( \frac{e}{p\beta} \right)^2 \frac{B_0^2}{3} k_z^2 \frac{d}{dy^3} y^3 \\ &= \frac{1}{3} \left( \frac{e}{p\beta} \right)^2 B_0^2 k_z^2 \\ &= \frac{1}{3} \frac{k_z^2}{\rho^2} \beta^2 \end{aligned}$$

setting  $\beta = 1$  for the ultra relativistic case yields

$$= \frac{1}{3} \frac{k_z^2}{\rho^2}$$

which is exactly the third-order term of the expansion of the equation of motion inside of a wiggler, so that one speaks of pseudo-octupole or octupole component of the wiggler.

**List of Symbols**

$\alpha_u$  proportional to the first derivative of the betatron function. 7

$\rho$  Bending radius. 6, 12, 15, 18, 20, 21, 25, 81, 101, 102, 105, 106

$\beta_u$  betatron function of the horizontal ( $u := x$ ) plane or the vertical ( $u := y$ ) plane. 7, 8, 10–12, 19, 21, 56, 60, 61, 69, 70, 73, 74, 82, 105

$\beta$  velocity over the speed of light  $c$ . 6, 9, 14, 19, 106

$\xi_u$  first-order chromaticity of the respective plane  $u$ . 28

$C$  Circumference of the ring. In the case of **KARA** it is  $C = 110.40$  m. 8, 12, 14, 25, 107

**Courant-Snyder invariant** Courant-Snyder invariant. 7, 8

**CSR** Coherent synchrotron radiation. 16

$I_b$  Bunch current, typically in mA. 15, 90

$\delta$  Momentum deviation of a particle  $p$  and the reference particle  $p_0$   $\delta = \frac{p-p_0}{p_0}$ . 11, 12, 14

$\eta$  Dispersion. 12, 18

$e$  Elementary charge. 6, 9, 14, 17–19, 21, 60, 68, 101, 105, 106

$\varepsilon$  emittance of the horizontal ( $u := x$ ) or vertical ( $u := y$ ) plain. 7, 8, 21, 105

$E$  Beam energy, typically in eV. 6, 9, 17, 25

$k$  Focussing strength. 68

$\gamma$  relativistic Lorentz factor. 12, 18, 19, 60, 68, 101, 106

$\gamma_u$  gamma Twiss function. 7

$h$  harmonic number. 9, 14

**Hill's equation** Equation of conservative motion of a particle moving in an accelerator. 7

$K$  Undulator or deflection parameter  $K$ . 19

$\eta_c$  momentum compaction. 12–14

$\alpha_c$  momentum compaction factor. 12–14, 18, 27, 28, 84–86, 95, 96

**Optical functions** See Twiss parameter. 7

$\lambda_w$  Period length of the wiggler. 17, 19, 21, 25, 26, 36, 37, 68, 105, 108

$\omega_{RF}$  Circular radio frequency. 9, 14

$m_0$  rest mass of the electron. 17–19, 60, 68, 101, 106

$c$  speed of light. 6, 9, 14, 17–19, 60, 68, 107

**synchrotron oscillation** synchrotron oscillation. 11, 12

**fractional tune** fractional tune. 8, 9

$\nu_u$  Tune or fractional tune of the respective plane  $u$ . 8, 9, 12, 19, 21, 27, 28, 45, 47, 60–62, 71, 105

**tune** tune. 8

**stopband** band around a tune resonance line that is already instable. 9, 21

**Twiss parameter** Twiss parameter. 7

$k_u$  Wave number of the  $u$  plane of the wiggler;  $k_z = \frac{2\pi}{\lambda_w}$ . 19, 21, 37, 38, 61, 68, 105, 106

## List of Acronyms

**ADTS** amplitude-dependent tune shift, also-called detuning with amplitude. iv, 21, 27, 62, 68, 69, 71, 72, 74, 75, 79, 80, 95, 105

**AT** Matlab Accelerator Toolbox [Ter01]. 35

**BINP** Budker Institute of Nuclear Physics. 25, 61, 63, 93, 102

**BPM** Beam Position Monitor. 9, 27, 29–33, 53, 71, 73, 74, 88, 89

**CATACT** CATalysis and ACTinide. 23–26, 36–38, 42, 45, 46, 48, 49, 80, 94

**CERN** Conseil Européen pour la Recherche Nucléaire. 3, 26, 35, 60, 66, 93, 95

**CLIC** Compact LInear Collider. 3, 5, 16, 23, 24, 26, 29, 30, 36, 38, 39, 42, 45–49, 60, 63, 66, 80, 85, 90, 93–95, 101

**FFT** Fast Fourier Transformation. 9, 35, 37, 71, 72, 74, 94, 95

**ID** Insertion Device. 16, 18, 19, 23, 24, 30, 63

**KARA** KARlsruhe Research Accelerator. iii, 1–3, 5, 10, 12, 16, 23–25, 27, 28, 30, 31, 33, 35, 37, 39, 41, 43–45, 47, 49, 51, 53, 55–57, 60, 67, 72, 80, 82–85, 93–96, 107

**KIT** Karlsruhe Institute of Technology. 60

**LOCO** Linear Optics from Closed Orbits. 27, 32, 33, 35, 51–57, 94

**NAFF** Numerical Analysis of Fundamental Frequencies. 72–74, 95

**ORM** Orbit Response Matrix. 32, 33, 35, 53, 56

**RF** radio frequency. 12

**SVD** Singular Value Decomposition. 73



## Bibliography

- [ANK14] ANKA - Synchrotron Radiation Facility: *ANKA User Reports 2012/2013*. Technical report, Karlsruher Institut für Technologie (KIT), 2014. <https://doi.org/10.5445/IR/1000044101>.
- [BBC<sup>+</sup>16] Axel Bernhard, A. Bragin, S. Casalbuoni, P. Ferracin, L. Garcia Fajardo, S. Gerstl, Julian Gethmann, A. Grau, E. Huttel, S. Khrushchev, N. Mezentsev, A.-S. Müller, Y. Papaphilippou, D. de Jauregui, H. Schmickler, D. Schoerling, V. Shkaruba, N. Smale, V. Tsukanov, P. Zisopoulos, and K. Zolotarev: *A CLIC Damping Wiggler Prototype at ANKA: Commissioning and Preparations for a Beam Dynamics Experimental Program*. In *Proceedings of the 7th International Particle Accelerator Conference (IPAC 2016)*, number CERN-ACC-2016-222, pages 2412–2415, Busan, Korea, 2016. <https://doi.org/10.18429/JACoW-IPAC2016-WEPMW002>.
- [BCS10] Karl L.F. Bane, Y. Cai, and G. Stupakov: *Threshold studies of the microwave instability in electron storage rings*. *Physical Review Special Topics - Accelerators and Beams*, 13(10):104402, oct 2010. <https://link.aps.org/doi/10.1103/PhysRevSTAB.13.104402>.
- [Ber18] Axel Bernhard: *Vorlesung: Beschleunigerphysik II: Synchrotronstrahlungsquellen*. 2018.
- [BGB<sup>+</sup>18] Miriam Brosi, Julian Gethmann, A. Bernhard, B. Kehrer, A. Papash, P. Schönfeldt, P. Schreiber, J.L. Steinmann, and A.-S. Müller: *Studies of the Micro-Bunching Instability in the Presence of a Damping Wiggler*. *Journal of Physics: Conference Series*, 1067(6), 2018. <https://doi.org/10.1088/1742-6596/1067/6/062017>.
- [Bor] Michael Borland: *User’s Manual for Elegant Program Version 25.1.0*. 25.1.0 edition.
- [Bor00] Michael Borland: *ELEGANT: A flexible SDDS-compliant code for accelerator simulation*. Technical report, 2000.
- [Bra09] Daniel Brandt: *CAS — CERN Accelerator School: Course on Beam Diagnostics*. CERN Accelerator School. CERN, 2009. <https://doi.org/10.5170/CERN-2009-005>.

- [Bro20] Miriam Brosi: *In-Depth Analysis of the Micro-Bunching Characteristics in Single and Multi-Bunch Operation at KARA*. Dissertation, Karlsruher Institut für Technologie, 2020. <https://doi.org/10.5445/IR/1000120018>.
- [BSB<sup>+</sup>16] Miriam Brosi, J.L. Steinmann, E. Blomley, E. Bründermann, M. Caselle, N. Hiller, B. Kehrer, Y. L. Mathis, M.J. Nasse, L. Rota, M. Schedler, P. Schönfeldt, M. Schuh, M. Schwarz, M. Weber, and A.-S. Müller: *Fast mapping of terahertz bursting thresholds and characteristics at synchrotron light sources*. *Physical Review Accelerators and Beams*, 19(11):110701, nov 2016. <https://link.aps.org/doi/10.1103/PhysRevAccelBeams.19.110701>.
- [But09] Tilman Butz: *Fouriertransformation für Fußgänger*. Vieweg+Teubner, Wiesbaden, 2009, ISBN 978-3-8348-0538-6. <http://link.springer.com/10.1007/978-3-8348-9609-4>.
- [BW11] Johannes Bahrdt and Godehard Wüstefeld: *Symplectic tracking and compensation of dynamic field integrals in complex undulator structures*. *Physical Review Special Topics - Accelerators and Beams*, 14(4):040703, 2011. <http://link.aps.org/doi/10.1103/PhysRevSTAB.14.040703>.
- [Cha16] Cheng Chang: *Precise Determination of the Electron Beam Energy with Compton Backscattered Laser Photons at ANKA*. Dissertation, Karlsruher Institut für Technologie, 2016. <http://doi.org/10.5445/IR/1000051914>.
- [Cla04] James A. Clarke: *The Science and Technology of Undulators and Wigglers*. Oxford University Press, 2004, ISBN 978-0-1985-0855-7. <https://doi.org/10.1093/acprof:oso/9780198508557.001.0001>.
- [CMTZ13] Alexander W. Chao, Karl H. Mess, Maury Tigner, and Frank Zimmermann: *Handbook of accelerator physics and engineering, second edition*. World Scientific, 3. edition, 2013, ISBN 978-9-8144-1585-9. <https://doi.org/10.1142/8543>.
- [Dim20] Dimtel: *Dimtel iGp12 website*, 2020. <https://www.dimtel.com/products/igp12>.
- [Efr79] Bradley Efron: *Bootstrap Methods: Another Look at the Jackknife*. *Ann. Statist.*, 7(1):1–26, 1979. <https://doi.org/10.1214/aos/1176344552>.
- [EKP98] Dieter Einfeld, A. Krussel, and M. Pont: *Magnet Prototype for ANKA (unpublished)*. 1998.
- [EKP99] Dieter Einfeld, A. Krussel, and M. Pont: *Magnetic Measurements of the ANKA Storage Ring Magnets*. In *Proceedings of the 1999 Particle Accelerator Conference (Cat. No.99CH36366)*, volume 5, pages 3375–3377, 1999.
- [et.20] P.A. Zyla et.al.: *Review of Particle Physics*. *PTEP*, 2020(8):083C01, 2020. <https://doi.org/10.1093/ptep/ptaa104>.

- [Eur20] European Strategy for Particle Physics Preparatory Group: *2020 UPDATE OF THE EUROPEAN STRATEGY by the European Strategy Group*. Technical report, CERN, Geneva, Switzerland, 2020. <https://europeanstrategy.cern/european-strategy-for-particle-physics>.
- [FB81] Martin A. Fischler and R.C. Bolles: *Random sample consensus: a paradigm for model fitting with applications to image analysis and automated cartography*. Communications of the ACM, 24(6):381–395, jun 1981. <http://doi.acm.org/10.1145/358669.358692>.
- [FEW<sup>+</sup>03] Laurent Farvacque, Pascal Elleaume, Richard F Walker, Joel Chavanne, Hideo Onuki, Shigemi Sasaki, Marie Emmanuelle Couprie, Sochi Wakatsuki, W. R. Dix, Toru Yamada, Kazutoshi YaGi-Watanabe, Tsuneaki Miyahara, Wah Keat Lee, Patricia Fernandez, Dennis M Mills, and Terubumi Saito: *Undulators, Wigglers and Their Applications*. Taylor & Francis, 2003, ISBN 0-415-28040-0.
- [Flo03] Klaus Floettmann: *Some basic features of the beam emittance*. Physical Review Special Topics - Accelerators and Beams, 6(3):034202, mar 2003. <https://link.aps.org/doi/10.1103/PhysRevSTAB.6.034202>.
- [GBB<sup>+</sup>17] Julian Gethmann, A. Bernhard, E. Blomley, E. Huttel, A.-S. Müller, Y. Papaphilippou, A. Papash, M. Schedler, P. Zisopoulos, and K. Zolotarev: *Non-Linear Beam Dynamics Studies of the CLIC Damping Wiggler Prototype*. In *Proceedings of the 8th International Particle Accelerator Conference (IPAC 2017): Copenhagen, Denmark, May 14-19, 2017*, pages 3087–3090, 2017. <https://doi.org/10.18429/JACoW-IPAC2017-WEPIK068>.
- [Get14] Julian Gethmann: *Studien Zu Optiken Mit Insertion Devices Am ANKA-Speicherring*, 2014.
- [Hal81] Klaus Halbach: *Physical and optical properties of rare earth cobalt magnets*. Nuclear Instruments and Methods in Physics Research, 187(1):109–117, aug 1981. [https://doi.org/10.1016/0029-554X\(81\)90477-8](https://doi.org/10.1016/0029-554X(81)90477-8).
- [Hei13] Jan Christoph Heip: *Design and Characterisation of THz Beam Transport Systems*. Dissertation, Karlsruhe Institute of Technology, 2013.
- [HHH<sup>+</sup>14] Edmund Hertle, N. Hiller, E. Huttel, B. Kehrer, A.-S. Müller, and N.J. Smale: *First Results of the New Bunch-by-bunch Feedback System at ANKA*. In *Proceedings of the 5th International Particle Accelerator Conference (IPAC'14)*, pages 1739–1741, Dresden, Germany, jul 2014. JACoW Publishing. <https://doi.org/10.18429/JACoW-IPAC2014-TUPRI074>.
- [Hin08] Frank Hinterberger: *Physik der Teilchenbeschleuniger und Ionenoptik*. Springer Berlin Heidelberg, Berlin, Heidelberg, 2nd edition, 2008, ISBN 978-3-540-75281-3. <http://link.springer.com/10.1007/978-3-540-75282-0>.

- [HKB<sup>+</sup>05] Erhard Huttel, A.B. Kalefa, I. Birkel, A.-S. Müller, P. Wesolowski, F. Pérez, M. Pont, and M. Giovannozzi: *Operation With A Low Emittance Optics At ANKA*. In *Proceedings of the 2005 Particle Accelerator Conference (PAC'05), Knoxville, TN, USA, May 2005*, page 2467. JACoW Publishing, 2005.
- [Hof04] Albert Hofmann: *The Physics of Synchrotron Radiation*. Cambridge Monographs on Particle Physics, Nuclear Physics, and Cosmology ; 20. Cambridge University Press, Cambridge, 1. publ. edition, 2004, ISBN 978-0-521-30826-7.
- [Hue] K. Huebner: *LEP2 Present and Future Performance and Limitations*. In *Proceedings of the 6th European Particle Accelerator Conference (EPAC'98)*, Stockholm, Sweden.
- [KB90] Peter Kuske and Johannes Bahrtdt: *Influence of the Bessy Undulator on the Beam Dynamics*. In *Proceedings of the 2nd European Particle Accelerator Conference (EPAC'90)*, pages 1417–1419, Nice, France, 1990.
- [Keh19] Benjamin Kehrer: *Time-resolved studies of the micro-bunching instability at KARA*. Dissertation, Karlsruhe Institute of Technology (KIT), 2019. <https://doi.org/10.5445/IR/1000098584>.
- [Las93] Jacques Laskar: *Frequency analysis for multi-dimensional systems. Global dynamics and diffusion*. Physica D: Nonlinear Phenomena, 67(1):257–281, 1993, ISSN 0167-2789. [http://doi.org/10.1016/0167-2789\(93\)90210-R](http://doi.org/10.1016/0167-2789(93)90210-R).
- [MBH<sup>+</sup>03] Anke-Susanne Müller, I. Birkel, E. Huttel, F. Perez, M. Pont, and R. Rossmanith: *Linear and nonlinear optics studies in the anka storage ring*. In *Proceedings of the 2003 Bipolar/BiCMOS Circuits and Technology Meeting (IEEE Cat. No.03CH37440)*, volume 5, pages 3273–3275, Portland, OR, USA, 2003. IEEE, ISBN 0-7803-7738-9. <http://ieeexplore.ieee.org/document/1289885/>.
- [MVS<sup>+</sup>12] Nicolai Mezentsev, A.A. Volkov, V. Skaruba, S. Khrushchev, V. Tsukanov, E. Miginskaya, V.M. Syrovatin, and V.H. Lev: *Final Design Report Superconducting Multipole Wiggler for ANKA CATACT beamline (unpublished)*, 2012.
- [MVS<sup>+</sup>16] Nicolai Mezentsev, A.A. Volkov, V. Shkaruba, S. Khrushchev, K. Zolotarev, A. Bragin, I. Poletaev, V. Tsukanov, V.M. Syrovatin, V.H. Lev, A. Zorin, and O. Tarasenko: *Technical Report: ANKA CLIC Superconducting Multipole Wiggler (unpublished)*, 2016.
- [MZ03] Michiko G. Minty and Frank Zimmermann: *Measurement and Control of Charged Particle Beams*. Particle Acceleration and Detection. Springer, 2003, ISBN 3-540-44187-5.
- [PBB<sup>+</sup>19] Alexander I. Papash, E. Blomley, T. Boltz, M. Brosi, E. Bründermann, S. Casalbuoni, J. Gethmann, E. Huttel, B. Kehrer, A. Mochihashi, A.-S. Müller, R. Ruprecht, M. Schuh, and J.L. Steinmann: *New Operation Regimes at the*

- Storage Ring KARA at KIT*. In *Proceedings of the 10th International Particle Accelerator Conference (IPAC'19)*, pages 1422–1425, Melbourne, Australia, 2019. JACoW Publishing. <https://doi.org/10.18429/JACoW-IPAC2019-TUPGW016>.
- [PBG<sup>+</sup>17] Alexander I. Papash, E. Blomley, J. Gethmann, E. Huttel, A.-S. Müller, and M. Schuh: *High Order Magnetic Field Components And Non-Linear Optics At The ANKA Storage Ring*. In *Proceedings of the 8th International Particle Accelerator Conference (IPAC'17)*, pages 2586–2588, Copenhagen, Denmark, 2017. JACoW Publishing. <https://doi.org/10.18429/JACoW-IPAC2017-WEPAB011>.
- [plc17] Cobham plc: *Opera-3d*, 2017. <http://www.cobham.com/about-cobham/aerospace-and-security/about-us/antenna-systems/specialist-technical-services-and-software/products-and-services/design-simulation-software/opera.aspx>.
- [PVG<sup>+</sup>11] Fabian Pedregosa, G. Varoquaux, A. Gramfort, V. Michel, B. Thirion, O. Grisel, M. Blondel, P. Prettenhofer, R. Weiss, V. Dubourg, J. Vanderplas, A. Passos, D. Cournapeau, M. Brucher, M. Perrot, and E. Duchesnay: *Scikit-Learn: Machine Learning in Python*. *Journal of machine learning research*, 12:2825–2830, 2011. <http://jmlr.org/papers/v12/pedregosa11a.html>.
- [Rie14] Markus Ries: *Nonlinear momentum compaction and coherent synchrotron radiation at the Metrology Light Source*. Dissertation, Humboldt-Universität zu Berlin, 2014. <http://edoc.hu-berlin.de/docviews/abstract.php?id=40712>.
- [Rut83] Ronald D. Ruth: *A Canonical Integration Technique*. *IEEE Trans. Nucl. Sci.*, 30(4):2669–2671, 1983. <https://ieeexplore.ieee.org/document/4332919>.
- [Saf89] James Safranek: *Beam Dynamics in Wigglers: Tracking in PEP with Damping Wigglers and Measurements at Spear*. In *Proceedings of the Particle Accelerator Conference (PAC'89)*, page 1307. IEEE, 1989. <https://cds.cern.ch/record/900194>.
- [Saf97] James Safranek: *Experimental determination of storage ring optics using orbit response measurements*. *Nuclear Instruments and Methods in Physics Research Section A: Accelerators, Spectrometers, Detectors and Associated Equipment*, 388(1-2):27–36, mar 1997. [https://doi.org/10.1016/S0168-9002\(97\)00309-4](https://doi.org/10.1016/S0168-9002(97)00309-4).
- [SBB<sup>+</sup>19] Patrick Schreiber, T. Boltz, M. Brosi, B. Härer, A. Mochihashi, A.-S. Müller, A.I. Papash, and M. Schuh: *Status of Operation With Negative Momentum Compaction at KARA*. In *Proceedings of the 10th International Particle Accelerator Conference (IPAC'19)*, pages 878–881, Melbourne, Australia, 2019. JACoW Publishing. <https://doi.org/10.18429/JACoW-IPAC2019-MOPTS017>.
- [Sch85] E.T. Scharlemann: *Wiggle Plane Focusing in Linear Wigglers*. *J. Appl. Phys.*, 58(6):2154–2161, 1985. <https://doi.org/10.1063/1.335980>.

- [Sch92] Peter Schmüser: *Magnetic measurements of superconducting magnets and analysis of systematic errors*. CAS - CERN Accelerator School : Magnetic measurement and alignment, (DESY-HERA-P-92-1):35 p, mar 1992. <https://doi.org/10.5170/CERN-1992-005.240>.
- [Sch97] Frank Schmidt: *Methodical Accelerator Design (MAD-8)*, 1997. <https://mad.web.cern.ch/mad>.
- [SLT<sup>+</sup>02] James Safranek, C. Limborg, A. Terebilo, K.I. Blomqvist, P. Elleaume, and Y. Nosochkov: *Nonlinear dynamics in a SPEAR wiggler*. Physical Review Special Topics - Accelerators and Beams, 5(1):010701, January 2002. <http://doi.org/10.1103/PhysRevSTAB.5.010701>.
- [Smi86] Lloyd Smith: *Effects of Wigglers and Undulators on Beam Dynamics*. In *13th International Conference on High-energy Accelerators*, page 4, 1986.
- [SSB<sup>+</sup>19] Patrik Schönfeldt, P. Schreiber, M. Brosi, J. Schestag, T. Boltz, M. Blaicher, and J. Gethmann: *Inovesa: Noisy and non-linear, release candidate 3*, jun 2019. <https://doi.org/10.5281/zenodo.3236959>.
- [Str12] Max Streichert: *Sextupole Strengths (private communication)*. 2012.
- [Ter01] Andrei Terebilo: *Accelerator Toolbox for MATLAB*. 2001. <http://www.slac.stanford.edu/grp/ssrl/spear/at/>.
- [The18] The CLICdp collaborations: *The Compact Linear Collider (CLIC) - 2018 Summary Report*. Technical report, CERN, Geneva, Switzerland, 2018. <https://doi.org/10.23731/CYRM-2018-002Burrows,PhilipN>.
- [VGO<sup>+</sup>20] Pauli Virtanen, R. Gommers, T.E. Oliphant, M. Haberland, T. Reddy, D. Cournapeau, E. Burovski, P. Peterson, W. Weckesser, J. Bright, S.J. van der Walt, M. Brett, J. Wilson, K.J. Millman, N. Mayorov, A.R.J. Nelson, E. Jones, R. Kern, E. Larson, C.J. Carey, Í. Polat, Y. Feng, E.W. Moore, J. VanderPlas, D. Laxalde, J. Perktold, R. Cimrman, I. Henriksen, E.A. Quintero, C.R. Harris, A.M. Archibald, A.H. Ribeiro, F. Pedregosa, and P. van Mulbregt: *SciPy 1.0: fundamental algorithms for scientific computing in Python*. Nature Methods, 17(3):261–272, mar 2020. <http://www.nature.com/articles/s41592-019-0686-2>.
- [VW02] Marco Venturini and R. Warnock: *Bursts of Coherent Synchrotron Radiation in Electron Storage Rings: A Dynamical Model*. Physical Review Letters, 89(22):224802, nov 2002. <https://link.aps.org/doi/10.1103/PhysRevLett.89.224802>.
- [Wal83] Richard P. Walker: *Electron Beam Focusing Effects and Matching Conditions in Plane Periodic Magnets*. Nuclear Instruments and Methods, 214(2-3):497–504, 1983. [http://doi.org/10.1016/0167-5087\(83\)90622-1](http://doi.org/10.1016/0167-5087(83)90622-1).

- [Wal93] Richard P. Walker: *Wigglers*. In Stuart Turner (editor): *CERN Accelerator School*, number 5, pages 807–835. CERN, 1993. <https://doi.org/10.5170/CERN-1995-006.807>.
- [Wan03] Chun-xi Wang: *Model Independent Analysis of Beam Centroid Dynamics in Accelerators*. Technical report, SLAC National Accelerator Laboratory (SLAC), Menlo Park, CA (United States), apr 2003. <https://doi.org/10.2172/813017>.
- [WBC<sup>+</sup>95] Richard P. Walker, R. Bracco, A. Codutti, B. Diviacco, D. Millo, and D. Zangrando: *Status of ELETTRA insertion devices*. In *Proceedings of the Particle Accelerator Conference (PAC'95)*, pages 1432 – 1434, Dallas, TX, USA, may 1995. <https://doi.org/10.1109/PAC.1995.505246>.
- [WFR03] Y.K. Wu, E. Forest, and D.S. Robin: *Explicit symplectic integrator for s-dependent static magnetic field*. *Physical Review E*, 68(4):046502, oct 2003. <https://doi.org/10.1103/PhysRevE.68.046502>.
- [Wie88] Helmut Wiedemann: *Low emittance storage ring design*. In M. Month and S. Turner (editors): *Frontiers of Particle Beams*, volume 296 of *Lecture Notes in Physics*, pages 390–439. Springer Berlin Heidelberg, 1988. <http://link.springer.com/10.1007/BFb0031502>.
- [Wie07] Helmut Wiedemann: *Particle Accelerator Physics*. Springer Berlin Heidelberg, 3rd edition, 2007. <http://link.springer.com/10.1007/978-3-540-49045-6>.
- [Wie15] Helmut Wiedemann: *Particle Accelerator Physics*. Graduate Texts in Physics. Springer International Publishing, 4th edition, 2015. <http://link.springer.com/10.1007/978-3-319-18317-6>.
- [Wol01] Andrej Wolski: *Symplectic Integrators for Nonlinear Wiggler Fields*, 2001. <http://www-project.slac.stanford.edu/lc/ilc/TechNotes/LCCNotes/PDF/LCC-0062%2520final.pdf>.
- [Wu04] Y.K. Wu: *Canonical Integration Code for Wigglers*. 2004.
- [Zis18] Panagiotis Zisopoulos: *Optics characterisation at ANKA including the high wiggler field*, 2018. <https://indi.to/LMb36>.
- [ZKPS02] Anže Zupanc, I. Križnar, M. Pleško, and U. Simon: *Orbit correction with frequency in java*. In *4th International Workshop on Personal Computers and Particle Accelerator Controls*, Frascati, 2002. <http://www.lnf.infn.it/conference/pcapac2002/TALK/TU-P13/TU-P13.pdf>.
- [ZPA<sup>+</sup>15] Panos Zisopoulos, Y. Papaphilippou, F. Antoniou, A.-S. Müller, and E. Hertle: *Transverse Tunes Determination from Mixed BPM Data*. In *Proceedings of the 6th International Particle Accelerator Conference (IPAC'15)*, pages 1709–1712, Richmond, VA, USA, 2015. JACoW Publishing. <https://doi.org/10.18429/JACoW-IPAC2015-TUPJE042>.

- [ZPL19] Panagiotis Zisopoulos, Y. Papaphilippou, and J. Laskar: *Refined betatron tune measurements by mixing beam position data*. Phys. Rev. Accel. Beams, 22(7):71002, jul 2019. <https://link.aps.org/doi/10.1103/PhysRevAccelBeams.22.071002>.
- [ZW96] Dino Zangrando and Richard P Walker: *A stretched wire system for accurate integrated magnetic field measurements in insertion devices*. Nuclear Instruments and Methods in Physics Research Section A: Accelerators, Spectrometers, Detectors and Associated Equipment, 376(2):275–282, 1996, ISSN 0168-9002. <http://www.sciencedirect.com/science/article/pii/0168900296002070>.

# Acknowledgement

At this place I want to thank everybody who supported me and contributed to the success of this work. I do want to express my special gratitude to the following persons:

Prof. Dr. Anke-Susanne Müller for the supervision of my work, the fruitful discussions and feedback and support in many other ways, ranging from the contribution to the lecture as well as the connections with other experts on conferences and workshops.

Prof. Dr. Guido Drexlin for his feedback and his co-supervision.

Dr. Axel Bernhard for supporting me in his working group during this long time from the end of the Diploma thesis to the end of all proof reading of this thesis. For all the great moments also apart from the work and the supportive words in phases when negative results seemed to be strong burdens.

Edmund Blomley for being the operator of choice, many discussions, helping at night shifts remotely or on site and of course all the collaborative, e. g. software related work and really friendly room mate.

Dr. Miriam Brosi for the strong support especially in THz and low- $\alpha$  related topics, whether via discussions or measurements.

Dr. Marcel Schuh, and also Dr. Erhard Huttel, for the support with the machine also at unpleasant times.

Dr. Alexander Papash for fruitful discussions and support during some measurements.

Dr. Benjamin Kehrer for fruitful discussions about AT models.

Dr. Markus Schwarz for discussions about and explanations of accelerator physics theory and for proof reading on short notice and the yet good feedback.

The Advanced Accelerator Concepts group and Dr. Christina Widmann, the THz group, and also the ID group for general support, discussions and the academic life beyond the work.

Last but not least, I want to thank my friends who supported me during this time mentally and my family for their constant motivation, encouragement, and support in all aspects.